

# Numerical Approaches for Loads and Motions Assessment of Floating Offshore Renewable Energy Devices Moored by Means of Catenary Mooring Systems

A thesis submitted in partial fulfillment of the requirements for the  
degree of Philosophiae Doctor (PhD) by

Imanol Touzón



Bilbao, January 2021

Department of Mechanical Engineering  
Faculty of Engineering of Bilbao  
University of the Basque Country UPV-EHU

Supervisors: Prof. Victor Petuya  
Dr. Vincenzo Nava





# Abstract

Technologies for harvesting offshore renewable energy based on floating platforms, such as offshore wind, wave and tidal energies, are currently being developed with the purpose of achieving a competitive cost of energy. The economic impact of the mooring system is significant within the total cost of such deployments and large efforts are being carried out to optimise designs. In order to obtain economically efficient designs, it is very convenient that the mooring system is considered with sufficient accuracy from early stages of the technology development path. Analysis of mooring systems at early stages generally require a trade-off between quick analysis methods and accuracy to carry out multi-variate sensitivity analyses. Even though the most accurate approaches are based on the non-linear finite element method in the time domain, they can result in being very time consuming.

The most widely used numerical approaches for mooring line load estimates have been analysed and compared in the preliminary stage of this thesis. It is shown that mooring optimization analyses can be carried out for heaving wave energy converters considering the horizontal stiffness introduced by the mooring system in the floating structure, as long as the considered pretensions are mild. In addition, it is also verified that accurate line tension estimates require lines drag and inertia forces to be accounted for.

A mooring and floating structure coupled model has been developed based on the lumped mass approach. It has also been validated with experimental wave tank testing results of a floating cylindrical buoy moored through three catenary lines, provided by TECNALIA. It has been confirmed that the differences found in the floating structure and mooring coupled numerical model have been mainly produced by the uncertainty on hydrodynamic force estimates on the floating structure rather than by the lumped mass method, that has been found to be very accurate. In addition, seabed friction significantly influences line tension of lines with transverse motions, and friction models should be carefully selected and adjusted.

With the purpose of enabling quick line tension estimates, a linearization of the structure and mooring coupled model has been proposed and a frequency domain approach has been developed. It has been verified against the corresponding results of the already validated time domain model, both applied to a floating wave energy converter moored with three catenary lines. The obtained results in operational conditions have been accurate enough, enabling modal analysis of the coupled system.

# Resumen

Actualmente se están desarrollando tecnologías para la captación de energías renovables marinas basadas en plataformas flotantes, como las energías eólica marina, undimotriz y mareomotriz, con el fin de lograr un coste de la energía competitivo. El impacto económico del sistema de fondeo es significativo dentro del coste total de dichos despliegues y se están realizando grandes esfuerzos para optimizar los diseños. Con el fin de obtener diseños económicamente eficientes, es muy conveniente que el sistema de fondeo se considere con suficiente precisión desde las primeras etapas del desarrollo tecnológico de las tecnologías correspondientes. El análisis de los sistemas de fondeo en las primeras etapas generalmente requiere un equilibrio entre métodos rápidos de análisis y una precisión suficiente para llevar a cabo análisis de sensibilidad de múltiples variables. Aunque los enfoques más precisos se basan en el método de elementos finitos no lineales en el dominio del tiempo, éstos pueden resultar en altos costes computacionales.

En la etapa preliminar de esta tesis se han analizado y comparado los enfoques numéricos más utilizados para estimar las cargas en las líneas de amarre. Se muestra que se pueden realizar análisis de optimización de fondeos para convertidores de energía de olas basados en su dinámica vertical considerando la rigidez horizontal que introduce el sistema de fondeo en la estructura flotante, siempre que las pretensiones consideradas sean leves. Asimismo, se verifica que estimaciones precisas de las tensiones de línea requieren que se tengan en cuenta las fuerzas de inercia y viscosas del fluido en dichas líneas.

Posteriormente se ha desarrollado un modelo acoplado de estructura flotante y fondeo basado en el enfoque *'lumped mass'*. Éste ha sido validado con resultados de ensayos experimentales en tanque de olas de una boya cilíndrica flotante amarrada a través de tres líneas en catenaria, proporcionados por TECNALIA. Se ha confirmado que las diferencias encontradas entre los resultados del modelo numérico y los del modelo físico se han producido principalmente por incertidumbre en las estimaciones de las fuerzas hidrodinámicas en la estructura

flotante, en lugar de en el modelo de las líneas de fondeo, basado en el método de *'lumped mass'* que se ha verificado que es muy preciso. Asimismo, la fricción con el lecho marino influye significativamente en la tensión de las líneas con movimientos transversales, y los modelos de fricción deben seleccionarse y ajustarse cuidadosamente.

Con el fin de permitir estimaciones rápidas de la tensión de la línea, se ha propuesto una linealización del modelo acoplado de estructura y fondeo y se ha desarrollado un enfoque en el dominio de la frecuencia. Se ha verificado con los correspondientes resultados del modelo en el dominio del tiempo ya validado, ambos aplicados a un convertidor de energía undimotriz flotante amarrado con tres líneas en catenaria. Los resultados obtenidos en condiciones operativas han sido satisfactorios, permitiendo a su vez el análisis modal del sistema acoplado.

# Acknowledgment

This thesis has been developed under the supervision of Professor Victor Petuya in the Department of Mechanical Engineering of the School of Engineering of the University of the Basque Country (UPV / EHU). His continuous and efficient orientation in the search for the best solution, his availability for regular talks and his always constructive attitude, have made possible the development of this work. The co-supervision of the thesis has been carried out by Doctor Vincenzo Nava, from TECNALIA. His availability to talk about the evolution of the work, as well as his vision on the approaches of the publications and of the doctoral document itself have been a key element. Thanks to both.

During this time there has been a very close collaboration with the Offshore Renewable Energy research group at TECNALIA whose people have served as inspiration both personally and professionally. Specifically, I want to thank Jose Luis Villate and Pedro Ibañez for enabling my stay in Norway and Raúl Rodríguez and Pablo Benguria for openly sharing tank testing data, both aspects have strengthened the final result. Moreover, I want to thank Joseba López, Miren Sánchez, Eider Robles, Iñigo Mendikoa and Javier López for their attitude and fellowship, which have contributed very positively to my development. In addition, I am very grateful to Zhen Gao for welcoming me and guiding me with his wide experience during three valuable months in the Marine Technology department at NTNU. I do not want to forget to mention Pierpaolo Ricci, Martín Ojanguren and Borja de Miguel, our collaboration during my first steps was decisive in the direction of my work.

Last but not least, I am very grateful to all my family and friends for your patience and understanding during these years. Especially to Esti for your continuous support in all aspects, assuming much more than I could have even imagined and to Ane, you give us the energy to enjoy everything, nights included.

*“Ezina, ekinez egina”*



# Agradecimientos

Esta tesis ha sido desarrollada bajo la supervisión del Profesor Victor Petuya en el Departamento de Ingeniería Mecánica de la Escuela de Ingenieros de la Universidad del País Vasco (UPV/EHU). Su continua y eficiente orientación en la búsqueda de la mejor solución, su disponibilidad para charlas periódicas y su actitud, siempre constructiva, han hecho posible que este trabajo salga adelante. La codirección de la tesis ha corrido a cargo del Doctor Vincenzo Nava, de TECNALIA. Su disponibilidad para conversar sobre la evolución del trabajo, así como sobre los enfoques de las publicaciones y del propio documento de doctorado han sido un elemento clave. Gracias a ambos.

Durante este tiempo ha habido una colaboración muy estrecha con el grupo de investigación de Energías Renovables Offshore en TECNALIA, cuyas personas han servido de inspiración tanto a nivel personal como profesional. Concretamente quiero agradecer a Jose Luis Villate y Pedro Ibañez el hecho de habilitar mi estancia en Noruega y a Raúl Rodríguez y Pablo Benguria por compartir abiertamente los datos de los ensayos en canal, ambos aspectos han fortalecido el resultado final. Asimismo, quiero agradecer a Joseba López, Miren Sánchez, Eider Robles, Iñigo Mendikoa y Javier López su actitud y compañerismo, que han contribuido muy positivamente en mi desarrollo. Agradezco a Zhen Gao haberme acogido y guiado con su amplio conocimiento durante tres valiosos meses en NTNU. No quiero dejar de mencionar a Pierpaolo Ricci, Martín Ojanguren y Borja de Miguel, nuestra colaboración durante mis primeros pasos fue determinante en la dirección de mi trabajo.

Por último, no por ello menos importante, estoy muy agradecido a toda mi familia y amigos por vuestra paciencia y comprensión durante estos años. Especialmente a Esti por tu apoyo continuo en todos los aspectos, asumiendo mucho más de lo que ni siquiera hubiera imaginado y a Ane, tú nos das la energía para disfrutar de todo, noches incluidas.

*“Ezina, ekinez egina”*

# Table of Contents

<b>Abstract</b> .....	<b>i</b>
<b>Resumen</b> .....	<b>iii</b>
<b>Acknowledgment</b> .....	<b>v</b>
<b>Agradecimientos</b> .....	<b>vi</b>
<b>Table of Contents</b> .....	<b>vii</b>
<b>List of Illustrations</b> .....	<b>x</b>
<b>List of Tables</b> .....	<b>xvii</b>
<b>Nomenclature</b> .....	<b>xviii</b>
General .....	xviii
Symbols .....	xviii
Abbreviations .....	xx
<b>Chapter 1</b> .....	<b>1</b>
<i>Introduction</i> .....	<i>1</i>
1.1 Background .....	1
1.2 Previous Work of Other Researchers .....	2
1.3 Outline of the Thesis .....	7
1.4 Main Contributions .....	9
<b>Chapter 2</b> .....	<b>11</b>
<i>State of the Art</i> .....	<i>11</i>
2.1 Introduction .....	11
2.2 Marine Renewable Energy. Wave Energy Technology Potential and Development .....	11
2.3 Numerical Modeling Methods .....	24
2.4 Chapter Summary .....	57
<b>Chapter 3</b> .....	<b>59</b>

<i>Development of Numerical Models for Moored Offshore Floating Energy Systems</i> .....	59
3.1 Introduction .....	59
3.2 Quasistatic Linearized Frequency Domain .....	60
3.3 Quasistatic Non-Linear Time Domain .....	64
3.4 Dynamic Non-Linear Time Domain .....	66
3.5 Dynamic Linearized Frequency Domain .....	70
3.6 Case Study Geometries of Floating Structures .....	75
3.7 Chapter Summary.....	85
<b>Chapter 4</b> .....	<b>87</b>
<i>Comparison of Numerical Approaches in Extreme Conditions</i> .....	87
4.1 Introduction .....	87
4.2 Numerical Model Settings.....	88
4.3 Results and Discussion.....	91
4.4 Chapter Summary.....	113
<b>Chapter 5</b> .....	<b>115</b>
<i>Small Scale Experimental Validation of the Dynamic Non-Linear Time Domain Model</i> .....	115
5.1 Introduction .....	115
5.2 Numerical Model Settings.....	116
5.3 Results and Discussion.....	124
5.4 Chapter Summary.....	148
<b>Chapter 6</b> .....	<b>151</b>
<i>Numerical Verification of the Dynamic Linearized Frequency Domain Model</i> .....	151
6.1 Introduction .....	151
6.2 Numerical Model Settings.....	152
6.3 Results and Discussion.....	157

6.4 Chapter Summary .....	174
<b>Chapter 7 .....</b>	<b>177</b>
<i>Conclusions</i> .....	177
<b>Recommendations for Future Work .....</b>	<b>181</b>
<b>References .....</b>	<b>183</b>
<b>Main Outcomes of this Thesis .....</b>	<b>193</b>
Articles Indexed in Journal Citation Reports .....	193
Conference Publications.....	194
Participation in Seminars .....	195

# List of Illustrations

Figure 1 Estimated Average Annual Wave Power per meter of incoming wave front. Courtesy of <i>J. Cruz</i> [24].....	12
Figure 2 Main Wave Energy Conversion technologies. From top left to bottom right: Submerged pressure differential, Attenuators, Surface point absorber, Oscillating water column, Overtopping devices and Oscillating wave surge converters. Courtesy of <i>Aquaret</i> [25] .....	14
Figure 3 Pelamis Wave power P2-001 device installed. Courtesy of <i>EMEC</i> [26] .....	15
Figure 4 Aquamarine power’s Oyster 800 device installed (left) and during its deployment (right). Courtesy of <i>EMEC</i> and <i>OffshoreWind.biz</i> [27] [28].....	16
Figure 5 MARMOK-A-5 device at open sea. Courtesy of <i>IDOM</i> [33] .....	17
Figure 6 Ocean Energy buoy ready for deployment. Courtesy of <i>Sustainable Energy Authority Of Ireland</i> [31] and the <i>U.S. Office of Energy Efficiency &amp; Renewable Energy</i> [35] .....	18
Figure 7 CorPower Ocean technology at open sea. Courtesy of <i>CorpowerOcean</i> [32].....	18
Figure 8 Breakwater in which the fixed <i>OWC</i> chambers are integrated (left) and some drivetrains mounted over the corresponding chambers (right). Courtesy of <i>Ente Vasco de la Energía</i> [36] .....	19
Figure 9 Annual electricity price in Spain during the year 2019. Courtesy of <i>Operador del Mercado Ibérico de Energía</i> [38] .....	20
Figure 10 Wave <i>LCOE</i> Percentage Breakdown by Cost Centre Values at Current Stage of Deployment (Left) and the commercial Target (Right). <i>International Energy Agency – Ocean Energy Systems</i> [42] .....	20
Figure 11 Most common mooring configurations used for offshore structures. <i>Courtesy of Reliability in a Sea of Risk (RiaSoR) project</i> [43] .....	22

Figure 12 Spread mooring system (left), turret mooring system (center) and CALM Buoy (right). Courtesy of <i>American Petroleum Institute</i> [45] .....	23
Figure 13 Plane progressive regular wave propagation. Courtesy of Ø. A. A. HARALD and E. KROGSTAD [46] .....	25
Figure 14 Wave particle velocity profiles in shallow waters (left) and deep waters (right). Courtesy of Ø. A. A. HARALD and E. KROGSTAD [46] .....	27
Figure 15 Wave surface elevation of a real sea.....	29
Figure 16 Occurrence matrix in the BIMEP area. Courtesy of <i>BIMEP</i> [50] .....	31
Figure 17 Axis conventions assumed in this thesis.....	33
Figure 18 Radiation Impulse Response Function example in heave .	38
Figure 19 Inversed Radiation Impulse Response Function for direct integration of the convolution term.....	41
Figure 20 Schematic of a top view of a floating structure with four mooring lines. Lines, lines tensions and forces in the plane of the surface water level have been pointed out. ....	47
Figure 21 Mooring line schematic representation. Last four nodes and the fairlead with local and global coordinates (top) and first five nodes and the anchor (bottom). The kinematic constraints to maintain the anchor and fairleads are represented with blue triangles .....	51
Figure 22 Friction force model.....	52
Figure 23 Mesh representation of the <i>BEM</i> model for the <i>WEC</i> spar platform submerged part (left) and its main physical properties (right). Data adapted from [16], model <i>K</i> .....	76
Figure 24 Hydrodynamic coefficients of the floating buoy spar <i>WEC</i> in surge, heave and pitch, the cross coupled coefficients have been omitted here, but used in the model. Added mass and Radiation damping of surge (top-left), heave (top-right) and pitch (bottom-left). Froude-Krylov and diffraction forces in surge, heave and pitch (bottom-right) .....	78

Figure 25 Optimal <i>PTO</i> damping per sea state computed with the <i>OWC</i> type <i>WEC</i> .....	79
Figure 26 Representation of the numerical model and mooring system of the HarshLab 2.0 (top) and the physical model tested (bottom)....	81
Figure 27 Hydrodynamic coefficients of the 1:13.6 <sup>th</sup> scale floating buoy HarshLab 2.0 in surge, heave and pitch. Added mass and Radiation damping of surge (top-left), heave (top-right) and pitch (bottom-left). Froude-Krylov and diffraction forces in surge, heave and pitch (bottom-right) .....	83
Figure 28 Heave-pitch cross coupling Morison coefficients .....	84
Figure 29 Four lines mooring system configuration modelled in 150m water depth .....	88
Figure 30 Sensitivity analysis of the <i>QSTD</i> iterative process. Surge of the structure and the corresponding mooring horizontal force (left) and relative errors of the standard deviation of both line tension and surge motion (right) .....	90
Figure 31 Baseline results of the <i>QSFD</i> model. Performance indicators of line design tension and design offset a) and cost indicators of mooring total mass and anchor radius b). Yellow arrows indicate direction of lines pretension increase within each linear mass indicated in the legend. ....	92
Figure 32 Surge factors with respect to <i>QSFD</i> model of the <i>QSTD</i> a) and <i>DynTD</i> b) approaches. Accumulated bars with the contribution of the mean and dynamic offsets .....	94
Figure 33 Heave a) and pitch b) std factors of the <i>DynTD</i> models....	95
Figure 34 Heave a) and pitch b) std factors of the <i>QSTD</i> models.....	96
Figure 35 Power spectral densities in surge ( <i>WF</i> magnified 20 times) (a), heave and pitch motions ( <i>WF</i> reduced by a factor of 2) (b) and (c) comparing models' performance with the largest and lowest non-dimensional pretension.....	98
Figure 36 Normalized <i>PDFs</i> with the three models in surge a), heave b), pitch c) and the most loaded line tension d) .....	100

Figure 37 Kurtosis and skewness of surge motion (a)(b), heave motion (c)(d), pitch motion (e)(f) and most loaded line tension (g)(h) obtained with the <i>DynTD</i> approach .....	103
Figure 38 Most Loaded Line tension factors for the <i>WEC</i> with the <i>QSTD</i> a) and <i>DynTD</i> b) models .....	104
Figure 39 Most loaded line tension <i>PSDs</i> comparison with the approaches considered.....	105
Figure 40 Normalized <i>PDFs</i> of the most loaded line with the three approaches. High pretension a) and low pretension b) .....	106
Figure 41 Time series portion of buoy heaving and the corresponding tension of the most loaded line.....	106
Figure 42 Line tension of <i>WEC</i> with large pretension a) and low pretension b) for three models. Green: <i>QSFD</i> , Blue: <i>QSTD</i> and Orange: <i>DynTD</i> .....	107
Figure 43 Design (top) and cost (bottom) spaces for the <i>WEC</i> structure with the <i>QSFD</i> (red squares), <i>QSTD</i> (green triangles) and <i>DynTD</i> (blue circles) models.....	109
Figure 44 Correction factors between the <i>DynTD</i> and the <i>QSFD</i> models for five linear mass values (65, 85, 105, 125 and 145) and a linear fitting of the mean values for Anchor Radius (a), Suspended length (b) and Design Tension (c) .....	111
Figure 45 Cost optimization of the mooring system. Total cost is the sum of the lease area and the total mooring mass assuming a cost ratio of 3 [€/kg]/[€/m <sup>2</sup> ] .....	112
Figure 46 Experimental physical moored model subject to the sea state 10 (see Table 11), side view, a) and boat landing upper view b).....	117
Figure 47 Estimated water surface elevation at the structure position from the sensors available FO and SB .....	118
Figure 48 Six degree of freedom dynamometer a) and load cells for line tension measurement b) and a wave elevation gauge c) .....	119
Figure 49 Mooring system representation of the Harsh 2.0 floating platform, scale 1:13.6. Mooring lines top view, HarshLab2.0 structure, mooring line anchors and wave sensor positions are represented....	120



Figure 50 Decay test simulations after drag force coefficient computation in heave a), roll b) and pitch c).....	127
Figure 51 Static response of the mooring system to horizontal positions of the floating structure .....	128
Figure 52 Decay test simulations after drag force coefficient computation in surge a), sway b) and yaw c).....	130
Figure 53 Line tension comparison between experimental and numerical models for decay tests in surge for the three lines. Line 1: a); Line 2: b); Line 3: c) .....	132
Figure 54 Line tension comparison between experimental and numerical models for decay tests in sway for the three lines. Line 1: a); Line 2: b); Line 3: c) .....	133
Figure 55 Line tension comparison between experimental and numerical models for decay tests in yaw for the three lines .....	134
Figure 56 Heave decay test with mooring and the induced pitch motion. Solid lines: Experimental; Dashed lines: Numerical.....	135
Figure 57 Obtained experimental model motion (Exp) and filtered imposed numerical motions (Num) in the Sea State 2 .....	136
Figure 58 Line tensions obtained in the numerical simulations with imposed motions (dashed line) compared with the experimental tests in the Sea State 1 (solid line). Line 1: a); Line 2: b); Line 3: c).....	137
Figure 59 Maximum line tension comparisons and maximum tension error percentages. Line 1: a) and b); Line 2: c) and d); Line 3: e) and f). .....	138
Figure 60 Standard deviations of line tension comparisons and tension error percentages. Line 1: a) and b); Line 2: c) and d); Line 3: e) and f). .....	139
Figure 61 Lines 1 and 2 tensions from experimental and numerical tests .....	140
Figure 62 Structure motions obtained in the <i>DynTD</i> coupled simulation subject to sea state 1. Surge: a); Heave: b); Pitch: c) .....	142

Figure 63 Lines tensions obtained in the hydrodynamics and mooring coupled simulations subject to sea state 1. Line 1: a); Line 2: b); Line 3: c).....	143
Figure 64 Structure motion standard deviations comparisons and the corresponding error percentages. Degrees of freedom 1 (surge): a) and b); 3 (heave): c) and d); 5 (pitch): e) and f).....	145
Figure 65 Maximum line tension comparisons and error percentages with the <i>DynTD</i> coupled simulations. Line 1: a) and b); Line 2: c) and d); Line 3: e) and f). ....	146
Figure 66 Standard deviations of line tensions and their error percentage with the <i>DynTD</i> coupled simulations. Line 1: a) and b); Line 2: c) and d); Line 3: e) and f). ....	147
Figure 67 Floating <i>WEC</i> with the three-line mooring system.....	153
Figure 68 Resulting time series of the sensitivity analysis to the number of sections used to discretize each mooring line. Time series of line 1 a), line 3 b) and surge c).....	155
Figure 69 Relative errors found in standard deviations of the sensitivity analysis to the number of line sections. Relative errors of the standard deviations of lines 1 and 3 a) and surge b).....	156
Figure 70 Sea State Occurrence probability at BiMEP sea test site [50] and the Sea States with more than 1% occurrence probability (red stars), selected for <i>TD</i> and <i>FD</i> simulation verification.....	157
Figure 71 Structure and internal surface water level motion a) and lines tension amplitudes at the fairleads b) and eigenvalues within the showed frequency range (vertical lines). Response amplitudes $H_s=1.5m$ and $T_p=8.5s$ .....	159
Figure 72 Modes of the coupled model mainly related with surge a) and sway b) .....	160
Figure 73 Modes of the coupled model mainly associated with pitch a) and roll b) .....	162
Figure 74 Modes of the coupled model mainly associated with heave of the structure a) and pitch of the surface water level b) .....	163

Figure 75 Modes of the coupled model associated with line motions in the plane of the catenary of the windward lines a) and the leeward line b)..... 164

Figure 76 Surge motion *PSDs* of the floater. Wave frequency magnified with a factor of 100 to enable plotting the whole *PSD* in a single figure. Dash-dotted vertical lines indicate the relevant modes identified in section 6.3.1..... 165

Figure 77 Heave motion *PSDs* of the floater (solid lines) and the internal *SWL* (dashed lines). Dash-dotted vertical lines indicate the relevant modes identified in section 6.3.1 ..... 166

Figure 78 Pitch motion *PSDs* of the floater (solid lines) and the internal *SWL* (dashed lines). Dash-dotted vertical lines indicate the relevant modes identified in section 6.3.1 ..... 166

Figure 79 Percentage differences of the standard deviation of motions obtained with the *DynFD* with respect to the *DynTD*. Contour lines represent zero levels. a) Surge; b) Heave of the structure; c) Heave of the internal *SWL*; d) Pitch of the structure; e) Pitch of the internal *SWL* ..... 168

Figure 80 Line tension standard deviation (vertical lines at each node) with both models with respect to the mean line tension along the whole line 1 a) and line 3 b)..... 170

Figure 81 Difference percentage of the linearized frequency domain model with respect to the non-linear time domain model in terms of line tensions standard deviation at the fairlead. Contour lines represent zero levels, showing both limits of the selected simulation sea states and limits between under and overestimations of the *DynFD* model. .... 171

Figure 82 Line tension *PSD* comparison between the *FD* and *TD* models for low *Hs*, line 1: a) and line 3: b); intermediate *Hs*, line 1: c) and line 3: d); moderate *Hs*, line 1: e) and line 3: f). Dash-dotted vertical lines indicate the relevant modes identified in section 6.3.1 ..... 173

# List of Tables

Table 1 Viscous drag force factors considered for each degree of freedom of the structure and the corresponding natural frequencies .	77
Table 2 Harsh 2.0 platform shape and its main properties.....	82
Table 3 Mooring properties selected to be combined for simulation cases .....	89
Table 4 Environmental conditions for the reference simulation case	90
Table 5 Mean obtained kurtosis and skewness of the <i>WEC</i> motions and tension of the most loaded line with the non-linear QSTD approach .....	101
Table 6 Mooring system anchor and fairleads for both scales .....	120
Table 7 Mooring line structural and hydrodynamic properties .....	121
Table 8 Mooring stiffness and decay tests lists.....	122
Table 9 Performed forced oscillatory tests.....	123
Table 10 Regular wave tests performed on the floating moored structure .....	124
Table 11 Performed Sea States (JONSWAP) in both the physical and numerical models .....	124
Table 12 Damped natural frequency identified from the decay tests and percentage of added stiffness in heave, pitch and roll due to the influence of the boat landing, present in the physical model .....	126
Table 13 Found drag force coefficients and the corresponding mean error for the three analyzed decay tests .....	126
Table 14 Damped natural frequencies identified in the decay tests in surge, sway and yaw.....	129
Table 15 Obtained drag coefficients and the corresponding errors for each degree of freedom and decay test.....	129
Table 16 Mooring line lengths, fairleads and anchor points .....	153
Table 17 Mooring line properties.....	154

# Nomenclature

## General

Some general aspects need to be considered when reading this thesis, as explained in the following points:

- Variables in square brackets  $[\ ]$  denote matrices
- Variables in curly brackets  $\{ \}$  denote vectors
- Overdots indicate time derivatives
- Abbreviations are generally defined the first time they appear
- Units are indicated in square brackets  $[\ ]$  to be clearly distinguished from the text.
- When pairs of number in sub-scripts are used, denote row and column in matrices
- *Italics* are used to describe symbols, variables or specific aspects or names of equations as well as typing all abbreviations
- The symbol ‘ $\wedge$ ’ over a variable indicates complex amplitude
- Subscripts  $G$  and  $L$  denote the variable is referred to global and local coordinate centers respectively
- Subscripts in general are added to reference the object that the main variable refers to, e.g. *moor*, *str...*

## Symbols

$h$	water depth
$\eta$	Surface elevation
$\eta_a$	Wave amplitude
$\lambda$	wavelength
$\omega$	wave frequency
$\varphi$	Wave phase

$k$	Wave number
$\lambda$	Wavelength
$g$	Gravity
$\rho_w$	Water density
$u, v, w$	Horizontal (positive X and Y) and vertical (positive Z) fluid velocities
$E_p, E_k$	Potential and kinetic wave energy
$J$	Energy transport, Energy flux or Power flux
$S_x(\omega)$	Frequency spectrum of the variable $x$
$H_s$	Sea state significant wave height
$T_p$	Sea state peak period
$\sigma_x$	Standard deviation of the variable $x$
$\Theta$	Velocity potential
$\Psi$ and $\chi$	Normalized velocity potentials
$\delta, \dot{\delta}, \ddot{\delta}$	Rigid-body body position, velocity and acceleration
$A(\omega)$	Frequency dependent Radiation Added mass coefficient
$B(\omega)$	Frequency dependent Radiation Damping coefficient
$M$	Mass term
$K_h$	Hydrostatic Stiffness term
$F_w$	Wave excitation linear force. Froude-Krylov and Diffraction force coefficients
$B(\tau)$	Radiation impulse response function
$A(\infty)$	Infinite-frequency limit of the Added mass coefficient
$C_a$	Morison Added mass coefficient
$C_d$	Viscous force coefficient
$T_h$	Horizontal component of line tension
$w$	Mooring line submerged weight per unit length

$l_s$	Suspended line length
$E$	Material Young modulus
$A$	Cross sectional area
$\psi_i$	Angle in the XY plane of the mooring line $i$
$F_{hyd}$	Hydrodynamic Morison force
$\xi$	Critical damping of a mechanical system

## **Abbreviations**

<i>BEM</i>	Boundary Element Method
<i>CALM</i>	Catenary Anchor Leg Mooring
<i>COG</i>	Centre of Gravity
<i>DAE</i>	Differential Algebraic Equations
<i>DOF</i>	Degree of Freedom
<i>DynTD</i>	Dynamic Time Domain
<i>DynFD</i>	Dynamic Frequency Domain
<i>FD</i>	Frequency Domain
<i>FEM</i>	Finite Element Method
<i>IEC</i>	International Electrotechnical Commission
<i>KC</i>	Keulegan Carpenter
<i>LCOE</i>	Levelized Cost of Energy
<i>LF</i>	Low Frequency
<i>MLL</i>	Most Loaded Line

<i>O&amp;M</i>	Operations and Maintenance
<i>ODE</i>	Ordinary Differential Equations
<i>OWC</i>	Oscillating Water Column
<i>PDF</i>	Probability Density Function
<i>PSD</i>	Power Spectral Density
<i>PTO</i>	Power Take Off
<i>QSFD</i>	Quasistatic Frequency Domain
<i>QSTD</i>	Quasistatic Time Domain
<i>RAO</i>	Response Amplitude Operator
<i>RIRF</i>	Radiation Impulse Response Function
<i>SWL</i>	Surface Water Level
<i>TD</i>	Time Domain
<i>TRL</i>	Technology Readiness Level
<i>WEC</i>	Wave Energy Converter
<i>WF</i>	Wave Frequency





# Chapter 1

## Introduction

### 1.1 Background

Offshore renewable energies have already become relevant in the energy generation mix, especially bottom-fixed offshore wind, that has been commercially deployed for years. In addition, technologies based on floating structures for harvesting wind, tidal currents and wave energy, can be deployed in a wider variety of locations. They represent the largest untapped potential, and this makes them of interest for a large number of research projects.

Wave Energy Conversion technologies are being developed with the purpose to be deployed in groups of several devices and the cost of the mooring system is a relevant item within the total array cost. Therefore, it is very interesting that the estimates of the mooring cost are monitored along the path to commercialization, well estimated for single device and afterwards extrapolated to arrays of wave energy converters (*WECs*).

The sizing of mooring systems tends generally to be very influenced by extreme environmental conditions but are also subject to fatigue loading under operational conditions. Unlike other mechanical systems, mooring lines are generally described by non-linear models and, given the required low natural frequencies to horizontal motions compared to wave frequencies (*WF*), mooring analysis need long time domain (*TD*) simulations to define their statistics. Therefore, a design process in which multi-variate sensitivity analyses are required, can be difficult to be carried out with the most common numerical methods, based on the non-linear finite element method (*FEM*) solved in the time domain. There are alternative methods to reduce the computation time, that

consider catenary lines as quasistatic systems, solved both in the frequency and in the time domains. Several standardization bodies provide guidelines on how to apply such methods for traditional offshore structures based on quasistatic mooring lines. However, wave energy conversion structures are very dynamically excited and further assumptions may be necessary in order to use the mentioned quasistatic methods.

This thesis has been developed with a focus on numerical approaches for the assessment of floating structures moored through catenary mooring systems and applied to floating heaving *WECs*. The main rationale to perform this thesis has been to find the most appropriate numerical approaches for this kind of structures at early stages of development.

Therefore, a set of numerical models has been developed, validated and applied to a floating *WEC*, considered as a case study. Initially, the uncertainty of the simplest approaches has been provided for extreme events and different mooring settings. Subsequently, a fully coupled rigid body motions and lumped mass method numerical tool has been developed, which has been validated through physical results obtained in a tank testing campaign of a catenary anchor leg moored buoy, showing its strengths and weaknesses. This model has been linearized, and a frequency domain (*FD*) model has been proposed to account both for rigid body motions and lines drag and inertia forces. It has been verified with its non-linear counterpart, previously validated, providing the results in 36 sea states along with the most influencing aspects in its accuracy.

## **1.2 Previous Work of Other Researchers**

Large pieces of research have been carried out so far to estimate mooring loads appropriately. The most widely used method for numerical modelling of mooring lines is the non-linear lumped mass as well as the non-linear *FEM*. Many authors have already introduced this method and validated with tank test results, showing very good accuracy in a wide range of conditions.

V. D. Boom et al.[1] Introduced and validated an algorithm based on the lumped mass method with tank tests for mooring dynamic loads estimation. It was documented that dynamic effects of mooring lines strongly influence maximum line tensions and may, in some situations, affect the low frequency motions of the moored structure.

J. Azcona et al.[2] Presented a mooring numerical model based on the non-linear lumped mass method, solved in the time domain. It was validated with physical tests, consisting in regular horizontal motions of the fairlead in the plane of the catenary and also compared with the corresponding results of a quasistatic model. The lumped mass model showed accurate line tension results compared with the experimental data. The comparison between the lumped mass and the quasistatic model provided a maximum tension ratio between 2 and 3, highlighting the underestimation of the quasistatic model under certain periods. The code was subsequently coupled with FAST in J. Azcona et al.[3] for the assessment of fatigue loads on mooring lines of floating wind turbines. The coupling scheme consists in sharing motions and loads between parallel numerical models.

M. Hall et al.[4] Introduced a mooring numerical model based on the non-linear lumped mass method, solved in the time domain. It was validated with physical tests of a catenary moored floating wind turbine platform subject to regular waves. The results show good line tension estimates in prescribed motions while the accuracy is reduced when coupled with FAST. Results of the corresponding quasistatic model are also included, showing maximum line tensions of 60% to 70% with respect to the lumped mass. It is stated that structure hydrodynamics seem to introduce larger uncertainty than the lumped mass mooring model, however structure motions are not significantly sensitive to using either the quasistatic or the coupled lumped mass models. The coupling scheme is carried out through parallel numerical models, sharing forces and motions between the structure and the mooring models.

V. Harnois et al.[5] Used a non-linear *FEM* coupled with linear potential coefficients in a commercial code to validate a catenary mooring system with lines made up of combined chain with a compliant section. The hydrodynamic coefficients were complemented with non-

linear viscous drag term, fitted with the decay physical tests. It showed good results in irregular waves and the influence of drift force numerical estimation was investigated.

K. Xu et al.[6] Presented a numerical model of a catenary moored floating wind turbine, based on the finite element method coupled with the rigid body motions based on the potential flow theory. The effect of the water depth on mooring line loads was investigated in water depths within the range of 50m to 200m. It highlights that the slowly varying drift forces are underpredicted with the Newman approximation as the water depth decreases, having a significant influence on line tension estimates.

T. H. J. Bunnik et al.[7] Introduced a numerical model of a catenary anchor leg mooring buoy and its validation with tank test results. It is based on linear potential coefficients coupled to the lumped mass method. The model was complemented with a non-linear viscous drag term computed from the decay tests. It highlights that line dynamics are relevant for a good prediction of line tensions and that potential flow is not sufficient for pitch motion estimates.

M. The Vu et al.[8][9] Applied the quasistatic approach to estimate the umbilical cable influence on underwater vehicles, accounting for current forces on the umbilical. The results show significant influence on the underwater vehicle horizontal motions compared with the same configuration without the effect of the umbilical cable.

C. V. Amaechi et al.[10] Analysed the influence of considering hydrodynamic loads on lines with the lumped mass approach solved in the time domain. It results in an increase on line tensions with factors of up to 2 when accounting for hydrodynamic loads.

References [11] and [12] represent two commercial software packages, SESAM and SIMA, both based on the Simo and Riflex packages. It couples linear and non-linear body motions based on potential flow theory with non-linear finite elements for mooring lines and umbilical cable models. The coupling scheme is carried out through parallel numerical models, sharing forces and motions between the structure and the mooring models.

Reference [13] represents the commercial software Orcaflex that takes the outputs of linear potential flow solvers for body dynamics and couples with the corresponding mooring lines and umbilical cables including stiffness and damping terms directly between the corresponding degrees of freedom. This scheme has also been presented in Z. Ran et al. [14] which allows both mechanical systems to be solved fully coupled.

The applicability of the lumped mass and *FEM* methods also holds for Wave Energy Conversion technologies. This thesis addresses the applicability of the existing and the herein proposed coupled approaches to floating spar type heaving *WECs*. A significant effort is being made in order to bring a Wave Energy Conversion technology to a commercial stage, and many studies have been carried out to assess the power conversion capacity of technologies proposed by several research organizations, such as the floating spar type Oscillating Water Column (*OWC*) *WEC*.

A. F. de O. Falcão [15] Presented an in-depth review of the wave energy numerical modelling and development during four decades, up to 2010. Several topics are addressed: the wave energy resource, theoretical background, focused on wave energy absorption and control, power take off mechanisms and mooring systems. The main challenges of technology development were identified, such as costs of small testing, as well as the need to deploy large structures, adapted to the wavelength to optimize the energy absorption.

R. P. F. Gomes et al.[16] A Floating *OWC* device type geometry was optimised through extensive numerical modelling, with the objective of maximising wave energy absorption with geometric constraints. It is shown that the total submerged length was required to be relatively large in order to capture the energy in waves of larger periods. The influence of the air chamber height is more significant with larger submerged lengths.

F. X. Correia da Fonseca et al.[17] Carried out an experimental investigation of a floating *OWC* device type isolated and in a triangular array configuration. It was found that protecting the turbine through a fully closed chamber suppressed the turbine damping and aggravated

the mooring induced loads. It was also found that, once the heaving motion was tuned to the most energetic period, the array performance per device was improved compared with the isolated device.

However, the need to optimize mooring costs and monitor its influence on the levelized cost of energy (*LCOE*) has been pointed out by many authors. Therefore, it is very convenient to assess the coupled model from the very beginning of the design.

Early stages require a large number of very quick simulations, which has also inspired many authors to propose several *FD* based techniques to account for the coupled system. Some interesting pieces of research have been carried out to synthesize the mooring influence on the floater motions and others also proposed methods to estimate line tensions accounting to some extent for lines' inertia and drag loads.

Reference [18] is an offshore standard, it suggests an initial approach to synthesize the mooring influence on the floating structure in the offshore industry in general and in the offshore renewable energy sector. It consists in the linearization of the horizontal nonlinear geometric stiffness at the mean position of the structure. Through this procedure main horizontal motion properties and the order of magnitude of line tensions can be estimated.

F. Cerveira et al.[19] Introduced a numerical model of a floating *WEC* accounting for the influence of mooring lines. In order to account for geometric stiffness, inertia and drag effects, they added an equivalent impedance to the floater linear hydrodynamics. It allowed to assess the impact of the mooring system on wave energy extraction that was proved not to be significant for the investigated point absorber reacting against the seabed.

J. Fitzgerald et al.[20] Presented a methodology to account for the mooring influence on the floater performance. It is applied to a frequency domain numerical model of a generic *WEC*, consisting in a vertical heaving cylinder. The methodology consists in adding an equivalent impedance to the frequency domain model, precomputed with a lumped mass method imposing a sinusoidal motion at the fairlead. It highlights the importance of computing the added impedance for the corresponding motion amplitude. It is stated that the

method can be extensively used to control the mooring influence on the wave energy converter performance but a faster method for impedance computation may be convenient.

K. Larsen et al.[21] Presents two frequency domain methods for the calculation of the dynamic tension of single and multiple segment mooring lines. One based on the catenary equations and an estimation of the line drag resistance and a second method based on a single degree of freedom dynamic system per mooring line that accounts for lines' drag and inertia loads. Good agreement for a wide range of mooring configurations was found for the second method for floater motions and line tensions.

Y. M. Low et al.[22] A numerical model of both floater and lines dynamics in both frequency and time domain was introduced. It is based on the linear potential flow and the lumped mass method respectively. It builds up the mass, stiffness and damping matrices to represent lines structural properties, coupled with the floater dynamics. The geometric non-linearity is linearized computing the tangent stiffness around the mean position of the platform and the viscous drag term is also linearized by means of harmonic or statistical linearization. It has been applied to a floating platform moored in ultra-deep waters, expecting the geometric non-linearity to be not significant. Very good agreement is found between the non-linear time domain method and the commercial software Orcaflex as well as between the linearized model and the non-linear time domain, both in terms of floater motions and line tensions. In addition, the same authors suggested a hybrid *TD* and *FD* methods [23] for intermediate water depths, i.e. 200m, as the geometric non-linear stiffness is more relevant in lower water depths, showing accurate results.

### 1.3 Outline of the Thesis

The focus is to identify and propose numerical models for floater motions and mooring lines loads, applied to catenary moored heaving wave energy converters at early stages of development. It is broken down into three main parts, a state of the art in recent developments and numerical modelling (Chapter 2), the identified and proposed linearized



models (Chapter 3) and the main results that support the conclusions (Chapter 4, Chapter 5 and Chapter 6).

Chapter 2. It is composed of two main parts. The first section introduces the wave energy potential identified by several authors along with a description of the main types of wave energy technologies. Some of the most relevant technologies developed so far are introduced. Then a review of the state-of-the-art techniques for numerical modelling of the resource, floating structures and catenary mooring systems has been included. An introduction to numerical modelling methods of kinematic constraints is also added, that will be used in the subsequent chapters.

Chapter 3. The four numerical models developed in this thesis are introduced. Specifically, the Dynamic Linearized Frequency Domain model is the most relevant contribution of this thesis. A second section about the numerical models of the floating structures used in the thesis as case studies is also added.

Chapter 4. Main results of a comparison of numerical approaches for a heaving wave energy converter, subject to extreme environmental conditions, are introduced. It provides the ranges of applicability of each numerical approach for both floater motions and mooring lines' loads.

Chapter 5. Tank testing validation of the herein developed non-linear lumped mass model fully coupled to a floating structure is introduced. The validation has been carried out with tank test results of a catenary anchor leg moored (*CALM*) buoy in four main phases: decay tests without mooring system, decay tests with mooring system, mooring loads analysis with prescribed motions and structure and mooring system analysis with fully coupled simulations.

Chapter 6. The verification results of the herein proposed and developed Dynamic Linearized Frequency Domain model are introduced. The verification has been carried out with the non-linear lumped mass and floater dynamics coupled model, applied to a heaving floating wave energy converter.

## 1.4 Main Contributions

The main contributions of this thesis are subsequently mentioned and described:

- A critical comparison between the most commonly used approaches for floating structure and mooring system analysis has been performed, applied to a floating spar-type *WEC*. It shows that the most simplified numerical approaches can be used for optimization purposes in early stages, for mooring lines with a relatively low pretension. In addition, it shows the need to account for lines drag and inertia for appropriate mooring line tension estimates.
- A fully coupled floating structure and mooring lines numerical tool has been developed, and subsequently validated with a tank testing campaign of a *CALM* buoy. Results over a wide range of sea states show that the mooring model is very accurate while the higher uncertainty of the coupled model comes mainly from the floating structure.
- The linearization of the floating structure and dynamic mooring system coupled tool, to be solved in the frequency domain, has been developed and verified with its non-linear time domain counterpart, applied to a floating spar-type *WEC* in operational conditions. It shows good agreement in general and enables coupled eigenmode analysis. It is a tool two orders of magnitude faster than non-linear time domain techniques to solve body motions and mooring line dynamic induced tensions.

1991-2014



Universidad  
del País Vasco

Euskal Herriko  
Unibertsitatea

## Chapter 2

# State of the Art

### 2.1 Introduction

This chapter provides an overview of some of the most advanced *WEC* technologies along with the most used numerical modelling methods. The variety of typologies of *WECs* is significant and adapted numerical tools, that appropriately represent *WEC* motions, are needed in order to reduce the numerical modeling efforts in early stages, both for performance assessment and load estimates. On the other hand, there are already mature numerical methods for resource, body motions and mooring numerical modelling that have been used in the offshore industry for years. Section 2.3 collects the most relevant numerical modelling methods for *WEC* motions as well as for mooring loads analysis. In addition, a commonly used method to set constraints in numerical analysis of mechanisms is also included, that is used in subsequent chapters to couple floating bodies that compose *WECs* and the *WEC* itself with its corresponding mooring lines.

### 2.2 Marine Renewable Energy. Wave Energy Technology Potential and Development

Marine renewable energy is a promising source of energy with a large potential to be commercialized. It can be considered as any kind of energy that can be found and converted from marine water. There is currently a significant research and technology development effort being carried out focused on different kinds of marine energy. Some of them are:

- Tidal Range and Tidal Stream

- Ocean Thermal Gradient Energy Conversion
- Salinity Gradient or Osmotic Power
- Wave Energy

Other kinds of energy that can be harnessed in the oceans and also currently under development are:

- Submarine geothermic power
- Marine biomass
- Offshore Wind

Wave energy resource potential, represented in Figure 1, at a world scale is estimated to be of the order of magnitude of the world energy consumption and probably 10-25% of that resource can be exploitable [24].

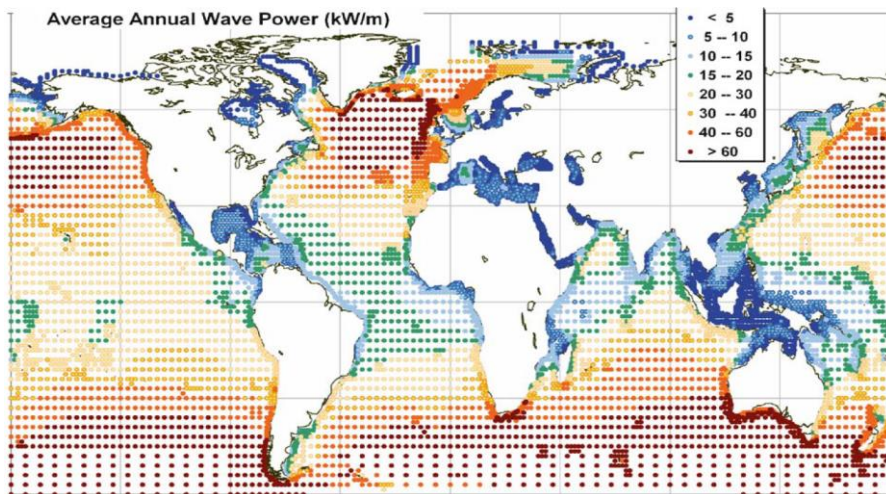


Figure 1 Estimated Average Annual Wave Power per meter of incoming wave front. Courtesy of J. Cruz [24]

The available power on the shores of many countries, interested in developing clean and renewable energy, boosts wave energy development creating small but promising companies to develop technologies for wave power conversion.

The challenge of wave power conversion comes up at the very beginning of the design phase as there is not a demonstrated best technology yet. Therefore, even though there are currently some promising developments at the technology demonstration phase, a significant portion of the research is focused on the working principle of the technology in order to find the one that demonstrates feasible forecasts of the *LCOE*, able to compete with the already commercial renewable energy generation technologies.

The largest untapped potential can be found in waters deeper than 50m. For this reason, the mooring system is a key technical aspect to be analysed and solved. Moreover, the station keeping system must assure device positioning while maintaining power production levels. Therefore, sizing the mooring system entails a challenge as size and device motions are significantly different to those of the traditional offshore industry, yet considered as unmanned permanent structures.

### ***2.2.1 Wave Energy Conversion Technologies***

Many different technologies have been analysed and tested so far, based in different principles. The most common ones have been collected in [25] and are represented in Figure 2.

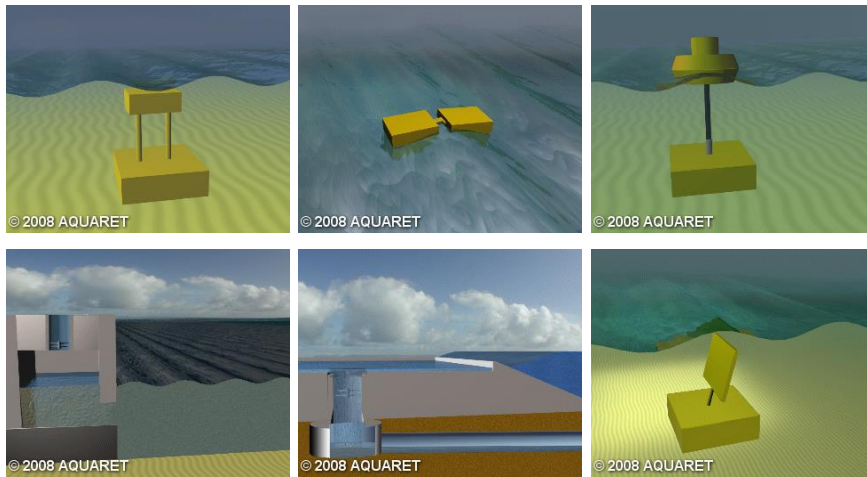


Figure 2 Main Wave Energy Conversion technologies. From top left to bottom right: Submerged pressure differential, Attenuators, Surface point absorber, Oscillating water column, Overtopping devices and Oscillating wave surge converters. Courtesy of *Aquaret* [25]

These wave energy conversion principles are also described in the same reference as follows:

- Submerged pressure differential devices capture energy from pressure change as the wave moves over the top of the device causing it to rise and fall.
- Attenuators are floating devices that are aligned perpendicular to the waves. These devices capture energy from the relative motion of the two arms as the wave passes them.
- Surface point absorbers are floating structures that can absorb energy from all directions. They convert the motion of the buoyant top relative to the base into electrical power.
- Oscillating water column technologies convert the rise and fall of waves into movements of air flowing past turbines to generate power.
- Overtopping devices have a wall over which waves break into a storage reservoir which creates a head of water. The water is released back to the sea through a turbine to generate power.

- Oscillating wave surge converters are near-surface collectors, mounted on an arm which pivots near the seabed. The water particles in the waves cause the arm to oscillate and generate power.

A significant number of wave energy converters, based on the principles showed in Figure 2 or a combination of them, have been developed so far showing acceptable energy production capacity, many of them based on floating structures.

Some of the most relevant technologies developed during last years have been the Pelamis Wave power device [26] and the Oyster device by Aquamarine Power [27] that were an attenuator and an oscillating wave surge converter respectively.

In 2004, Pelamis Wave Power, showed in Figure 3, demonstrated their first full-scale prototype, the P1, at EMEC’s wave test site at Billia Croo. Here, the P1 became the world’s first offshore wave power converter to successfully generate electricity into a national grid. The device was 120m long, 3.5m in diameter and comprised four tube sections. The first P2 machine, P2-001, was ordered by E.ON UK in 2009: the world’s first wave power machine to be purchased by a utility company. Arriving in Orkney in July 2010, the 750kW P2 machine was successfully installed at the Billia Croo wave test site for the first time in October 2010. Following a three-year testing programme, the P2-001 returned to the ownership of Pelamis Wave Power, for continued demonstration alongside the ScottishPower Renewables owned P2-002. Unfortunately, Pelamis went into administration in November 2014, and Wave Energy Scotland now owns their assets and IP. The P2-001 has been dismantled.



Figure 3 Pelamis Wave power P2-001 device installed. Courtesy of EMEC [26]



The Oyster concept, showed in Figure 4, is an oscillating wave surge converter: a buoyant, hinged flap attached to the seabed at around ten metres depth, around half a kilometre from shore. This flap, which is almost entirely underwater, moves backwards and forwards in the near-shore waves. The movement of the flap drives two hydraulic pistons which push high pressure water onshore to drive a conventional hydroelectric turbine. Aquamarine Power deployed and tested two full-scale Oyster devices at EMEC: the 315kW Oyster 1 and the second-generation 800kW Oyster 800, spending in excess of £3M in Orkney and working with over 40 local businesses. Oyster 800 was grid-connected in June 2012 at EMEC’s Billia Croo test site until the test programme ended in 2015, when the company ceased trading.



Figure 4 Aquamarine power’s Oyster 800 device installed (left) and during its deployment (right). Courtesy of *EMEC* and *OffshoreWind.biz* [27] [28]

Some of the most relevant technologies currently under development are the Marmok device [29], owned by IDOM [30], the Ocean Energy buoy (OE buoy) owned by Ocean Energy Ltd and funded by the Government of Ireland and the US Department of Energy (DOE) [31] and the Corpower’s wave energy concept [32]. These concepts are at a technology demonstration stage and actively taking part in R&D funded projects.

IDOM is an international engineering, architecture and consultancy firm, headquartered in Bilbao, with more than 3000 professionals providing services in a large variety of areas. Their technology is an *OWC*, showed in Figure 5, basically made up of three parts: a floater that is excited by the effect of waves, a hollow cylinder that contains the water column and a lower ballast that provides stability and inertia.

The air flow produced by the relative motion of the buoy with respect to the internal water column is forced to pass through a bidirectional turbine located at the top of the floater. The turbine rotates in a single direction regardless of the direction of the air flow, allowing the generator to be directly coupled to the turbine shaft. Different control strategies are used to adjust and optimize the actions of the turbine for each sea state, as well as to protect it in the event of a storm.



Figure 5 MARMOK-A-5 device at open sea. Courtesy of *IDOM* [33]

OE Buoy is a wave power device that uses an *OWC* design, showed in Figure 6. It was deployed in half-scale test mode in Spiddal near Galway in Ireland for over two years between 2007 and 2009. In 2011 the model was redeployed at the same site, primarily as a data collector for the EU funded Cores Project [34]. There is currently a project to test an OE buoy featuring a 500kW turbine designed by Siemens Government Technologies that will undergo 12 months of open ocean, grid-connected testing at the US Navy's Wave Energy Test Site. One of the buoy's most distinguishing features is its 35 meter, 826-ton hull, which was fabricated throughout 2019.

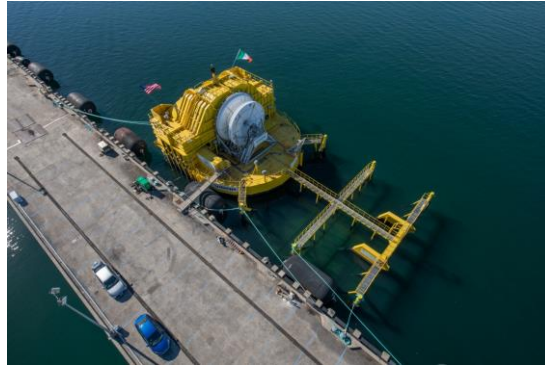


Figure 6 Ocean Energy buoy ready for deployment. Courtesy of *Sustainable Energy Authority Of Ireland* [31] and the *U.S. Office of Energy Efficiency & Renewable Energy* [35]

CorPower Ocean is a Swedish SME and their Wave Energy Converters are point absorber type, see Figure 7, with a heaving buoy on the surface absorbing energy from ocean waves. The buoy is connected to the seabed using a tensioned mooring system. The company states that their novel phase control technology makes the compact devices oscillate in resonance with the incoming waves, strongly amplifying the motion and power capture.

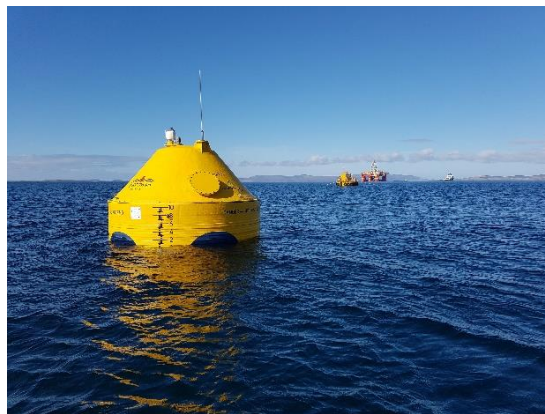


Figure 7 CorPower Ocean technology at open sea. Courtesy of *CorpowerOcean* [32]

In addition to past and current developments already mentioned, the Mutriku Wave power plant [36] has been delivering wave power to the

grid since it was inaugurated in July 2011 and it is the first wave power plant in Europe to sell the energy it generates. It is integrated in a breakwater in Mutriku town in the Basque Country and has 16 pneumatic turbines that can generate 296 kW of power, see Figure 8. The turbines operate using *OWC* technology, based on the creation of air flow from the changing level of water inside a chamber due to the movement of the waves.



Figure 8 Breakwater in which the fixed *OWC* chambers are integrated (left) and some drivetrains mounted over the corresponding chambers (right). Courtesy of *Ente Vasco de la Energía* [36]

When accounting for all cost items of wave energy devices, such as the structure, power take off (*PTO*), the mooring system or operation and maintenance (*O&M*) costs, the forecasted *LCOE* turns out to be not yet competitive with the current renewable energy market. The mean *LCOE* forecasted for different Wave Energy devices is ranged in 182-636€/MWh [37], in contrast with the price of the electricity in Spain during the year 2019, that was within the range of 45-75€/MWh, as shown in Figure 9.

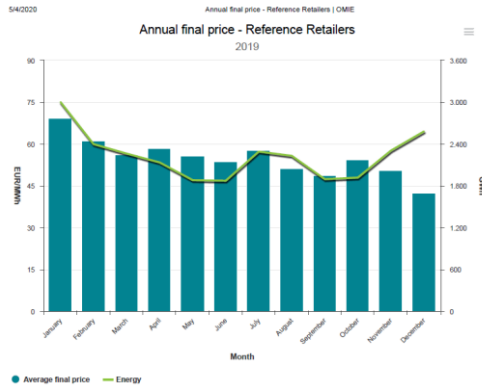


Figure 9 Annual electricity price in Spain during the year 2019. Courtesy of *Operador del Mercado Ibérico de Energía* [38]

As a consequence of the cost estimates, it seems important to keep track of the *LCOE* forecasts, along with good performance power levels, as *WEC* concepts are further developed. These approaches are being considered by a number of authors as [39] or [40], that assess the technology performance in terms of cost and power performance as it progresses through the technology readiness levels (*TRLs*). Alongside these works, there are ongoing European Union funded projects, such as [41], to identify the innovation paths for *WECs* and tidal energy converters with solid technical tools for the performance assessment.

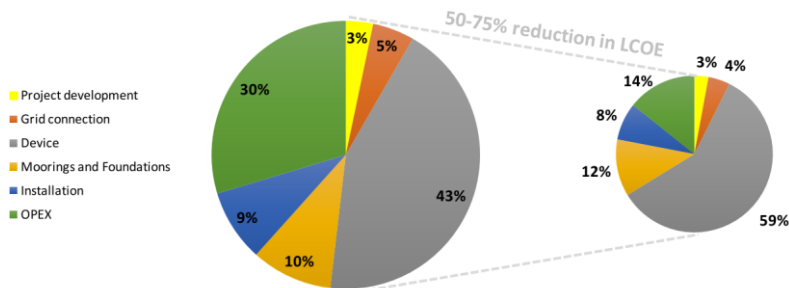


Figure 10 Wave *LCOE* Percentage Breakdown by Cost Centre Values at Current Stage of Deployment (Left) and the commercial Target (Right). *International Energy Agency – Ocean Energy Systems* [42]

In Figure 10 an estimation of the cost breakdown is provided in which the most relevant cost items are identified when evaluating the *LCOE* of *WEC* devices. It is shown that the device structure, *O&M* and the mooring system are the most influencing cost items. Additionally, a commercial target cost has been provided in which a 50-75% reduction is envisaged, mostly based in *O&M* cost reductions but with an increasing relative cost of mooring systems, up to a 12%.

This provides a reasonable framework to do research on numerical modelling approaches for mooring systems of *WECs* so that appropriate cost and performance estimates can be carried out from the very beginning of the technology development.

### ***2.2.2 Types of Mooring Systems***

There is a large variety of mooring configurations that can be used for any floating offshore structure. Most of them can be classified within catenary, semitaught and taut moorings, however these three main groups can be broken down into a larger number as represented in Figure 11.

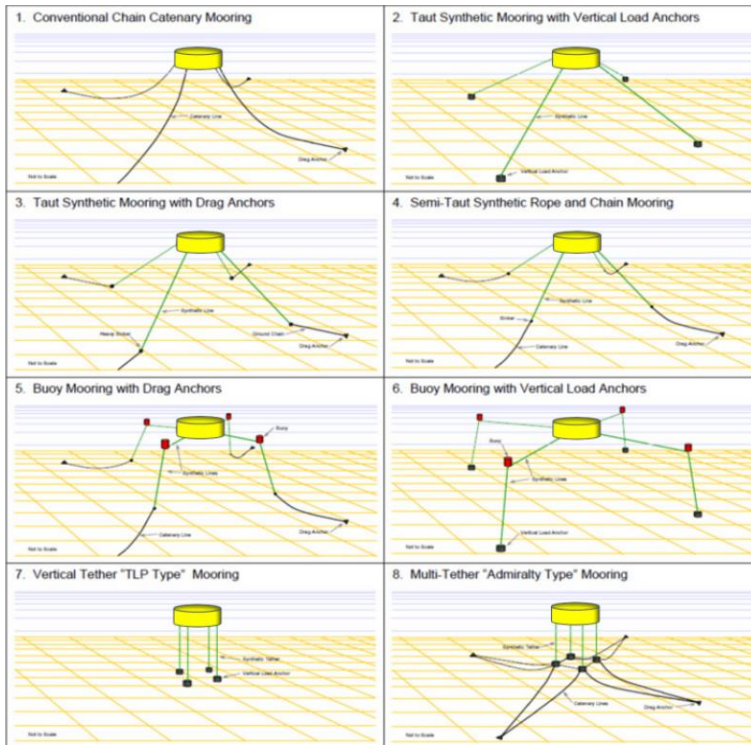


Figure 11 Most common mooring configurations used for offshore structures.  
*Courtesy of Reliability in a Sea of Risk (RisSoR) project [43]*

In general, taut mooring systems need structures with very large floatability to keep the tension on mooring lines under all conditions and avoid them going slack, with the subsequent snap loads and the risk they imply. Nevertheless, the structure is kept in position in a very stable vertical position and the area used by the mooring system is significantly reduced, compared with catenary mooring systems. Non-vertical taut mooring systems guarantee very stable horizontal positions but tend to enlarge the footprint.

Mooring systems based on catenary lines require larger footprints, however, the structure is kept in position through lifted line sections from the seabed that are translated into horizontal forces on the fairleads. These mooring systems are not as exposed to snap loads as long as a significant weight is kept hanging from the fairlead.

It is very common to combine chain sections with synthetic ropes that rises the tension and add negligible weight to the line, especially relevant for increasing water depths. Therefore, chain sections are mostly used to be on the seabed and lifted to balance horizontal forces on the moored structure. This effect is commonly known as the geometric non-linear stiffness.

Mooring systems based on catenary lines are usually subdivided into spread mooring systems, turret mooring systems or with a single line moored to *CALM* buoy, as represented in Figure 12, among others. General definitions for the three of them can be found in [44]:

- Spread mooring systems are multi-point mooring systems that moor vessels to the seabed using multiple mooring lines.
- Turret mooring systems consists of a turret assembly that is integrated into a vessel and permanently fixed to the seabed by means of a mooring system. The turret system contains a bearing system that allows the vessel to rotate around the fixed geostatic part of the turret, which is attached to the mooring system.
- The single point mooring buoy consists of a buoy that is permanently moored to the seabed by means of multiple mooring lines. The buoy can contain a bearing system that allows a part of it to rotate around the moored geostatic part.

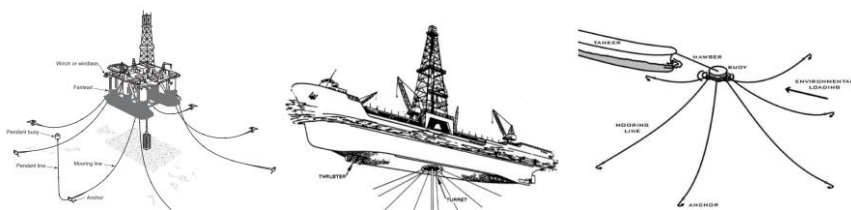


Figure 12 Spread mooring system (left), turret mooring system (center) and *CALM* Buoy (right). Courtesy of *American Petroleum Institute* [45]

All the above-mentioned systems can be analysed with the same numerical methods based on static, dynamic or hybrid approaches. The work here presented is focused on spread mooring systems based on catenary anchor lines.



## 2.3 Numerical Modeling Methods

Floating *WECs*, unlike other offshore structures, are designed so that their response, excited by sea waves, is amplified. It implies mooring lines to be highly excited too and, therefore, a strong coupling between mooring line and structure dynamics can be expected. On one hand the tensions induced by structure dynamics are to be considered, since it may lead to significant costs of the mooring system. On the other hand, mooring line interaction with the power conversion system should be considered, especially when it is not an active part of the conversion system. The latter case is the most common situation, which all designers must face at the corresponding stage of development, sometimes realizing that the cost of the installation and the mooring components may be unexpectedly high.

Mooring analysis should be carried out in accordance to the design stage of the technology. Several approaches have been proposed to analyze mooring systems in general, most of them based on either static or dynamic models, assuming the structure to be modelled through its rigid-body degrees of freedom (*DOF*). The most widespread approach is the lumped mass model, coupled to a floater modelled through the boundary element method (*BEM*), based on the potential flow theory. Nevertheless, early design stages require fast approaches, especially for fatigue assessments, that may provide acceptable estimates for many configurations, although not as accurate as the lumped mass.

In this section the most widely used numerical modelling techniques for the wave resource, floating structures and for mooring lines are introduced. The models herein presented for floating structures are mainly based on the potential flow theory and the Morison forces.

### 2.3.1 Resource Modelling

The resource is the first step for design and modelling of any offshore structure. It sets the basis for power production as well as for extreme event stress on different components, derived from the corresponding motions. The wave numerical modelling is described very briefly in this section. Resources are described in different time scales, in the short term, i.e. time series of a sea state, and in the long term, through the

probability of occurrence of each sea state in a specific site. The latter corresponds to what is commonly known as the scatter diagram, what characterizes the wave resource of the corresponding site.

### 2.3.1.1 Short term Waves. Wave Spectrum

A sea state can be characterized through its spectral shape, that provides the energy distribution in frequency. Therefore, it can be modelled as a sum of several regular waves with its corresponding frequency, amplitude and phase.

Regular waves are supposed to have a sinusoid profile and a plane wave front, as represented in Figure 13.

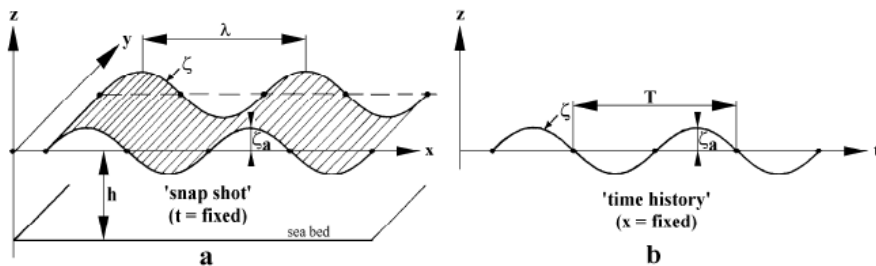


Figure 13 Plane progressive regular wave propagation. Courtesy of Ø. A. A. HARALD and E. KROGSTAD [46]

Where:

- $h$ : water depth
- $\eta$ : Surface elevation
- $\eta_a$ : amplitude of Surface elevation
- $\lambda$ : wavelength

Therefore, the water surface elevation at a given point can be represented by:

$$\eta(t) = \eta_a \cdot \cos(\omega \cdot t + \varphi_x) \quad 2.3.1$$

Alternatively, with the Euler formula it is expressed as:

$$\eta(t) = \text{Re}\{\eta \cdot e^{i(\omega \cdot t + \varphi_x)}\} = \text{Re}\{\hat{\eta} \cdot e^{i \cdot \omega \cdot t}\} \quad 2.3.2$$

In case of gravity waves a relation is established between the frequency and wavelength, the so called *dispersion relation* [46]–[48]. It is defined as:

$$\omega^2 = g \cdot k \cdot \tanh(kh) \quad \text{where:} \quad k = \frac{2 \cdot \pi}{\lambda} \quad 2.3.3$$

The term  $(kh)$  represents the relation between the water depth and the wavelength. It indicates that waves of the same frequency will have larger wavelengths in deep waters than in shallow waters. Therefore, the propagation speed, or phase velocity, of water waves  $\left(\frac{\lambda}{T} = \frac{\omega}{k}\right)$  is lower in shallow waters.

It can then considered that [48]:

- Deep waters:  $h > \lambda/2$
- Shallow waters:  $h < \lambda/20$

If wave velocity fields are resolved for a plane progressive wave, next equations are obtained for shallow 2.3.4 and deep waters 2.3.5 respectively [48].

$$u(x, z, t) = \eta_a \cdot \omega \cdot \frac{\cosh(k \cdot (h + z))}{\sinh(k \cdot h)} \cdot \sin(\omega \cdot t - k \cdot x) \quad 2.3.4$$

$$w(x, z, t) = \eta_a \cdot \omega \cdot \frac{\sinh(k \cdot (h + z))}{\sinh(k \cdot h)} \cdot \cos(\omega \cdot t - k \cdot x)$$

$$u(x, z, t) = \eta_a \cdot \omega \cdot e^{k \cdot z} \cdot \sin(\omega \cdot t - k \cdot x) \quad 2.3.5$$

$$w(x, z, t) = \eta_a \cdot \omega \cdot e^{k \cdot z} \cdot \cos(\omega \cdot t - k \cdot x)$$

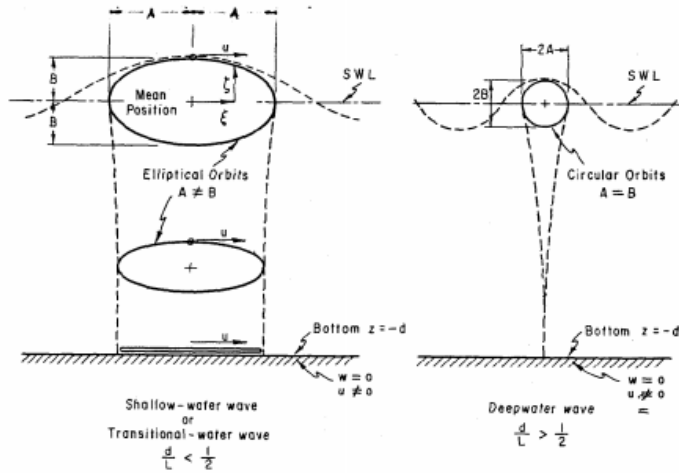


Figure 14 Wave particle velocity profiles in shallow waters (left) and deep waters (right). Courtesy of Ø. A. A. HARALD and E. KROGSTAD [46]

Water wave particle motions are circular in deep waters and become elliptical as they approach to shallower waters, as represented in Figure 14. Therefore, the seabed influence on wave kinematics can be appreciated as the hyperbolic tangent in the dispersion relation is notably lower than the unity.

The potential energy contained in a water column within a sea wave at a defined time is [46]:

$$dE_p = \int_{z=0}^{z=\eta} \rho \cdot g \cdot z \cdot dV = dA \cdot \int_{z=0}^{z=\eta} \rho \cdot g \cdot z \cdot dz = dA \cdot \rho \cdot g \cdot \frac{\eta^2}{2} \quad 2.3.6$$

In regular waves the water surface elevation can be replaced by its harmonic expression. Then using its mean value ( $\overline{\eta^2} = \frac{\eta_a^2}{2}$ ) the potential energy per horizontal unit area yields:

$$\left\langle \frac{dE_p}{dA} \right\rangle = \rho \cdot g \cdot \frac{\eta_a^2}{4} \quad 2.3.7$$

The kinetic energy can be expressed in the same terms:

$$dE_k = \int_{z=-h}^{z=\eta} \frac{1}{2} \cdot \rho \cdot (u^2 + v^2 + w^2) \cdot dV \quad 2.3.8$$

The velocity components, for plane progressive waves and deep waters, can be replaced by:

$$(u^2 + v^2 + w^2) = (\eta_a \cdot \omega \cdot e^{k \cdot z})^2 \quad 2.3.9$$

Which yields:

$$\begin{aligned} dE_k &= \int_{z=-h}^{z=\eta} \frac{1}{2} \cdot \rho \cdot (\eta_a \cdot \omega \cdot e^{k \cdot z})^2 \cdot dV \\ &= dA \cdot \frac{1}{2} \cdot \rho \cdot (\eta_a \cdot \omega)^2 \cdot \int_{z=-h}^{z=\eta} e^{2 \cdot k \cdot z} \cdot dz \\ &\cong dA \cdot \frac{1}{2} \cdot \rho \cdot (\eta_a \cdot \omega)^2 \cdot \int_{z=-\infty}^{z=0} e^{2 \cdot k \cdot z} \cdot dz \\ &= dA \cdot \frac{1}{2} \cdot \rho \cdot (\eta_a \cdot \omega)^2 \cdot \frac{1}{2 \cdot k} \end{aligned} \quad 2.3.10$$

Applying the dispersion relation for deep waters the mean kinetic energy per unit horizontal surface is obtained:

$$\left\langle \frac{dE_k}{dA} \right\rangle = \rho \cdot g \cdot \frac{\eta_a^2}{4} \quad 2.3.11$$

As it is shown the kinetic and potential energy contained in each regular wave take the same value, which are carried along with the wave as it travels. It can be assumed that real waves, made up of a sum of harmonic waves, are propagated making *groups* and the energy does so. Those groups are propagated with the group velocity, lower than the regular wave velocity, more precisely, using the dispersion relation in deep waters [46], equation 2.3.12 is obtained.

$$c_g = \frac{\omega_2 - \omega_1}{k_2 - k_1} = \frac{d\omega}{dk} = \frac{g}{2 \cdot \omega} = \frac{c_p}{2} \quad 2.3.12$$

The energy contained in a wavelength per meter of wavefront is:

$$\langle E_k + E_p \rangle = 2 \cdot \rho \cdot g \cdot \frac{\eta_a^2}{4} \cdot c_g \cdot T \quad 2.3.13$$

Which, per unit of time, yields a wave power per meter of wavefront [46], which is called by different authors as *energy transport*, *energy flux* or *power flux*.

$$J = \langle E_k + E_p \rangle = \frac{\rho \cdot g^2}{4 \cdot \omega} \cdot \eta_a^2 \left[ \frac{W}{m} \right] \quad 2.3.14$$

Real seas are never composed of pure regular waves, they are made up of several regular waves over a range of frequencies instead, as showed in equation 2.3.15.

$$\eta(t) = \sum_{n=1}^{\infty} Re\{\hat{\eta}_{an} \cdot e^{i\omega_n \cdot t}\} \quad 2.3.15$$

One can assume the wave surface elevation time series as described in the Figure 15.

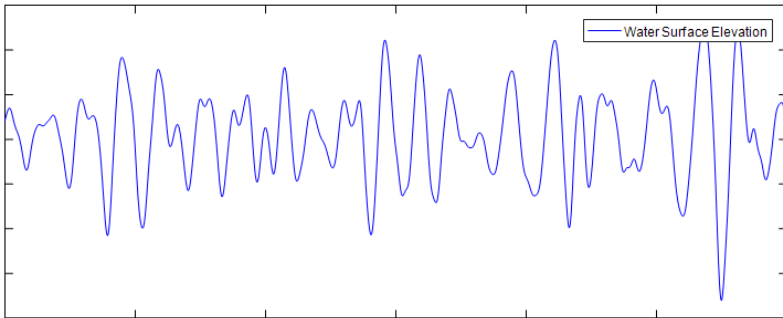


Figure 15 Wave surface elevation of a real sea

The sampling period is  $\Delta t$  and  $N$  is the number of samples recorded, therefore the total sampling time is:

$$\tau = \Delta t \cdot N \quad 2.3.16$$

The variance of the recorded signal, supposed to be of a zero-mean value, can be computed as:

$$\sigma_{\eta}^2 = \bar{\eta}^2 = \frac{1}{N} \cdot \sum_{n=1}^N \eta_n^2 = \frac{1}{N \cdot \Delta t} \cdot \sum_{n=1}^N \eta_n^2 \cdot \Delta t = \frac{1}{\tau} \cdot \int_0^{\tau} \eta^2(t) dt \quad 2.3.17$$

If it is supposed that the signal is composed of N harmonic functions:

$$\begin{aligned} \sigma_{\eta}^2 &= \frac{1}{\tau} \cdot \int_0^{\tau} \eta^2(t) dt = \frac{1}{\tau} \cdot \int_0^{\tau} \left\{ \sum_{n=1}^N \eta_{an} \cdot \cos(\omega_n \cdot t - k_n \cdot x + \varphi_n) \right\}^2 dt \\ &= \sum_{n=1}^N \frac{1}{2} \cdot \eta_{an}^2 \end{aligned} \quad 2.3.18$$

The wave spectrum is then defined as in equation 2.3.19.

$$S(\omega_n) d\omega = \frac{1}{2} \cdot \eta_{an}^2 \quad 2.3.19$$

Looking at the spectrum definition, the wave amplitude corresponding to each frequency component of the wave spectrum is defined in equation 2.3.20. Therefore, it enables building up time series of the wave elevation through the inverse fourier transform, applying random phases ( $\varphi_n$ ) to each frequency component.

$$\hat{\eta}_{an} = \sqrt{2 \cdot S(\omega_n) \cdot \Delta\omega} \cdot e^{i \cdot \varphi_n} \quad 2.3.20$$

The wave elevation is considered to be a Gaussian process and, consequently all wave heights within a sea state are Rayleigh distributed [48], [49] and as such can be statistically analysed. It also yields equivalent distribution of dynamics of offshore structures as long as models are linear or, to a lesser extent, linearized. A realistic wave spectrum is generally defined through its significant wave height ( $H_s$ ) and a characteristic period, mostly  $T_p$  (peak period). There several theoretical sea states defined that model realistic seas, such as JONSWAP defined in equation 2.3.21 for  $\gamma = 3.3$ , Pierson-Moskowitz or the Bretschneider spectra.

$$S_{\eta}(\omega) = \frac{320 \cdot H_s^2}{T_p^4} \cdot \omega^{-5} \cdot e^{\frac{-1950}{T_p^4} \omega^{-4}} \cdot \gamma^A$$

$$A = e^{-\left(\frac{\frac{\omega}{\omega_p} - 1}{\sigma \sqrt{2}}\right)^2}$$

2.3.21

Taking the JONSWAP spectrum with  $\gamma^A = 1.522$  it becomes the Bretschneider spectrum. The Bretschneider spectrum is also known as the Modified Two-Parameter Pierson-Moskowitz spectrum, whereas the original, one-parameter Pierson-Moskowitz spectrum is obtained with the Bretschneider spectrum assuming the peak period and significant wave height relation of  $0.772 \cdot T_p = 3.86 \cdot H_s$  [48].

### 2.3.1.2 Long term Waves. Wave Climate

A wave climate of any site can be characterized through the occurrence of irregular sea states of combined  $H_s$  and  $T_p$ . A two-dimensional representation is therefore needed. It is represented by means of the scatter diagram of sea states occurrence, as introduced in Figure 16.

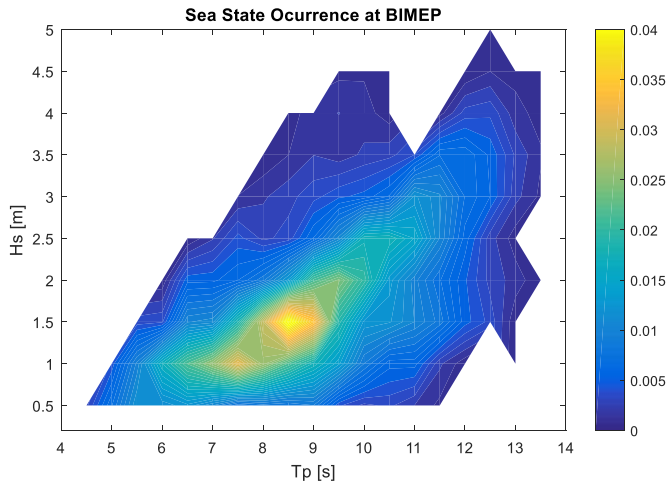


Figure 16 Occurrence matrix in the BIMEP area. Courtesy of *BIMEP* [50]



Good knowledge of the wave climate is recommended so that the load cases for design of different offshore structures are well defined avoiding technical risks and large oversizing of components. For a precise scatter diagram and statistical properties, it is recommended that at least 10 year of data are available [51]. In order to assess the power production of *WECs* the International Electrotechnical Commission (*IEC*) provides guidelines on how to group the measured sea states in a given location [52].

In addition to the wave climate, extreme statistics are very relevant for mooring design and analysis. The station keeping system must be able to withstand the expected extreme environmental conditions along the design life. The estimates of such conditions are carried out through extreme statistics that provide significant wave height and peak period combinations with the same probability of occurrence. Such combinations are defined through  $H_s$  and  $T_p$  contours with the same probability of occurrence, characterized by the return period. It indicates the period of time in which the  $H_s$  and  $T_p$  combinations would occur once in the site under analysis. In detailed designs several points of the corresponding contour are analysed and ideally a contour per direction for the same return period is desirable. The *IEC* also is working on providing guidelines about the design load cases for moorings of *WECs* [53] and for the more generic offshore industry DNV GL provides design guidelines for moorings [18] as well as the API [54] or BV [55]. Depending on the type of structure, standardization bodies recommend combinations of extreme sea states, current and wind, each with its corresponding return period.

### ***2.3.2 Wave Structure Interaction***

The interaction between waves and structures can be modelled via the linear potential flow method, extensively used within the offshore industry and is well described in [56] and [57]. It assumes inviscid and irrotational flow as well as small wave amplitudes compared to the wavelength, which leads to linearized kinematic and dynamic free surface boundary conditions. This is a good approximation as sea waves are dominated by inertia and gravity forces, especially for large

structures, with small Keulegan Carpenter ( $KC$ ) numbers. However, this is not always the case, in more severe ocean conditions drag forces plays a more relevant role. Therefore, the linear potential flow is most times complemented with non-linear drag forces for intermediate  $KC$  numbers giving in general good results. Additionally, in high or extreme wave heights the full Morison equation is commonly used.

The most common axis convention is to consider the  $XY$  plane on the surface water level ( $SWL$ ) with the  $Z$  axis positive upwards, as represented in Figure 17. This convention has also been assumed in this thesis.

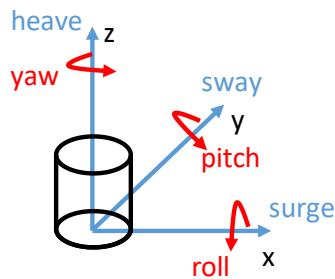


Figure 17 Axis conventions assumed in this thesis

### 2.3.2.1 Cummins equation

This section is an introductory part to the equation of motion derived for floating structures interacting with sea waves [48]. Dynamics of floating bodies, activated by time varying sea wave loads, are governed by the so called *Cummins Equation* [58] which is derived below. Complex potential problems can be handled via the frequency dependent linear hydrodynamic coefficients [59], also introduced in this section.

Any floating object is assumed to be a linear mechanical system with a translational (or rotational, here a one translational  $DOF$  model is derived for simplicity) velocity as input and the reaction force of the surrounding water as output. Assuming an impulsive displacement  $\Delta\delta$  with a constant velocity  $\dot{\delta}$  of the structure, the following expression can be written:

$$\Delta\delta = \dot{\delta} \cdot \Delta t \quad 2.3.22$$

During this displacement, water particles will start to move. Since linear potential flow is assumed, a velocity potential  $\Theta$ , proportional to the velocity can be assumed:

$$\theta = \Psi \cdot \dot{\delta} \quad 2.3.23$$

Where  $\Psi$  is the normalized velocity potential.

The water particles are still moving after the impulsive displacement. As the system is assumed to be linear, motions of the fluid, described by the velocity potential, are proportional to the impulsive displacement:

$$\theta = \chi(x, y, z, t) \cdot \Delta\delta \quad 2.3.24$$

Where  $\chi$  is another normalized velocity potential.

A general conclusion can be that the impulse influences the motion of the fluid during time intervals afterwards, therefore it can be said that the system has a form of memory.

Any arbitrary motion of the floating structure can be represented as a succession of small impulsive displacements, so that the resulting total velocity potential  $\Theta(t)$ , during the interval  $(t_m, t_m + \Delta t)$  becomes:

$$\theta(t) = \dot{\delta}_m \cdot \Psi + \sum_{k=1}^m \{ \chi(t_{m-k}, t_{m-k} + \Delta t) \cdot \dot{\delta}_k \cdot \Delta t \} \quad 2.3.25$$

Where:

- m: number of time steps

-  $t_m$ :  $t_0 + m \cdot \Delta t$

-  $t_{m-k}$ :  $t_0 + (m - k) \cdot \Delta t$

-  $\dot{\delta}_m$ : Velocity component during the time interval  $(t_m, t_m + \Delta t)$

-  $\dot{\delta}_k$ : Velocity component during the time interval  $(t_{m-k}, t_{m-k} + \Delta t)$

- $\Psi$ : Normalized velocity potential caused by a displacement during time interval  $(t_m, t_m + \Delta t)$
- $\chi$ : Normalized velocity potential caused by a displacement during time interval  $(t_{m-k}, t_{m-k} + \Delta t)$

Letting  $\Delta t$  go to zero yields:

$$\theta(t) = \dot{\delta}(t) \cdot \Psi + \int_{-\infty}^t \chi(t - \tau) \cdot \dot{\delta}(\tau) \cdot d\tau \quad 2.3.26$$

In which  $\dot{\delta}(\tau)$  is the velocity component of the body at time  $\tau$ .

The pressure in the fluid follows from the linearized Bernoulli equation:

$$p = -\rho \cdot \frac{\partial \theta}{\partial t} \quad 2.3.27$$

An integration of the pressures over the wetted surface,  $S$ , yields the expression for the hydrodynamic reaction force,  $F_h$ :

$$\begin{aligned} F_h &= - \iint_S p \cdot n \cdot dS = \rho \iint_S \frac{\partial \theta}{\partial t} \cdot n \cdot dS \\ &= \rho \iint_S \Psi \cdot \frac{\partial \dot{\delta}(t)}{\partial t} \cdot n \cdot dS \\ &\quad + \rho \iint_S \frac{\partial \int_{-\infty}^t \chi(t - \tau) \cdot \dot{\delta}(\tau) \cdot d\tau}{\partial t} \cdot n \cdot dS \end{aligned} \quad 2.3.28$$

Organising previous expression:

$$F_h = \rho \iint_S \Psi \cdot n \cdot dS \cdot \dot{\delta}(t) + \int_{-\infty}^t \left\{ \rho \iint_S \frac{\partial \chi(t - \tau)}{\partial t} \cdot n \cdot dS \right\} \cdot \dot{\delta}(\tau) \cdot d\tau \quad 2.3.29$$

Defining:

$$A = \rho \iint_S \Psi \cdot n \cdot dS \quad ; \quad B(t) = \rho \iint_S \frac{\partial \chi(t - \tau)}{\partial t} \cdot n \cdot dS \quad 2.3.30$$

The hydrodynamic force becomes:

$$F_h = A \cdot \ddot{\delta}(t) + \int_{-\infty}^t B(t - \tau) \cdot \dot{\delta}(\tau) \cdot d\tau \quad 2.3.31$$

The radiation force in equation 2.3.31 along with a linear restoring spring term (hydrostatic) and a wave excitation load,  $F_w(t)$  in the Newton's second law, yields the linear equation of motion in the time domain (*TD*), which is often referred to as *Cummins Equation* in honor of his work [58].

$$F_w - F_h - F_{rig} = M \cdot \ddot{\delta}(t) \quad 2.3.32$$

$$(M + A) \cdot \ddot{\delta}(t) + \int_{-\infty}^t B(t - \tau) \cdot \dot{\delta}(\tau) \cdot d\tau + K \cdot \delta(t) = F_w(t) \quad 2.3.33$$

The velocity potentials,  $\Psi$  and  $\chi$ , have to be found to determine A and B coefficients. The most common approaches to find A and B can be found in [59]. It consists in using the hydrodynamic mass and damping data determined using existing frequency domain computer programs based on potential theory, such as Nemoh [60], WAMIT [61] and AQWA [62].

Wave excitation forces can also be computed with the mentioned commercial codes, which compute the force on floating bodies due to the incoming waves (Froude Krylov forces) and to the diffraction induced by the body (diffraction forces) in the frequency domain, as described in [56] and [47]. As common commercial codes consider linear wave theory, forces are given per unit amplitude of the corresponding regular wave in case of the excitation force and motion for the radiation force.

Any floating object, subject to regular waves, can be assumed to carry out a harmonic oscillation, in stationary conditions, that for a unit amplitude are:

$$\begin{aligned} \delta(t) &= 1 \cdot \cos(\omega \cdot t) ; \dot{\delta}(t) = -1 \cdot \omega \cdot \sin(\omega \cdot t) ; \ddot{\delta}(t) \\ &= -1 \cdot \omega^2 \cdot \cos(\omega \cdot t) \end{aligned} \quad 2.3.34$$

Substitution of the harmonic motions into the Cummins equation yields:

$$\left( -\omega^2 \cdot (M + A) \cdot \cos(\omega \cdot t) - \omega \cdot \int_0^\infty B(\tau) \cdot \sin(\omega \cdot (t - \tau)) \cdot d\tau + K \cdot \cos(\omega \cdot t) \right) \cdot \hat{\delta}(\omega) = F_w(t) \quad 2.3.35$$

And reorganising:

$$\begin{aligned} -\omega^2 \cdot \left\{ M + A - \frac{1}{\omega} \cdot \int_0^\infty B(\tau) \cdot \sin(\omega \cdot \tau) \cdot d\tau \right\} \cdot \cos(\omega \cdot \tau) - \omega \cdot \left\{ \int_0^\infty B(\tau) \cdot \cos(\omega \cdot \tau) \cdot d\tau \right\} \cdot \sin(\omega \cdot \tau) + K \cdot \cos(\omega \cdot t) \\ = F_w(t) \end{aligned} \quad 2.3.36$$

A comparison of the classical frequency domain description of motions with the previous equation establishes the equivalency of the so called *Added Mass* (A) and *Radiation Damping* (B) coefficients in the frequency domain and in the time domain:

$$A(\omega) = A - \frac{1}{\omega} \cdot \int_0^\infty B(\tau) \cdot \sin(\omega \cdot \tau) \cdot d\tau \quad ; \quad B(\omega) = \int_0^\infty B(\tau) \cdot \cos(\omega \cdot \tau) \cdot d\tau \quad 2.3.37$$

Main characteristics of the radiation force coefficients are:

- Added Mass: For zero frequency takes a non-zero value and as the frequency approaches to large values the added mass tend to a constant value,  $A(\infty)$
- Radiation Damping: It is zero for zero frequency and tends to zero for large frequencies.

Both can exhibit peaks at discrete frequencies, which do not have any physical sense. Those frequencies appear in commercial packages when a double result is found for a defined frequency [61].

An inverse Fourier transform can be used to isolate the desired function  $B(\tau)$ . The coefficient A can be directly evaluated with a bit of algebra.

The *Radiation Impulse Response Function (RIRF)* and the mass term are described in equation 2.3.38.

$$B(\tau) = \frac{2}{\pi} \cdot \int_0^{\infty} B(\omega) \cdot \cos(\omega \cdot \tau) \cdot d\omega \quad 2.3.38$$

$$A(\tau) = A(\omega) + \frac{1}{\omega} \cdot \int_0^{\infty} B(\tau) \cdot \sin(\omega \cdot \tau) \cdot d\tau$$

This expression is valid for any value of omega, thus evaluating at  $\omega = \infty$  provides:

$$A = A(\infty) \quad 2.3.39$$

An example of the *RIRF*, of a heaving degree of freedom, is shown in Figure 18.

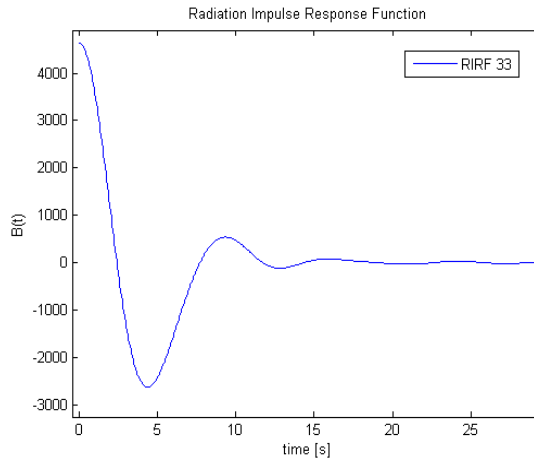


Figure 18 Radiation Impulse Response Function example in heave

The convolution term implies the integration from  $-\infty$  to the present time step  $t$ . That makes the problem hard to be handled in a practical way. Fortunately, *RIRFs* decay to zero along the time enabling the cutoff of the function after a sensible time lag. It is recommended to study the *RIRF* of each position of the matrix so that the cut off time is appropriately established.

In the degrees of freedom in which a hydrostatic restoring coefficient applies,  $K$ , it can be easily determined from the waterplane area, geometry and, when rotations in pitch and roll are involved, the center of gravity (*COG*) with respect to the buoyancy centre of the floating object. It has only influence on *DOFs* that have vertical components as heave, pitch and roll while there are no hydrostatic terms in sway, surge and yaw. Therefore, the hydrostatic stiffness matrix can be expressed as in equation 2.3.40.

$$[K_h] = \begin{bmatrix} 0 & 0 & 0 & 0 & 0 & 0 \\ 0 & 0 & 0 & 0 & 0 & 0 \\ 0 & 0 & K_{33} & K_{34} & K_{35} & 0 \\ 0 & 0 & K_{43} & K_{44} & K_{45} & 0 \\ 0 & 0 & K_{53} & K_{54} & K_{55} & 0 \\ 0 & 0 & 0 & 0 & 0 & 0 \end{bmatrix} \quad 2.3.40$$

It is then necessary to add to the structure a mechanism to implement a stiffness matrix to ensure its horizontal position is kept within certain limits. That is the main function of the mooring system as will be explained in section 2.3.3.

When solving the equation of motion of a floating structure the required information must be known beforehand so that the appropriate degrees of freedom of the system are considered. The longitudinal motions are, as described in Figure 17, surge, sway and heave while the rotational ones are roll, pitch and yaw along and about X, Y and Z axis respectively [47] [56].

Therefore, the solution of the floater either in the time or in the frequency domain may consider only the most relevant degrees of freedom of the floating structure in order to represent the parameters of interest, e.g. motions, power production or loads on components. Additionally, other degrees of freedom such as articulations between bodies may be considered which is carried out through kinematic restriction, to be introduced in section 2.3.4.

The Cummins equation expressed in the frequency domain for a one *DOF* system is composed of a mass, damping and a restoring coefficient terms, as shown in equation 2.3.41.



$$(-\omega^2 \cdot (M + A(\omega)) + i \cdot \omega \cdot B(\omega) + K_h) \cdot \hat{\delta}(\omega) = \hat{F}_w(\omega) \quad 2.3.41$$

Where:

- $M$ : The body mass, or moment of inertia in rotational degrees of freedom
- $A(\omega)$ : The so-called added mass, frequency dependent
- $B(\omega)$ : The radiation damping, frequency dependent
- $K_h$ : The hydrostatic restoring term
- $F_w(\omega)$ : Wave excitation force. Froude-Krylov and Diffraction force per unit wave amplitude
- $\hat{\delta}(\omega)$ : The complex amplitude of the response of the *DOF* in the frequency  $\omega$

As long as waves are assumed linear and with unit amplitude as in equation 2.3.41, the *FD* solution  $\hat{\delta}(\omega)$  represents the *Response Amplitude Operator (RAO)*, equivalent to the dynamic amplification factor for generic mechanical systems. The difference between both operators consists in expressing the amplification per unit wave amplitude in the former and per unit force amplitude in the latter.

*RAO* functions are applied as transfer functions when solving mechanical systems under the influence of irregular waves, or real sea states, as long as the system can be assumed linear, as expressed in equation 2.3.42.

$$S_\delta(\omega) = |RAO(\omega)|^2 \cdot S_\tau(\omega) \cdot d\omega \quad 2.3.42$$

Resolution of time domain models is only worth when non-linear terms are included such as control, viscous drag or mooring forces among others. However, before adding any non-linear term, the linear equation of motion, the Cummins equation 2.3.33, needs to be solved. It implies the computation of the convolution term at every time step, that can be carried out through different numerical methods, such as the ones explained below:

- Direct integration: It is usually applied the Runge-Kutta of fourth global order (RK4) or the trapezoidal method, which may not be as stable as the RK4 being computationally less time consuming. It consists in recording a time window of the velocity history and using the inversed *RIRF* (see Figure 19) as a filter to get the corresponding convolution term. Implicit methods for integration of ordinary differential equations may also be used such as the Wilson- $\Theta$ , Newmark or the Generalized-alpha methods, especially for stiff systems such as e.g. floating structure coupled with a discretized mooring system.

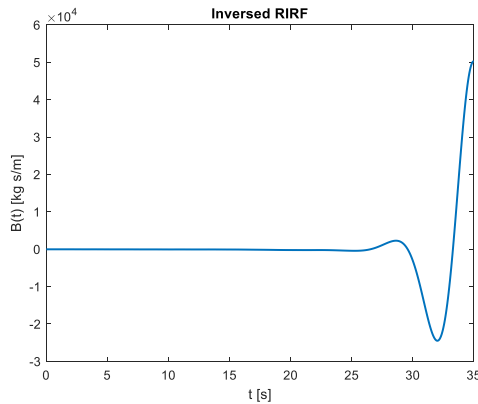


Figure 19 Inversed Radiation Impulse Response Function for direct integration of the convolution term

- Prony method: This method, suggested by [63], is an state space model which consists in approximating the *RIRF* as a sum of complex exponential functions, as showed in equation 2.3.43. The convolution integral term in the equation of motion 2.3.33 is replaced by a state space model, which represents how the force attributed to each of the exponentials is progressing along the time.

$$B(t) \approx \sum_{i=1}^N \alpha_i \cdot \exp(\beta_i \cdot t) \tag{2.3.43}$$

- Frequency Domain Identification method: This method was suggested by [64], it approximates the radiation coefficients in frequency

through a parametric function made up of two polynomials by means of least squares. A state space model is also built based on the coefficients of the mentioned polynomials.

$$K(s) = \frac{P(s)}{Q(s)} \text{ where } K(j\omega) = B(\omega) - j\omega \cdot [A(\omega) - A(\infty)] \quad 2.3.44$$

Any of the previous methods require the computation of the frequency domain radiation damping and added mass for all *DOFs* considered in the model. Depending on the body geometry and position of the center of gravity, strong coupling may exist between degrees of freedom and most of them might need to be included in the model, depending on the excitation force direction. It makes the number of *RIRFs* to increase significantly and, consequently, the number of convolution integrals to be computed. Even though state space models are efficient methods to compute the convolution and ease the implementation of variable time step integration methods, a trade off solution must be sought for various *DOF* models since the number of states may be dramatically increased with state space models.

### 2.3.2.2 Morison equation on slender elements

The Morison equation represents the hydrodynamic force on a submerged body, commonly applied for water particle force estimates on slender cylinders. It is computed as the superposition of a linear inertia force and a quadratic viscous drag force, as represented in equation 2.3.45.

$$F_{hyd}(t) = (1 + C_a) \cdot \rho_w \cdot V \cdot \dot{u}(t) - C_a \cdot \rho_w \cdot V \cdot \ddot{\delta}(t) + 0.5 \cdot \rho_w \cdot C_d \cdot D \cdot L_n \cdot |u(t) - \delta(t)| \cdot (u(t) - \delta(t)) \quad 2.3.45$$

Where:

- $\dot{u}(t)$  and  $u(t)$ : Local acceleration and velocity of fluid particles at each element section
- $\ddot{\delta}(t)$  and  $\dot{\delta}$ : Local acceleration and velocity of each element section
- $V$ : Volume of the corresponding section

- $D$ : Diameter of the corresponding section
- $L_n$ : Length of the corresponding section
- $C_a$ : Added mass coefficient
- $C_d$ : Viscous drag coefficient

It can be applied either to a fixed structure subject to waves and/or current, to a moving structure in waves and current or even to a moving structure in still water. It is applicable for a whole structure or at component level when it can be considered small compared with the wavelength ( $\lambda > 5D$ ) [51]. Therefore, it is commonly applied to compute forces on fixed jackets for offshore wind turbines, braces on large volume floating structures or on mooring lines and umbilical cables, necessary for floating offshore renewable technologies.

### 2.3.2.3 *Relevant non-dimensional numbers*

The most relevant non-dimensional numbers in floating structures subject to sea waves are the Froude ( $Fr$ ), Reynolds ( $Re$ ) and  $KC$  numbers [48]. These number are used to represent wave motion regimes depending on the dominant effects. Froude number similitude is mostly used to organize tank testing campaigns in offshore structures since loads are inertia driven. Reynolds number similitude is usually used when loads are dominated by viscous forces, which occurs in very specific and sometimes localized conditions.

- Froude number represents the relation between inertia and gravity water forces, showed in equation 2.3.46. Therefore, it represents the scaling of wave forces, gravity driven, on large volume structures as well as its dynamics.

$$Fr = \frac{v}{\sqrt{gL}} \quad 2.3.46$$

- Reynolds number represents the relation between inertia and viscous water forces, that can be expressed as in equation 2.3.47. Floating structures may be designed according to scale tests carried out following the Froude number and it must be considered the different

time scales between the Reynolds and Froude numbers. In small scale tests viscous forces have a larger influence than the corresponding forces in full -Froude- scale, which is to be accounted for in any design.

$$Re = \frac{\rho v L}{\mu} \quad 2.3.47$$

- Keulegan Carpenter number shows the dimensional relation between the wave amplitude and the main dimension of the structure, represented in equation 2.3.48. It is a very useful number to decide how to model wave and current exerted forces on the structure [48]. For  $KC < 3$ , the inertia force is dominant, linear potential flow theory is still applicable and viscous drag forces can simply be neglected. When  $3 < KC < 15$ , drag forces start being relevant and can be added in a linearized form, still maintaining frequency domain solutions under acceptable accuracy limits. Within the range of  $15 < KC < 45$  the full Morison equation with the corresponding nonlinear drag and inertia terms cannot be avoided. And for  $KC > 45$  the drag force is dominant, and inertia can be neglected.

$$KC = \frac{v_a T}{D} \quad 2.3.48$$

### 2.3.3 *Catenary Mooring Systems*

As with other mechanical systems, catenary lines can be assumed to have a static or a dynamic behavior, depending on the excitation frequency. Mooring lines are mostly excited by the motions of their fairleads, that depend on the motions of the floating structure. Both methods for static and dynamic lines are used for the analysis of offshore structures and are here included as state of the art, that will be subsequently assessed in Chapter 4. The static catenaries are modelled through the catenary equations for elastic lines whilst dynamic catenaries are analyzed through the lumped mass method, both introduced in this section.

### 2.3.3.1 Static Catenary Mooring Lines

A widespread numerical model to represent static mooring systems is based on the catenary equation, i.e. considering lines as static catenaries. It considers both lines axial stiffness and gravity forces. It is a good approximation when dealing with stationary forces and, as recommended by some offshore standards, e.g. [65], within certain depth ranges and with time varying environmental loads, especially in the low frequency range as suggested by [66]. In real working conditions, motions of any floating structure will be dynamically affected by the first order wave loads and slowly varying wave drift loads, exciting line dynamics of the mooring system. Those scenarios cannot be avoided in any detailed design. However, in preliminary design stages fast computations are valuable so that multiple options are considered, and sensitivity analyses can be performed.

The catenary equation is derived, for a single elastic line, as described in [56], resulting in:

$$h = \frac{T_h}{w} \cdot \left( \cosh \left( \frac{w}{T_h} \cdot \left( x - \frac{T_h}{AE} \cdot l_s \right) \right) - 1 \right) + \frac{1}{2} \cdot \frac{w}{AE} \cdot l_s^2 \quad 2.3.49$$

$$l_s = \frac{T_h}{w} \cdot \sinh \left( \frac{w}{T_h} \cdot \left( x - \frac{T_h}{AE} \cdot l_s \right) \right) \quad 2.3.50$$

To account for the portion of the line laying on the seabed it is to be fulfilled the expression:

$$X = (l - l_s) \cdot \left( 1 + \frac{T_h}{AE} \right) + x \quad 2.3.51$$

Where:

- $T_h$ : Horizontal component of line tension
- $x$ : horizontal coordinate of fairlead with respect to the contact point of line with the seabed. It accounts for the floater position ( $\delta_1, \delta_2$  and  $\delta_3$ ) and the fairleads on the structure
- $h$ : water depth

- $A$ : cross-sectional area of line
- $E$ : Young's modulus of elasticity of lines' material
- $w$ : submerged line weight per unit length
- $X$ : Horizontal distance from anchor point to the fairlead
- $l_s$ : suspended line length

Once the tension of each line is computed, the force of the whole mooring system on the floating structure is defined in equations 2.3.52 for each  $DOF$  of the structure.

$$F_1^m = \sum_{i=1}^n T_{hi} \cdot \cos\psi_i$$

$$F_2^m = \sum_{i=1}^n T_{hi} \cdot \sin\psi_i$$

$$F_3^m = \sum_{i=1}^n l_{si} \cdot w_i$$

2.3.52

$$F_4^m = \sum_{i=1}^n y_{fairi} \cdot (-F_{yi} \cdot \sin\delta_4 + F_{zi} \cdot \cos\delta_4)$$

$$F_5^m = \sum_{i=1}^n x_{fairi} \cdot (-F_{xi} \cdot \sin\delta_5 - F_{zi} \cdot \cos\delta_5)$$

$$F_6^m = \sum_{i=1}^n T_{hi} \cdot (x_{fairi} \cdot \sin\psi_i - y_{fairi} \cdot \cos\psi_i)$$

Where the angles  $\psi_i$  are the angles of each line  $i$  in the horizontal plane  $XY$  as specified in Figure 20, while  $\delta_4$  and  $\delta_5$  are roll and pitch angles respectively of the moored structure.

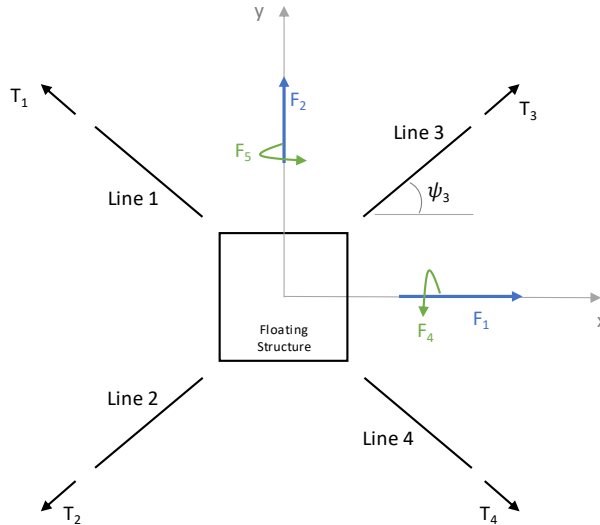


Figure 20 Schematic of a top view of a floating structure with four mooring lines. Lines, lines tensions and forces in the plane of the surface water level have been pointed out.

### 2.3.3.2 Dynamic Catenary mooring lines

To account for mooring lines', drag and inertia loads all lines must be discretized and modelled as series of finite elements. One alternative is to use lumped masses, simplifying mass and stiffness matrix computations. These models, solved in the time domain, represent accurately lines' motions and tensions and are very appropriate for detailed stages when considering deployments in real environments. Several studies have been carried out to assess the accuracy of the lumped mass method coupled to a floating WEC, such as [5], [17], [67] as detailed in section 1.2, in addition, a review of the main findings in that field is summarized in [68]. Also, lumped mass models coupled to a floating structure, both analyzed with *CFD* codes, is introduced in [69] obtaining excellent results.

The lumped mass method assumes mooring lines as interconnected point masses through massless stiffness and dampers representing lines' structural properties and the hydrodynamic loads modelled with the Morison equation 2.3.45. The reference coordinate system for all



bodies, both the moored structure and all lumped masses to be integrated in time is the global origin  $G (0,0,0)$ , as represented in Figure 21. Each point mass representing the mooring system consists of 3 degrees of freedom, all translational in each of the global directions X, Y and Z. The mechanical system defined by each mooring line can be summarized as in equation 2.3.53, this approach is available in several commercial software packages such as Orcaflex [13] or Sesam [11] and was initially introduced by [1].

$$[M] \cdot \{\ddot{\delta}(t)\} = \{F(t)\} = \{F_n(t) + F_z(t) + F_f(t) + F_g + F_b + F_{hyd}(t)\} \quad 2.3.53$$

Where:

- $F_n(t)$ : Structural stiffness and damping force in node n
- $F_z(t)$ : Seabed vertical reaction force
- $F_f(t)$ : Seabed horizontal friction force
- $F_g$ : Gravity force
- $F_b$ : Buoyancy force
- $F_{hyd}(t)$ : Hydrodynamic Morison force

The massless springs and dampers, connecting the lumped masses, represent axial structural properties of lines. Stiffness and damping forces on each node are represented by forces of the adjacent sections as:

$$F_n = F_n^{n+1} - F_n^{n-1} \quad 2.3.54$$

Where:

$$F_n^{n+1} = \frac{E \cdot A}{L_{0n}^{n+1}} \cdot \frac{1}{L_n^{n+1}} \cdot \begin{bmatrix} I_3 & -I_3 \\ -I_3 & I_3 \end{bmatrix} \cdot \begin{Bmatrix} \delta_n \\ \delta_{n+1} \end{Bmatrix} + [C_{Gn}^{n+1}] \cdot \begin{Bmatrix} \dot{\delta}_n \\ \dot{\delta}_{n+1} \end{Bmatrix} \quad 2.3.55$$

$$C_{G n}^{n+1} = \begin{bmatrix} [R]_n^{n+1} & 0 \\ 0 & -[R]_n^{n+1} \end{bmatrix} \begin{bmatrix} [C_L]_n^{n+1} & 0 \\ 0 & -[C_L]_n^{n+1} \end{bmatrix} \cdot \begin{bmatrix} [R]_n^{t n+1} & 0 \\ 0 & -[R]_n^{t n+1} \end{bmatrix} \quad 2.3.56$$

$$[C_L]_n^{n+1} = \begin{bmatrix} \beta \cdot \frac{E \cdot A}{L_{0 n}^{n+1}} & 0 & 0 \\ 0 & 0 & 0 \\ 0 & 0 & 0 \end{bmatrix} \quad 2.3.57$$

Where:

- subscript: node  $n$  in which force  $F$  is applied
- superscript: node to which the force  $F$  connects sub-index node
- $C$ : Damping matrix
- $R$ : Rotation matrix from local to global coordinates
- $E$ : Young elasticity modulus of line material
- $A$ : Cross sectional area of the line
- $\beta$ : Rayleigh coefficient for structural damping estimation
- $L$ : Deformed section length
- $L_0$ : Undeformed section length
- $I_3$ : Identity matrix of dimension 3

Stiffness and damping matrices account for axial forces and therefore a coordinate system rotation is to be done. Whilst the way the stiffness matrix is defined rotations are not necessary, damping matrix and Morison forces do require to compute rotations to obtain correct updates of such forces along the integration time steps. To avoid angle determination with sine and cosine computations, use of quaternions has been made, as explained in [70] where the quaternion is defined as:

$$[Q]^i = \begin{bmatrix} \cos \frac{\theta}{2} & a_x \cdot \sin \frac{\theta}{2} & a_y \cdot \sin \frac{\theta}{2} & a_z \cdot \sin \frac{\theta}{2} \end{bmatrix} \quad 2.3.58$$

Where:

- $\theta$ : Angle of rotation between initial and final position
- $a$ : Vector defining the rotation axis

The vector defining the rotation between local and global vectors is a perpendicular vector to the plane defined by the local ( $x_{1L}$ ) and global ( $\delta_{n+1} - \delta_n$ ) vectors. The local coordinate system is supposed to be located with the x coordinate aligned with the axis connecting both nodes and positive from the seabed to the structure, as represented in Figure 20.

Internal forces are computed for every section of all lines as showed in equations 2.3.54 to 2.3.57. Having defined lines through their three translational *DOFs* the mass matrix is diagonal, whose values account for adjacent half-length masses. The boundary conditions of the mooring lines are defined by the kinematic relations, as represented in equations 3.4.2 and 3.4.3.

Through the axial properties of the material, lines geometry and the rotation matrix, the modeled system can be summarized as in Figure 21.

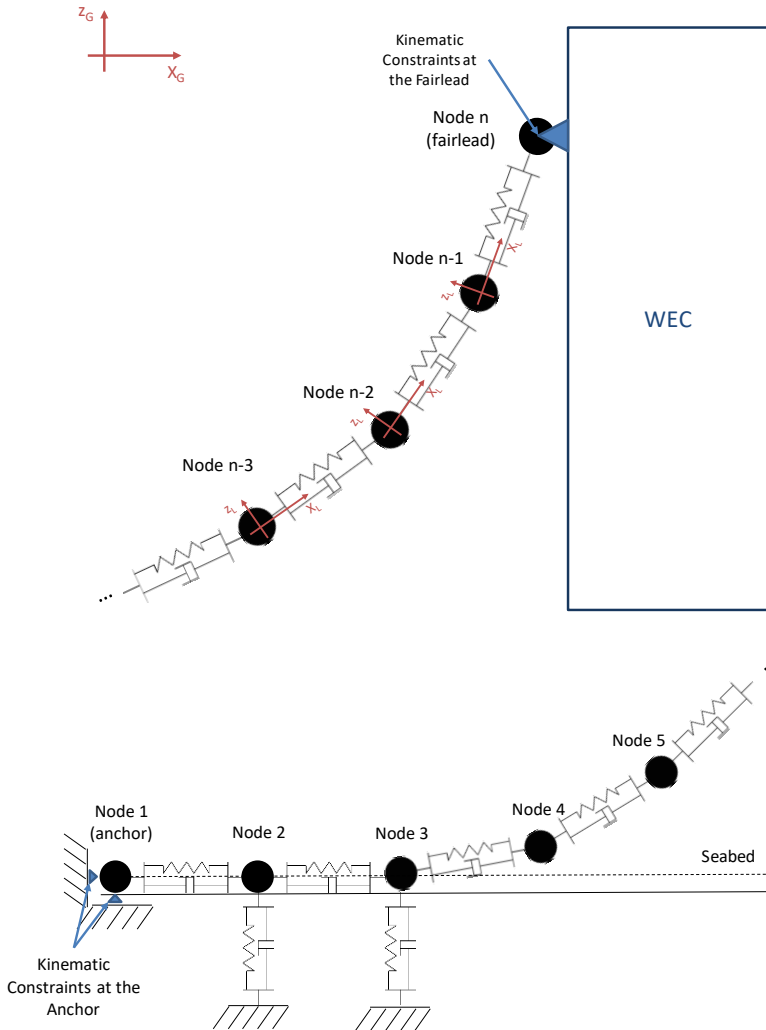


Figure 21 Mooring line schematic representation. Last four nodes and the fairlead with local and global coordinates (top) and first five nodes and the anchor (bottom). The kinematic constraints to maintain the anchor and fairleads are represented with blue triangles

Vertical seabed forces are computed as vertical stiffness and damping forces on the nodes at the seabed. Depending on seabed stiffness, nodes static position will be found slightly deeper in the seabed.

Vertical force is defined as a 1 *DOF* system in which the critical damping and natural frequency are settings of the numerical model as represented by equation 2.3.59.

$$F_z(t) = m_n \cdot \left( \ddot{\delta}_z(t) + 2\xi_v \omega_v \dot{\delta}_z(t) + \omega_v^2 \delta_z(t) \right) \quad 2.3.59$$

Where:

- $\omega_v$ : Vertical natural frequency of seabed nodes
- $\xi_v$ : vertical critical damping of seabed nodes
- $\delta_z$ : Vertical motion of each node on the seabed
- $m_n$ : Nodal mass of the  $n^{\text{th}}$  node

Seabed friction model is implemented through a comparison of horizontal force on the  $n^{\text{th}}$  node and the corresponding friction force. The force is applied through a damping coefficient, linear up to the total friction force, and kept constant for large velocities, as represented in Figure 22.

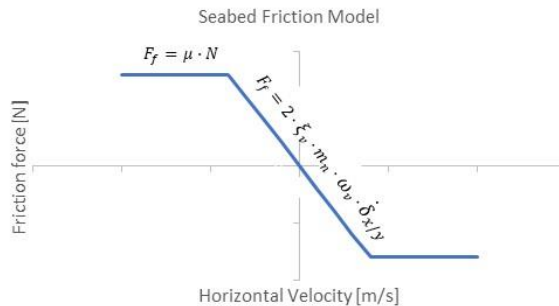


Figure 22 Friction force model

External forces applied on mooring line sections are gravity ( $F_g$ ), buoyancy ( $F_b$ ) and hydrodynamic ( $F_{\text{hyd}}$ ) loads. Gravity force is a constant vertical force due to the gravity acceleration over the length assigned to each node.

$$\{F_g\}^n = \begin{Bmatrix} 0 \\ 0 \\ -m \cdot g \end{Bmatrix} \quad 2.3.60$$

Buoyancy force is considered as opposed to the gravity force due to the weight of the water volume displaced ( $V$ ) by the corresponding line length ( $L_n$ ) assigned to each point mass, where  $\rho_w$  is the water density:

$$\{F_b\}^n = \begin{Bmatrix} 0 \\ 0 \\ V \cdot \rho_w \cdot g \end{Bmatrix} \quad 2.3.61$$

Hydrodynamic forces on line sections have been accounted for through the Morison equation [71], introduced in section 2.3.2.2 and defined in equation 2.3.45 for slender bodies submerged in water. A Morison hydrodynamic force is considered in each degree of freedom of each mass of the mooring lines, considering its velocities and accelerations.

However, the velocities required in equation 2.3.2.2 are referred to the local coordinate system, in the radial and axial directions. Therefore, fluid velocities at node positions are to be rotated to local coordinates so that the hydrodynamic force can be computed and rotated back into global coordinates. For the computation of such fluid velocities, transfer functions have been computed for each degree of freedom at each node position, assuming the deep waters. It allows water particle dynamics to be referred to wave elevation at the global coordinate origin.

The added mass term in equation 2.3.2.2 computed as two independent forces, an excitation force and a linear mass matrix as represented by the first two terms of the right-hand side of equation 2.3.2.2 Unlike the mass term, the drag term is inherently nonlinear and needs to be computed as an independent external force every time step. In practical terms, updating water particle dynamics every time step can be too time consuming and a sensible time period, of e.g. a few seconds, can be used to update the water particle velocities in section 2.3.2.2 without significant changes in the results.

### 2.3.4 Kinematic Relations

In this section the application of kinematic restrictions methods [72] to floating structures are discussed. Initially, the computation of the relations is introduced so that it can be solved either in the time domain or in the frequency domain. It is applicable to either relations between *DOFs* of several floating structures, e.g. a *WEC*, or to any attachment of a mooring line to its corresponding fairlead and anchor, on the moored structure and the seabed respectively. On the one hand it allows the numerical models of the floating structure and the mooring to be solved fully coupled, avoiding intermediate iterations between models. On the other hand, it is not required to know the generalized modes of specific floating *WECs* in advance to obtain the hydrodynamic coefficients. The radiation and diffraction problems can be solved with the floating structures of the *WEC* without any relation and, then, add the kinematic relations in the mechanical system to be solved.

A widespread approach to set kinematic restrictions are the Lagrange equations, which are derived on the equation 2.3.62 for independent coordinates problem:

$$\left\{ \frac{d}{dt} \left( \frac{\partial T(t)}{\partial \dot{\epsilon}(t)} \right) \right\} - \left\{ \frac{\partial T(t)}{\partial \epsilon(t)} \right\} = \{Q(t)\} \quad 2.3.62$$

Where  $\epsilon$  are the independent coordinates of the mechanical system,  $T$  is the kinetic energy and  $Q$  are the generalized forces on those independent coordinates.

Expressing kinematics as function of the independent coordinates and calculating the generalized forces is not straight forward. Therefore, it is customary to approach the problem through dependent coordinates so that, even though the number of degrees of freedom will be higher, the mechanical system can be easily built with the corresponding kinematic relations.

$$\left\{ \frac{d}{dt} \left( \frac{\partial T(t)}{\partial \dot{\delta}(t)} \right) \right\} - \left\{ \frac{\partial T(t)}{\partial \delta(t)} \right\} + \{\Phi_{\delta}^t \cdot \lambda(t)\} = \{F(t)\} \quad 2.3.63$$

The third term in the left-hand side represents forces to fulfil the imposed restrictions between dependent variables  $\delta$ .

Considering the kinetic energy, the equations of motion become as in 2.3.65.

$$T = \frac{1}{2} \cdot \{\dot{\delta}(t)\}^t \cdot [M] \cdot \{\dot{\delta}(t)\} \quad 2.3.64$$

$$[M] \cdot \{\ddot{\delta}(t)\} + [\Phi_\delta]^t \cdot \{\lambda(t)\} = \{F(t)\} \quad 2.3.65$$

The model above represents  $n$  equations since it is the number of variables. However, the number of unknown variables is  $n+m$  as  $m$  is the number of included restrictions through the *Lagrange Multipliers* ( $\lambda(t)$ ) with the aim of fulfilling the restrictions of the mechanical system. Therefore, these restrictions must be solved and so the second set of equations in 2.3.66.

$$\begin{aligned} [M] \cdot \{\ddot{\delta}(t)\} + [\Phi_\delta]^t \cdot \{\lambda(t)\} &= \{F(t)\} \\ \{\Phi(t)\} &= \{0\} \end{aligned} \quad 2.3.66$$

In 2.3.66 the first set of equations are  $n$  ordinary differential equations (*ODEs*) and the second are  $m$  differential algebraic equations (*DAEs*).

Most solvers available nowadays are for systems of *ODEs* instead of for systems of mixed *ODEs* and *DAEs*. Therefore, there are methods to convert the system in 2.3.66 into just a system of *ODEs*. Some of the methods to carry out this task are the Stabilized Lagrange, R Matrix or Penalty Method [72]. Since the penalty method does not add additional *DOFs* to the system, in the present thesis the penalty method has been implemented. It has been used to set restrictions between floating bodies as well as fairlead and anchor points of dynamic mooring lines.

The Lagrange multipliers, represented by  $\lambda$ , represent the forces between degrees of freedom of the system to maintain the imposed restrictions. This method allows the system of equations in 2.3.66 to be directly transformed into a system of *ODEs* without the algebraic equations. The penalty method consists in setting the magnitude of



these forces proportional to the violation of the imposed restrictions. In equation 2.3.67  $\alpha$  is the penalty coefficient which is usually necessary to be adjusted. Other parameters in equation 2.3.67 take usually values of  $\xi = 1$  and  $\omega = 10$ , and these vales have been used in this thesis. This represents a very rigid and fast decaying connection with a large inertia between *DOFs* of the system. However, too high values of the penalizer should be avoided not to generate bad conditioned systems of equations. Introducing the restriction equation into the equation of motion, equation 2.3.68 is derived.

$$\{\lambda(t)\} = \alpha \cdot (\{\dot{\Phi}(t)\} + 2\xi\omega\{\dot{\Phi}(t)\} + \omega^2\{\Phi(t)\}) \quad 2.3.67$$

$$[M] \cdot \{\ddot{\delta}(t)\} + [\Phi_\delta]^t \cdot \alpha \cdot (\{\dot{\Phi}(t)\} + 2\xi\omega\{\dot{\Phi}(t)\} + \omega^2\{\Phi(t)\}) = \{F(t)\} \quad 2.3.68$$

Where the vector  $\{\Phi(t)\}$  represents restrictions between dependent variables, and  $[\Phi_\delta]$  is the derivative of  $\{\Phi(t)\}$  with respect to dependent variables, represented in equation 2.3.69 along with the time derivatives of the restrictions, all to be used in the equation of motion.

$$[\Phi_\delta] = \begin{bmatrix} \frac{\partial \Phi(t)_{11}}{\partial \delta_1(t)} & \cdots & \frac{\partial \Phi(t)_{1n}}{\partial \delta_n(t)} \\ \vdots & \ddots & \vdots \\ \frac{\partial \Phi(t)_{m1}}{\partial \delta_1(t)} & \cdots & \frac{\partial \Phi(t)_{mn}}{\partial \delta_n(t)} \end{bmatrix} \quad 2.3.69$$

$$\{\dot{\Phi}(t)\} = \left\{ \frac{\partial \Phi(t)}{\partial \delta} \cdot \dot{\delta}(t) \right\} = [\Phi_\delta] \cdot \{\dot{\delta}(t)\}$$

$$\{\ddot{\Phi}(t)\} = [\dot{\Phi}_\delta] \cdot \{\dot{\delta}(t)\} + [\Phi_\delta] \cdot \{\ddot{\delta}(t)\}$$

The definitive mechanical system to be solved with dependent coordinates and the corresponding restrictions applying the penalty method is then as represented in equation 2.3.70. It will be used in sections 3.4 and 3.5 to solve wave interacting -multiple- bodies making up a mechanical system (a *WEC* composed of two diffracting bodies) as well as the fairleads and anchor restrictions of the mooring lines.

$$\begin{aligned}
 &([M] + \alpha \cdot [\Phi_\delta]^t \cdot [\Phi_\delta]) \cdot \{\ddot{\delta}(t)\} + \alpha \cdot [\Phi_\delta]^t \\
 &\quad \cdot ([\dot{\Phi}_\delta] \cdot \{\dot{\delta}(t)\} + 2\xi\omega[\Phi_\delta] \cdot \{\dot{\delta}(t)\} + \omega^2\{\Phi(t)\}) = \{F(t)\}
 \end{aligned}
 \tag{2.3.70}$$

This method can be reduced to a set of mass, damping and stiffness matrices in cases with linear restrictions, enabling the resolution of the mechanical system both in time and frequency domains.

## 2.4 Chapter Summary

It has been referenced the untapped potential for Wave Power Conversion worldwide, estimated of the same order of the world power consumption.

The current state of technology development denotes that a variety of device types are being considered. In addition, a large effort in R&D and engineering projects is being carried out, having several full-scale deployments carried out so far.

The linear potential flow method along with the Morison equation have been identified as a suitable and widely used numerical modelling techniques for dynamics of floating structures.

The catenary equations and the lumped mass method are introduced and described as the most suitable means to describe static and dynamic catenary mooring systems respectively.

Numerical methods to set restrictions between degrees of freedom of mechanical systems, widely used in analysis of mechanisms, have been described. Its main purpose in this thesis has been to couple floating body dynamics as well as dynamic mooring lines ends on the seabed and the floater.

UNIBERTSITATEA



Universidad  
del País Vasco

Euskal Herriko  
Unibertsitatea

## Chapter 3

# Development of Numerical Models for Moored Offshore Floating Energy Systems

### 3.1 Introduction

Numerical models introduced so far in the state-of-the-art chapter consider loads and motions of either the floater or the mooring lines. During the design of any moored floating structure, it is generally recommended, as a first step, to assess the influence of the mooring system on the structure through a single linearized stiffness term and, afterwards, assess mooring line loads imposing the resulting structure motions to a dynamic mooring system. Once suitable designs have been found a fully coupled dynamic analysis is recommended. This process may lead to endless design loops, especially in early stages, when the number of variables is significant and the initial *LCOE* estimates of the whole system is to be reduced as much as possible.

In order to ease the design process at different development stages, all the identified models, based on the methods introduced in section 2.3, have been considered, combining floating structure and mooring models. This chapter introduces the numerical tools developed in this thesis to consider floater and mooring lines coupled. Four numerical tools of increasing complexity have been developed in order to enable a comparison in terms of accuracy of loads and motion estimates.

All the developed tools consider the floater as a dynamic mechanical system, whilst the main difference lies in considering the mooring

system as a static or a dynamic system, proposing several contributions with respect to the identified state of the art.

A methodology to characterize horizontal restoring properties of catenary mooring systems is initially proposed, gathering also lines tension and required lengths. It allows estimating line tensions as well as the required material and seabed footprints with the most simplistic approach. A coupling scheme is also proposed for the most widely used approach, that assumes lines as dynamic non-linear systems and solved in the time domain. It is based on the method introduced in section 2.3.4, which allows both mechanical systems to be solved in a single integrated numerical model. Finally, a fully linearized dynamic coupled model is proposed, that can be solved in the frequency domain. This technique overcomes the long simulations of dynamic moorings in the time domain yet considering mooring lines as dynamic systems. In addition, coupled modal analyses are enabled, providing the designer with invaluable information for the mooring system design.

The last section of the chapter introduces the floating geometries considered in the subsequent chapters of this thesis, a spar type floating *WEC* and a cylindrical buoy. While the *WEC* is used to draw main conclusions of the analysis methods applied to such structures in the thesis, the cylindrical buoy has been used as a validation case study. It has been tank tested as a *CALM* buoy, whose data has been shared by Tecnalía R&I [73] and used as a validation case of the lumped mass coupled with a floating structure numerical tool, introduced in section 3.4.

### 3.2 Quasistatic Linearized Frequency Domain

It consists in modelling mooring lines as a static mechanical system and the structure as a dynamic one, that is solved in the frequency domain (*QSFD*). It is introduced in [65] for traditional offshore structures, provided it is demonstrated that effects from anchor line dynamics are negligible. The catenary properties are computed with a tool developed as per equations 2.3.52. The horizontal restoring force of the mooring system is linearized at the estimated mean position, based on steady

mean forces. The obtained horizontal stiffness is included in surge/sway motion and the equation of motion 2.3.41, accounting for the mooring horizontal stiffness, is solved in the frequency domain to obtain the response amplitude vector  $\{\hat{\delta}_a(\omega)\}$  subject to the wave force amplitude vector  $\{\hat{F}_w(\omega) \cdot \eta_a(\omega)\}$ , as showed in equation 3.2.1. Since the drag forces are also considered, the system is solved iteratively through either harmonic or statistical linearization. For regular or irregular waves respectively.

$$\begin{aligned} & \left[ -\omega^2[M + A(\omega) + M_{dkin}] + i\omega[B(\omega) + B_d(\hat{\delta}_a(\omega)) + C_{dkin} + C_{pto}] \right. \\ & \left. + [K_h + K_m + K_{dkin}] \right] \cdot \{\hat{\delta}_a(\omega)\} = \{\hat{F}_w(\omega) \cdot \eta_a(\omega)\} \end{aligned} \quad 3.2.1$$

Where:

- $B_d(\hat{\delta}_a(\omega))$ : Linearized drag force
- $[M_{dkin}], [C_{dkin}], [K_{dkin}]$ : Mass, damping and stiffness from imposing kinematic relations between diffracting bodies, applying 2.3.70 with linear restrictions
- $[K_m]$ : Linearized mooring stiffness

Equation 3.2.1 is introduced assuming the modelled floating WEC is made up of several diffracting bodies, as will be presented in section 3.6.1. Therefore, restriction forces arise, as per equation 2.3.70 that, as long as linear relations are set, can be reduced to the set of  $[M_{dkin}], [C_{dkin}]$  and  $[K_{dkin}]$  matrices.

The resulting system is solved separately for wave frequency and low frequency motions. First order *WF* excitation forces are computed with wave amplitudes derived from the spectrum of the corresponding sea state ( $S_\eta(\omega)$ ). However, the low frequency forces (*LF*) are computed through the corresponding force amplitude of the slowly varying wave drift force spectrum, showed in equation 3.2.2, in the frequency domain, as introduced by Pinkster [74].

$$S_{SV}(\mu) = 8 \cdot \int_0^{\infty} S_{\tau}(\omega + \mu) \cdot S_{\tau}(\omega) \cdot |T(\omega + \mu, \omega)|^2 \cdot d\omega \quad 3.2.2$$

Where:

-  $S_{SV}(\mu)$ : Slowly varying wave drift force spectrum

-  $T(\omega, \omega)$ : Drift force quadratic transfer function

The characteristic tension is computed from a combination of *WF* and *LF* horizontal motions, as shown in 3.2.3 and 3.2.4.

$$\delta_{char} = \max(\delta_{sig}^{LF} + \delta_{max}^{WF}; \delta_{max}^{LF} + \delta_{sig}^{WF}) \quad 3.2.3$$

$$\delta_{sig} = 2 \cdot \sigma_x \quad \text{and} \quad \delta_{max} = \sigma_x \cdot \sqrt{2 \cdot \ln(N)}$$

$$T_{d,QSFD} = T(\delta_{mean} + \delta_{char}) \quad 3.2.4$$

In 3.2.3  $\sigma_x$  is the standard deviation in surge,  $N$  the number of oscillations during the duration of the environmental state and  $T_{d,QSFD}$  the design tension with the *QSFD* approach. The corresponding line tension is provided by the catenary equations for the mooring system at the characteristic offset ( $\delta_{char}$ ) added to the mean offset.

In order to ease the computation of the static properties of the mooring system on the floating structure, each mooring configuration, namely number of lines and radial distribution, can be characterized in advance, independently of the floating structure.

Several authors have already introduced a non-dimensional pretension to characterize catenary mooring systems such as [56] [75]. Here a non-dimensional pretension of each line is defined as the ratio of the mooring line tension and its suspended weight in water,  $a_0 = \frac{T_0}{l_s \cdot w}$ .  $T_0$  is the line pretension, a parameter describing the tensional state of the mooring line in calm water,  $l_s$  is the corresponding suspended line length and  $w$  is the line weight per unit length. It is a measure of how taut a line is and, together with the relative stiffness, it can be considered also as a geometric factor. Looking at the elastic catenary equations, if

equation 2.3.49 is divided by  $l_s$  and rearranging equations 2.3.49 and 2.3.50, equations 3.2.5 and 3.2.6 are obtained.

$$\frac{l_s \cdot w}{T_h} = \sinh\left(\frac{w}{T_h}x - \frac{w \cdot l_s}{AE}\right) = \sinh(k_1) \quad 3.2.5$$

$$\frac{l_s \cdot w}{T_h} \cdot \left(\frac{h}{l_s} - \frac{1}{2} \cdot \frac{w \cdot l_s}{AE}\right) + 1 = \cosh\left(\frac{w}{T_h}x - \frac{w \cdot l_s}{AE}\right) = \cosh(k_1) \quad 3.2.6$$

It can be observed from equation 3.2.5 that, as long as the left-hand side is kept constant, then the constant  $k_1$  will be kept as well. In equation 3.2.6 if the left-hand side is maintained, the constant  $k_1$  will be kept constant again. Therefore, any catenary line will be equivalent as long as the following relations, in left hand side of both equations 3.2.5 and 03.2.6, are constant:

- Non-dimensional horizontal component of line tension:  $\frac{T_h}{l_s \cdot w}$
- Relative axial stiffness:  $\frac{w \cdot l_s}{AE}$
- Scope of suspended length:  $\frac{l_s}{h}$

In this thesis circular line sections have been considered, therefore a change in the line weight per unit longitude entails an equivalent change in the line elasticity. Consequently, the relative stiffness is kept itself as the material is assumed to be homogeneous along the line.

The same procedure is applied for the whole mooring system restoring force and line tension, referring it to the properties of the most loaded line (*MLL*). The mooring system static performance is characterized by the non-dimensional pretension of the most loaded line for a non-displaced structure.

$$a_0 = \frac{T_0^{ml}}{w \cdot l_{s_0}^{ml}} \quad 3.2.7$$



Its restoring force, at different offsets in a defined direction, is represented by the non-dimensional horizontal force of the whole mooring system:

$$a = \frac{F_h^m}{w \cdot l_s^{mll}} \quad 3.2.8$$

The information of the most loaded line can be summarized through the non-dimensional tension and the suspended scope for the same offsets considered for the restoring force:

$$a_{mll} = \frac{T^{mll}}{w \cdot l_s^{mll}} \quad 3.2.9$$

$$s_{mll} = \frac{l_s^{mll}}{h} \quad 3.2.10$$

It can be assumed that all lines within the mooring system are equal to the *MLL*, which can be a good enough approximation for preliminary assessments of mooring system performance and related cost. Therefore, with the system pretension, defined through  $a_0$ , and its horizontal restoring force, line tensions and scope ( $a$ ,  $a_{mll}$  and  $s_{mll}$ ) a configuration is characterized for an axial stiffness and a direction at any water depth with any lines mass. The limitation in characterizing a mooring configuration in such a way lies in the fairleads when changing the water depth, which are horizontally scaled with it. It may not accurately represent the mooring static performance at water depths too large or small compared with that used to compute the reference data.

### 3.3 Quasistatic Non-Linear Time Domain

Solving the *Cummins equation 2.3.33*, accounting for all *DOFs* in the 3 dimensional space, coupled with the catenary mooring force  $\{F_m(t)\}$  is proposed in [66], and has been assessed in many works, such as [2], [4]. It still assumes the mooring system as a static mechanical system and the floating structure as a dynamic one, that is solved in the time domain

(*QSTD*). However, the static (non-linear) properties can be included not only in surge but also in all other degrees of freedom. In addition, since the proposed model is solved in the time domain, a nonlinear viscous drag force vector  $\{F_d(t)\}$  in all degrees of freedom has been included in equation 3.3.1, as showed in the last term of the RHS of 2.3.45. The convolution term for the radiation damping has been solved through direct numerical integration as it is a system with at least six *DOFs* and, therefore, 36 convolution terms. This model is advantageous since it considers the quadratic drag force as well as non-linear geometric stiffness of the catenary lines of the mooring system and the influence of all degrees of freedom on mooring lines. However, it requires the catenary equations, as defined in 2.3.52 to be solved at every time step with its implicit iterative loop.

$$[M + A_\infty + M_{akin}] \cdot \{\ddot{\delta}(t)\} + \left\{ \int_{-\infty}^t B(t - \tau) \cdot \dot{\delta}(\tau) \cdot d\tau \right\} + [C_{akin} + C_{pto}] \cdot \{\dot{\delta}(t)\} \quad 3.3.1$$

$$+ [K_{akin} + K_h] \cdot \{\delta(t)\} = \{F_w(t)\} + \{F_m(t)\} + \{F_d(t)\}$$

The term  $\{F_d(t)\}$  represents the viscous drag force on the structure, modelled for each degree of freedom as in equation 3.3.2.

$$F_{di}(t) = -C_i \cdot |\dot{\delta}_i(t)| \cdot \dot{\delta}_i(t) \quad 3.3.2$$

Where  $i$  denotes the degree of freedom and  $C_i$  the corresponding drag force factor, which mainly depends on the structure geometry.

In this approach the mooring system has been represented by the elastic catenary equations with zero touch-down angle. To represent all statistical properties of the *LF* motions at least 3 hour 5 simulations are suggested in [66]. The maximum line tension of each simulation  $T_k$  is processed as represented with equations 3.3.3 and 3.3.4, where  $n$  refers to the number of simulations and  $T_{dQSTD}$  is the design tension with this approach.

$$T_{\mu} = \frac{1}{n} \sum_{k=1}^n T_k \quad ; \quad T_{\sigma} = \sqrt{\frac{1}{n} \sum_{k=1}^n (T_k - T_{\mu})^2} \quad 3.3.3$$

$$T_{d_{QSTD}} = T_{\mu} + 2 \cdot T_{\sigma} \quad 3.3.4$$

Where:

- $T_{\mu}$ : Mean line tension
- $T_{\sigma}$ : Standard deviation of line tension maxima of the set of simulations

### 3.4 Dynamic Non-Linear Time Domain

In addition to the non-linear geometric stiffness of catenary lines, the most widely used approach to account for drag and inertia forces on lines is the *FEM* or lumped mass model coupled with the wave structure interaction model, a completely dynamic model solved in the time domain (*DynTD*). In this section a *DynTD* model has been built, in which the wave structure interaction model is based on the linear potential flow complemented with a Morison force term and dynamic moorings based on the lumped mass model. Both models are fully coupled through the use of kinematic relations as introduced in section 2.3.4 so that kinematic restrictions are imposed on all fairleads and anchors of each mooring line. Even though this model is the most widely used due to its accuracy and availability in commercial codes, it can be too time consuming for sensitivity analyses of designs with several parameters.

The resulting hydrodynamic and mooring coupled model can be summarized through a set of mass, damping and stiffness matrices together with a force vector as in equation 3.4.1:

$$\begin{aligned}
 & \begin{bmatrix} (M + A)_{str} + M_{dkin} & M_{f/a} \\ M_{f/a} & M_{moor} \end{bmatrix} \cdot \begin{Bmatrix} \ddot{\delta}_{str}(t) \\ \ddot{\delta}_{moor}(t) \end{Bmatrix} + \begin{bmatrix} C_{pto} + C_{dkin} & C_{f/a} \\ C_{f/a} & C_{moor} \end{bmatrix} \\
 & \cdot \begin{Bmatrix} \dot{\delta}_{str}(t) \\ \dot{\delta}_{moor}(t) \end{Bmatrix} + \begin{bmatrix} H_{str} + K_{pto} + K_{dkin} & K_{f/a} \\ K_{f/a} & K_{moor} \end{bmatrix} \cdot \begin{Bmatrix} \delta_{str}(t) \\ \delta_{moor}(t) \end{Bmatrix} \quad 3.4.1 \\
 & = \begin{Bmatrix} F_{fk}(t) + F^{sv}(t) + F_d(t) - F_{conv}(t) - F_{f/a}(t) \\ F_z(t) + F_f(t) + F_g + F_b + F_{morison}(t) + F_{f/a}(t) \end{Bmatrix}
 \end{aligned}$$

In the equation 3.4.1 subscripts *str* denotes structure, *moor* denotes mooring, *pto* denotes power take off and *dkin* and *f/a* denotes kinematic relations between diffracting bodies and fairleads/anchors respectively. In the force vector referred to the structure, a quadratic viscous drag term ( $F_d(t)$ ) has been added, modelled as in equation 3.3.2. Due to the differences in natural frequencies of the floating structure and lines' elements, equation 3.4.1 represents a stiff system and the implicit Newmark integration scheme has been chosen to carry out the integration [49].

It should be noted that the force  $F_{f/a}$  stands for the forces to maintain fairleads at a constant distance from the centre of gravity of the structure and anchors fixed in the corresponding seabed positions. Its magnitude depends on the positions of the fairlead and anchor points with respect to the centre of gravity of the floater at each time step,  $\delta_{x,y,z-fair}$  and  $\delta_{x,y,z-anchor}$  respectively in equation 3.4.2. Whilst  $\delta_{x,y,z-fair}$  is time invariant,  $\delta_{x,y,z-anchor}$  changes along the time as the floater moves, and the corresponding force, built up as a constant force in 3.4.4 with the restrictions set in 3.4.2, needs to be updated every time step. Fairleads and anchors force,  $F_{f/a}$ , on the structure corresponds to the forces of all lines attached to the structure and with opposite sign with respect to the  $F_{f/a}$  on the corresponding attachment nodes on mooring lines.

The dynamic system described above is composed of three main parts, the floater, mooring lines and the lines fairleads and anchor. All of them have been included in the numerical model either through stiffness, damping and mass matrices or as time varying forces. Floater dynamics is linear since its wave structure interaction have been computed with a linear potential code and, hence, its matrices are time invariant as well

as the *PTO* forces, that have been modelled as a set of linear stiffness and damping matrices.

On the other hand, kinematics of fairlead and anchor points have been defined by means of multibody restrictions, as introduced in section 2.3.4. Such restrictions consist in setting kinematic relations between the three *DOFs* of the fairlead and anchor points with the floating structure and on the seabed respectively. These restrictions are expressed in equations 3.4.2 and 3.4.3 following the notation suggested in 2.3.69.

- Fairlead restrictions (dynamics of the fairlead of the structure imposed to the mass point  $n$ )

$$\Phi = \begin{cases} x_{surge} + x_{roll} + x_{yaw} + \delta_{x-fair} - x_n \\ y_{sway} + y_{pitch} + y_{yaw} + \delta_{y-fair} - y_n \\ z_{yaw} + z_{roll} + z_{pitch} + \delta_{z-fair} - z_n \end{cases} \quad 3.4.2$$

- Anchor (the mass point  $1$  of the line must be kept constant at its predefined point):

$$\Phi = \begin{cases} \delta_{x-anchor} - x_1 \\ \delta_{y-anchor} - y_1 \\ \delta_{z-anchor} - z_1 \end{cases} \quad 3.4.3$$

In equation 3.4.2  $\delta_{x,y,z,-fair}$  denote the position of the fairlead with respect to the *COG* of the structure as well as  $x_{surge,roll,yaw}$ ,  $y_{sway,pitch,yaw}$  and  $z_{heave,roll,pitch}$  denote the motions of the fairleads in the global X, Y and Z axis due to the corresponding motions of the structure. The anchor points are to be kept fixed on the seabed and to do so the position with respect to the *COG* of the structure  $\delta_{x,y,z-anchor}$  are to be updated along the time.

The relations presented above have constant derivatives which make them linear and can, therefore, be reduced to a set of stiffness, mass and damping matrices, representing the attachment forces plus a set of constant vectors arising from the constant distances  $\delta_{fair}$  and  $\delta_{anchor}$ . Such terms are directly derived from equation 3.4.4.

$$\begin{aligned}
 \{F_{f/a}(t)\} &= \alpha_{att} \cdot [\Phi_{\delta}^T(t)] \\
 &\cdot ([\Phi_{\delta}(t)] \cdot \{\delta(t)\} + [\dot{\Phi}_{\delta}(t)] \cdot \{\dot{\delta}(t)\} + 2\xi_{att}\omega_{att}[\Phi_{\delta}(t)] \\
 &\cdot \{\delta(t)\} + \omega_{att}^2\{\Phi(t)\})
 \end{aligned} \quad 3.4.4$$

In case the *WEC* is made up several diffracting rigid bodies, such as the floater and the internal *SWL* defined in the case study in section 3.6.1, the kinematic relations impose the internal *SWL* to rigidly move with the floater in surge and sway, see 3.4.5. Since the internal *SWL* does not have mass nor stiffness in yaw, it has also been set to rigidly move in yaw with the floater to avoid numerical issues. The numbering of the degrees of freedom of the diffracting bodies assumes the *first* body as the anchored body, the structure here (*DOFs* 1 to 6), and the second body, the internal *SWL* (*DOFs* 7 to 12) in equation 3.4.5 as rigidly joined to the first body.

$$\{\Phi_{dkin}(t)\} = \begin{cases} \delta_1(t) - \delta_7(t) \\ \delta_2(t) - \delta_8(t) \\ \delta_6(t) - \delta_{12}(t) \end{cases} \quad 3.4.5$$

Therefore, the formulation used for anchor and fairleads of the mooring system can also be used to set restrictions between floating structures, as it has been done here for the diffracting bodies (the structure and the internal *SWL*), through the restrictions set in 3.4.5. In this case all forces between both bodies are proportional to the body motions and no constant forces have been needed in the time domain model, resulting in a similar equation, showed in 3.4.6.

$$\begin{aligned}
 \{F_{dkin}(t)\} &= \alpha_{dkin} \cdot [\Phi_{dkin}^T \delta] \\
 &\cdot ([\Phi_{dkin} \delta] \cdot \{\delta(t)\} + [[\dot{\Phi}_{dkin} \delta] + 2\xi_{dkin}\omega_{dkin}[\Phi_{dkin} \delta]] \\
 &\cdot \{\delta(t)\} + \omega_{dkin}^2\{\Phi_{dkin}(t)\})
 \end{aligned} \quad 3.4.6$$

The design line tension, when carrying out simulations based on the *DynTD* model, is computed assuming the maxima of the simulations are Gumbel distributed, resulting in the equation 3.4.7. In order to

represent the low frequency variations, it is recommended in [65] to carry out at least 10 3-hour time domain simulations.

$$T_{d\_DynTD} = T_{\mu} - 0.577216 \cdot T_{\sigma} \cdot \frac{\sqrt{6}}{\pi} \quad 3.4.7$$

Where  $T_{\mu}$  and  $T_{\sigma}$  are the mean and the standard deviation of the maximum line tensions of the 10 simulations respectively and  $T_{d\_DynTD}$  the design line tension with this approach.

### 3.5 Dynamic Linearized Frequency Domain

Considering mooring lines as dynamic mechanical systems, coupled to a dynamic floater in a model that can be solved in the frequency domain (*DynFD*), can be found just in a few references, such as in [22] applied in ultra-deep waters. It consists in solving the system 3.4.1 in the *FD*, and in order to do so all forces arising from both the structure, the mooring system and line attachments must be linearized. Main sources of non-linearity in 3.4.1 are the viscous forces on both the floater and mooring nodes, shape changes and the geometric stiffness of catenary lines as well as the fairlead relations between the structure and mooring line ends. These effects are to be linearized in this section in order to enable the *FD* solution of the whole coupled model.

Whilst wave interaction forces of the structure are modelled through linear hydrodynamic coefficients, complemented with a viscous force term, the hydrodynamic loads on mooring lines are added through the Morison force, as shown in equation 2.3.45. On the one hand, the inertial term of the RHS in 2.3.45 is linear and consists of an excitation force, called effective buoyancy term and proportional to water particles acceleration, and the added mass term, proportional to the acceleration of the corresponding *DOF* (either of the floater or of a node of a mooring line). On the other hand, the viscous force term in the RHS of equation 2.3.45 can be rearranged as an excitation force and a damping force, both functions of the relative velocity of the fluid with respect to the corresponding degree of freedom ( $u(t) - \dot{\delta}(t)$ ), as

shown in equations 3.5.1 and 3.5.2. It has been assumed that the current velocity does not contribute on the varying hydrodynamic forces in order to simplify the process, and the linearized coefficient is therefore as introduced in 3.5.2 [48]. It makes the viscous drag force non-linear and iterations are needed to solve the complete *FD* model.

$$F_{drag}(t) = \gamma(u(t) - \dot{\delta}(t)) \cdot u(t) - \gamma(u(t) - \dot{\delta}(t)) \cdot \dot{\delta}(t) \quad 3.5.1$$

$$\gamma(u(t) - \dot{\delta}(t)) = \begin{cases} \frac{8}{3\pi} \cdot f_v \cdot \max(u - \dot{\delta}(t)) \rightarrow \text{Regular waves} \\ \sqrt{\frac{8}{\pi}} \cdot f_v \cdot \sigma_{u-\dot{\delta}(t)} \rightarrow \text{Irregular waves} \end{cases} \quad 3.5.2$$

In equation 3.5.2  $f_v = 0,5 \cdot \rho_w \cdot C_d \cdot D \cdot L$  and  $\sigma_{u-\dot{\delta}(t)}$  represents the standard deviation of the relative fluid velocity with respect to the corresponding *DOF*. Therefore, the linearization of the Morison viscous drag term ends up in a set of two linearized forces, proportional to the fluid and to the corresponding *DOF* velocities respectively. Consequently, the damping matrix and the velocity force depend on all *DOF* motions, implying the *FD* solution to be solved through a fixed-point iterative process. This iterative method consists in setting an initial value of  $\gamma$ , e.g. 0, that will provide an initial solution and an updated  $\gamma$ . The same computation is carried out until either  $\max(u - \dot{\delta}(t))$  or  $\sigma_{u-\dot{\delta}(t)}$ , for regular and irregular waves respectively, show a low error with respect to the previous solution, 0.1% has been assumed low enough in this thesis. Following the same procedure, mass forces in equation 2.3.45, proportional to the acceleration of the fluid and the corresponding *DOF*, are shown in equation 3.5.3. In this case it represents two linear forces that are directly included in the complete *FD* model, shown in equation 3.5.9.

$$F_{inertia}(t) = (1 + C_a) \cdot \rho_w \cdot V \cdot \dot{u}(t) - C_a \cdot \rho_w \cdot V \cdot \ddot{\delta}(t) \quad 3.5.3$$

In contrast with the *DynTD* model, the *DynFD* model provides only the time-varying part of the solution. The structural damping, as already



introduced in 2.3.57, is valid for velocities referred either to the absolute reference centre or to the mean position. However, the stiffness matrix, as in 2.3.55, needs to be redefined to work with the time varying motions, referenced to the mean position. Consequently, it implies adapting the structural stiffness matrix of the mooring system as represented in equation 3.5.4.

$$K_{G_n}^{n+1} = \begin{bmatrix} [R]_n^{n+1} & 0 \\ 0 & -[R]_n^{n+1} \end{bmatrix} \begin{bmatrix} [K_L]_n^{n+1} & 0 \\ 0 & -[K_L]_n^{n+1} \end{bmatrix} \cdot \begin{bmatrix} [R]_n^{t\ n+1} & 0 \\ 0 & -[R]_n^{t\ n+1} \end{bmatrix} \quad 3.5.4$$

$$[K_L]_n^{n+1} = \begin{bmatrix} \frac{E \cdot A}{L_{0n}^{n+1}} & 0 & 0 \\ 0 & 0 & 0 \\ 0 & 0 & 0 \end{bmatrix} \quad 3.5.5$$

In equation 3.5.4  $n$  denotes specific nodes of mooring lines, where subscripts and superscripts denote nodes connecting each line section. The subscript  $L$  indicates local coordinates of each node, with the positive  $X$  direction aligned with a line connecting both nodes, pointing at the node  $n+1$ , as represented in Figure 21. The subscript  $G$  indicates global coordinates to which the whole system is referred, with the  $XY$  plane on the undisturbed  $SWL$  and the positive  $Z$  axis pointing upwards.  $R$  is the rotation matrix relating local and global coordinates for each line section, computed with the floater at the mean position, and  $K_L$  is the structural stiffness matrix of each line section referred to its local coordinates. The local structural stiffness matrix accounts only for axial stiffness, and, following the sign convention adopted for local coordinates, it is represented in the first position of the matrix, as shown in equation 3.5.5. The structural damping has been defined as a Rayleigh damping matrix. Following the same procedure as in equations 3.5.4 and 3.5.5 for the stiffness matrix, the structural damping matrix is straightforward defined as  $[C_G]_n^{n+1} = \beta \cdot [K_G]_n^{n+1}$ , where  $\beta$  is the stiffness proportional Rayleigh damping coefficient.

The non-linear geometric stiffness contributes significantly on the system performance, especially in cases with significant mooring pretensions and in the  $LF$  range. Its influence on the floater has been here computed as the secant stiffness force on the structure. It is computed after each iteration of the  $FD$ , assuming oscillation amplitudes equal to two standard deviations of each degree of freedom of the floater about the mean position, obtaining the floater linearized geometric stiffness matrix,  $[K_g^f]$ . In addition, the same force differences have also been computed on the mooring line nodes, as a consequence of the same structure motion amplitudes, with an analytic subroutine of a catenary mooring system, as described in 2.3.52, obtaining  $[K_g^m]$ . These matrices provide the corresponding geometric stiffness effect on both the floater and lines, as represented in equations 3.5.6 and 3.5.7.

$$[K_g] = \begin{bmatrix} [K_g^f] & [K_g^m]^T \\ [K_g^m] & [0] \end{bmatrix} \quad 3.5.6$$

$$[K_g^f] = \begin{bmatrix} \frac{\Delta F_1}{\Delta x_1} & \dots & \frac{\Delta F_1}{\Delta x_6} \\ \vdots & \ddots & \vdots \\ \frac{\Delta F_6}{\Delta x_1} & \dots & \frac{\Delta F_6}{\Delta x_6} \end{bmatrix} \quad \text{and} \quad [K_g^m] = \begin{bmatrix} \frac{\Delta F_{dof\_f+1}}{\Delta x_1} & \dots & \frac{\Delta F_{dof\_f+1}}{\Delta x_6} \\ \vdots & \ddots & \vdots \\ \frac{\Delta F_{dof\_t}}{\Delta x_1} & \dots & \frac{\Delta F_{dof\_t}}{\Delta x_6} \end{bmatrix} \quad 3.5.7$$

In equations 3.5.6 and 3.5.7  $K_g$  indicates the linearized geometric stiffness matrix based on the mentioned amplitude assumption. The superscripts  $m$  and  $f$  denote mooring and floater and  $DOF\_t$  stands for *total* degrees of freedom of the system. Summarizing, the stiffness matrix is the static mooring force tensor, considering the influence of motions in all degrees of freedom of the floating structure on all degrees of freedom of the coupled model, both the structure itself and mooring lines.

The kinematic relations modeling fairlead and anchor points are defined in the same manner as introduced in section 3.4 by means of Lagrange multipliers, a force vector is added to the system that makes it fulfill the restrictions and avoids adding additional equations. The simulation in the frequency domain requires all forces to be linear either with respect

to the excitation or to the motion of the model. The restrictions in equation 3.4.2 and 3.4.3 are also set here for the frequency domain resolution and can be broken down into two terms, those depending on model motions and constant forces. Constant forces are not included in the frequency domain solution since it is already assumed to be in equilibrium, and consequently  $\delta_{x,y,z\text{-fairlead}}$  and  $\delta_{x,y,z\text{-anchor}}$  are not considered. Expressing  $x_{surge,roll,yaw}$ ,  $y_{sway,pitch,yaw}$  and  $z_{heave,roll,pitch}$  in 3.4.2 linearly with the structure positions, the restriction vector can be considered linear at the mean position as  $\{\Phi(t)\} = [\Phi_c] \cdot \{\delta(t)\}$ , and the equation 3.4.4 becomes:

$$\begin{aligned} \{F_{f/a}(t)\} = & \alpha_{att} \cdot [\Phi_\delta^T] \\ & \cdot \left( [\Phi_\delta] \cdot \{\ddot{\delta}(t)\} + \left[ [\dot{\Phi}_\delta] + 2\xi_{att}\omega_{att}[\Phi_\delta] \right] \cdot \{\dot{\delta}(t)\} \right. \\ & \left. + \omega_{att}^2[\Phi_c] \cdot \{\delta(t)\} \right) \end{aligned} \quad 3.5.8$$

The form in which equation 3.5.8 is expressed denotes a linear system, which can be directly included in a frequency domain model 3.5.9 through a set of mass, damping and stiffness matrices ( $M_{f/a}$ ,  $C_{f/a}$ ,  $K_{f/a}$ ).

The slowly varying second order wave drift forces have been included in the model through the spectrum proposed in [74] and detailed here in equation 3.2.2.

With respect to the seabed vertical reaction, it is modelled in the frequency domain through stiffness and damping matrices on the nodes on the seabed in the equilibrium position. The friction force has been also modelled through a damping matrix, applying the same damping coefficient as in the vertical motions, acting on the horizontal degrees of freedom of the corresponding nodes. These matrices are included in the whole mooring stiffness and damping matrices.

The resulting coupled mechanical model is expressed as in equation 3.5.9.

$$\begin{aligned}
& \left( -\omega^2 \cdot \begin{bmatrix} (M + A(\omega))_{str} + M_{dkin} & M_{f/a} \\ M_{f/a} & M_{moor} + \rho_w \cdot V \end{bmatrix} + i\omega \right. \\
& \cdot \left. \begin{bmatrix} \gamma_{str} (u(t) - \delta(t)) + B(\omega) + C_{pto} + C_{dkin} & C_{f/a} \\ C_{f/a} & C_{moor} + \gamma_{moor} (u(t) - \delta(t)) \end{bmatrix} \right) \\
& + \begin{bmatrix} H_{str} + K_g^f(\delta) + K_{pto} + K_{dkin} & K_g^{mT}(\delta) + K_{f/a} \\ K_g^m(\delta) + K_{f/a} & K_{moor} \end{bmatrix} \cdot \begin{Bmatrix} \hat{\delta}_{str}(\omega) \\ \hat{\delta}_{moor}(\omega) \end{Bmatrix} \\
& = \left\{ \begin{array}{l} \hat{F}_w(\omega) \cdot \hat{\eta}(\omega) + \hat{F}^{sv}(\omega) \\ (-\omega^2(1 + C_a) \cdot \rho_w \cdot V + i\omega \cdot \gamma_{moor} (u(t) - \delta(t))) \cdot \hat{\eta}(\omega) \end{array} \right\}
\end{aligned} \tag{3.5.9}$$

Since equation 3.5.9 contains both damping and stiffness terms dependent on the solution, the whole system is solved iteratively, through the fixed point iteration procedure as detailed above in this section. Therefore, the resulting solution yields constant values of the mentioned solution dependent terms.

Line tensions can therefore be obtained postprocessing motion amplitudes of the corresponding nodes, with the stiffness and damping matrices of mooring line sections, shown in equation 3.5.4 and the corresponding structural damping. It provides tension amplitudes that can be further processed to obtain power spectral densities (*PSDs*) and the corresponding maximum line tensions.

### 3.6 Case Study Geometries of Floating Structures

In this section the geometries of the floating structures used in Chapter 4, Chapter 5 and Chapter 6 of this thesis are described. The main objective is the analysis of the interaction of floating structures with the mooring system, particularly heaving *WECs*, that tend to be small and very dynamic structures. In order to perform most calculations, a previously published geometry has been selected, see [16] and the hydrodynamic properties of the floater are introduced in section 3.6.1. In addition, a lumped mass numerical tool has been developed, that represents the *DynTD* model, that has been subject to a tank test

validation phase. The tank test data for validation has been provided by Tecnalia [73], which consists of a *CALM* buoy. The hydrodynamic properties of the floater are also introduced in section 3.6.2.

### 3.6.1 Spar Type Oscillating Water Column Wave Energy Converter

This geometry is designed to work as an *OWC* in which the power is extracted from the relative heaving motion of the structure represented in Figure 23 with respect to its internal water column. The compressed and expanded air is made to pass through a self-rectifying air turbine allocated on the deck of the floating structure. Its hydrodynamic properties for power production assessment can be modelled, among other methods, with two diffracting bodies. The coupled model consists of the one represented in Figure 23 interacting with a massless surface, representing the free surface water of the internal water column. The floating *WEC* geometry is based on the optimisation presented in [16], model *K*. It has been modelled through linear potential theory and its mesh representation and main dimensions are shown in Figure 23.

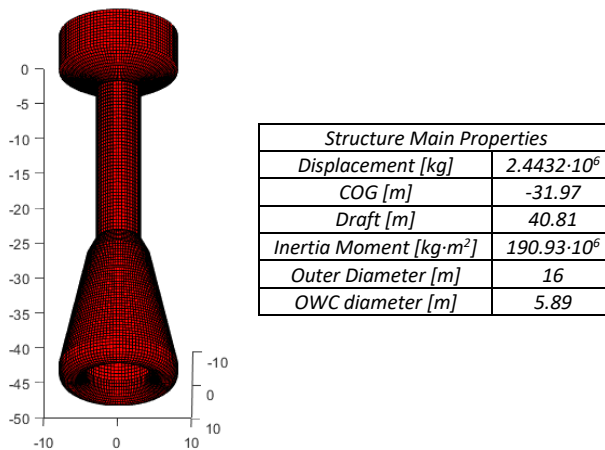


Figure 23 Mesh representation of the *BEM* model for the *WEC* spar platform submerged part (left) and its main physical properties (right). Data adapted from [16], model *K*

Two numerical models of this device have been built up to assess body motions, one for extreme conditions and another one in operational conditions. The model for extreme conditions assumes that the device operates in the survival mode, represented with the structure open at its top part and, therefore, the hydrodynamic model is based on a single body, representing the structure in Figure 23. It is a reasonable assumption as the closed chamber has been proved to induce large motions [17]. The second model represents the device in its power production mode, in order to do such model two diffracting bodies are needed, the structure in Figure 23 and a massless surface at the *SWL* of the internal water column. Therefore, the power production model is composed of 12 *DOFs*, six per diffracting body, and needs the corresponding kinematic restrictions to model the two bodies moving together in the horizontal motions, surge and sway. In addition, the yaw motion of both structures has also been restricted to move with the structure to avoid numerical issues in yaw of the internal *SWL*. Both bodies are left to move freely, with the corresponding hydrodynamic interactions, in heave, pitch and roll. It should be noted that pitch and roll of the internal *SWL* represent sloshing modes which might be better represented by the geometry of the corresponding sloshing modes along with the air compressibility to obtain better estimates of power production. Nevertheless, it has been assumed to be accurate enough for mooring performance assessment as well as device dynamics.

Table 1 Viscous drag force factors considered for each degree of freedom of the structure and the corresponding natural frequencies

<b>Degree of freedom</b>	<b>Viscous Drag Factors <math>f_v</math> [N·s/m] // [N·m·s]</b>	<b>Natural frequencies [rad/s]</b>
<b>Surge</b>	$1.188 \cdot 10^5$	0.064
<b>Sway</b>	$1.188 \cdot 10^5$	0.065
<b>Heave</b>	$4.469 \cdot 10^4$	0.6651
<b>Roll</b>	$3.532 \cdot 10^9$	0.3757
<b>Pitch</b>	$3.532 \cdot 10^9$	0.3757
<b>Yaw</b>	0	-
<b>Heave SWL</b>	0	0.5063
<b>Pitch SWL</b>	0	2.524

The current steady force can be assumed as a constant force, which will be related with a projected surface of  $290[\text{m}^2]$ . The total displaced mass of the structure is  $2.4432 \cdot 10^6[\text{kg}]$  and the *COG* is placed  $31.97[\text{m}]$  below de surface water level, assuming to be similar to the geometry introduced in [17]. The mass moment of inertia in pitch and roll has been assumed to be  $190.93 \cdot 10^6[\text{kg} \cdot \text{m}^2]$  derived from assuming a radius of gyration equal to half the length of the section from the *COG* to the keel,  $8.84[\text{m}]$ .

The numerical model relies on the hydrodynamic coefficients in Figure 24, that have been computed in this thesis with a commercial code based on the linear potential flow theory [62]. In addition, all motions of the structure are influenced by viscous drag forces, the assumed factors are described in Table 1, along with the natural frequencies in each degree of freedom considering the mooring system, computed within the work performed in section Chapter 6.

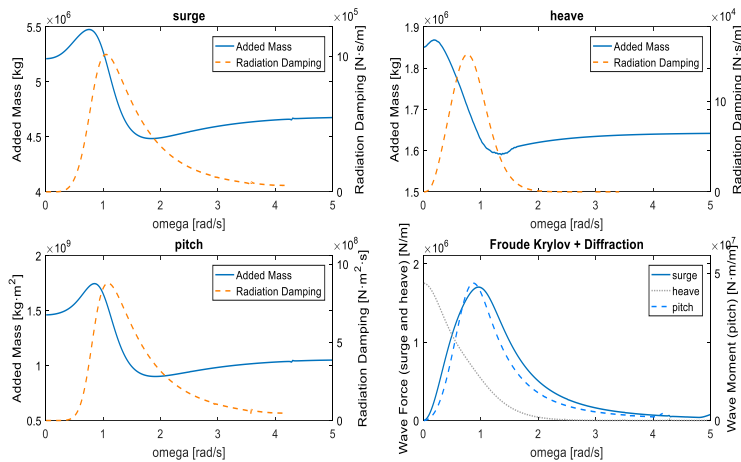


Figure 24 Hydrodynamic coefficients of the floating buoy spar *WEC* in surge, heave and pitch, the cross coupled coefficients have been omitted here, but used in the model. Added mass and Radiation damping of surge (top-left), heave (top-right) and pitch (bottom-left). Froude-Krylov and diffraction forces in surge, heave and pitch (bottom-right)

The non-linear drift force in surge has been accounted for through the Newman approximation and based on the mean drift coefficients computed by the linear potential code.

The *PTO*, in the power production model, has been assumed to be linear and acting on the relative heave motions between the structure and the water surface level, and is usually modelled through a stiffness and damping matrices ( $K_{pto}, C_{pto}$ ), as represented, in the frequency domain, in equation 3.6.1.

$$\begin{Bmatrix} F_{pto} \delta_3^f(\omega) \\ F_{pto} \delta_3^{SWL}(\omega) \end{Bmatrix} = (K_{pto} + i\omega \cdot C_{pto}) \cdot \begin{bmatrix} 1 & -1 \\ -1 & 1 \end{bmatrix} \cdot \begin{Bmatrix} \delta_3^f(\omega) \\ \delta_3^{SWL}(\omega) \end{Bmatrix} \quad 3.6.1$$

The *PTO* in an *OWC* system consists generally of a self-rectifying air turbine, such as the Wells turbine or Impulse turbines as introduced in [76], [77] that introduces a damping term in the relative motion. In addition, the air chamber compressibility adds a non-linear stiffness term in the relative motion.

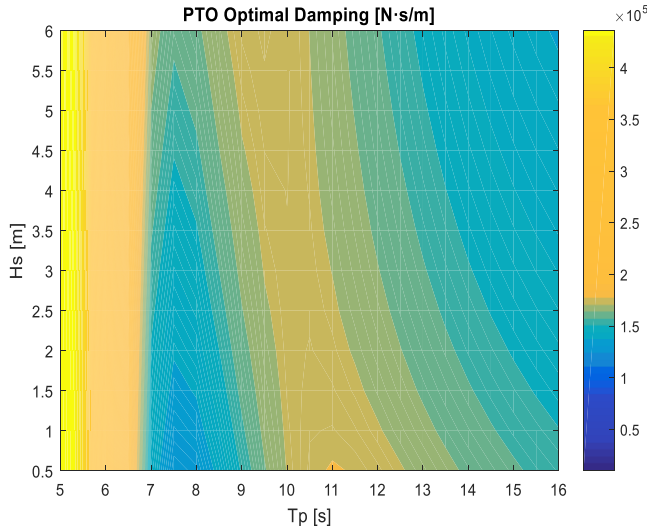


Figure 25 Optimal *PTO* damping per sea state computed with the *OWC* type *WEC*



In this thesis it has been considered just a damping term for simplicity, assuming the chamber not to introduce any stiffness in the system, which can be acceptable for the mooring induced loads but has a non-negligible influence in the produced power [78]. Therefore, the *PTO* has been assumed not to introduce any stiffness in the system and the optimal *PTO* damping has been numerically computed to maximise the extracted energy with a frequency domain model, accounting only for the body motions in heave. A linearized viscous force damping based on the coefficients in Table 1, without the mooring system, has been assumed. The obtained values are represented in Figure 25.

### 3.6.2 *Catenary Anchor Leg Mooring (CALM) Buoy*

This floating structure has been modelled in order to carry out an experimental validation of the *DynTD* model developed in section 3.4. The *CALM* buoy here modelled represents the HarshLab 2.0 platform shape, designed by the consortium made up for its commercial operation as a real sea laboratory for offshore materials. The experimental testing has been carried out at the CEHIPAR wave tank, in Madrid. The floater is made of a single rigid floating structure, consisting of two vertical cylinders. The larger cylinder is partially submerged, and the freeboard is made up of the remaining part of the structure, the smaller cylinder sits on the deck of the larger one. Its main dimensions both in full-scale and in the scaled teste model are shown in Table 2.

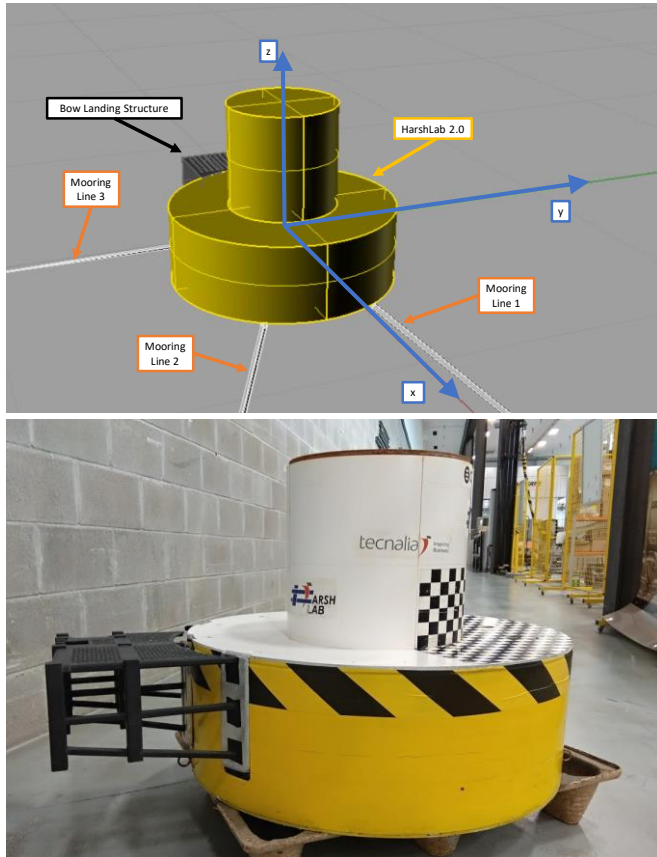


Figure 26 Representation of the numerical model and mooring system of the HarshLab 2.0 (top) and the physical model tested (bottom)

The model incorporates an attached structure to reproduce the boat landing, as shown in Figure 26, it has an influence on the hydrostatic stiffness and the viscous damping in pitch and heave as showed in Chapter 5. Due to its position it introduces a coupling effect between pitch-heave motions as well as between sway-yaw. The pitch-heave coupling effect, whose Morison coefficients are shown in Figure 28, has been fitted with the obtained forces in experimental oscillatory tests. However, the yaw-sway coupling effect has not been considered in the numerical model since all tests were performed with waves progressing along the positive  $x$  axis and none of them is significantly excited.

Table 2 Harsh 2.0 platform shape and its main properties

<i>Harsh 2.0 buoy shape</i>		
<i>Scale</i>	<i>1:1</i>	<i>1:13.6</i>
<i>Lower Diameter [m]</i>	<i>10.47</i>	<i>0.77</i>
<i>Lower Height [m]</i>	<i>3.54</i>	<i>0.26</i>
<i>Upper Diameter [m]</i>	<i>5.03</i>	<i>0.37</i>
<i>Upper Height [m]</i>	<i>4.76</i>	<i>0.35</i>
<i>Draft [m]</i>	<i>2.28</i>	<i>0.17</i>
<i>KG [m]</i>	<i>1.67</i>	<i>0.12</i>
<i>Water Depth [m]</i>	<i>68.00</i>	<i>5.00</i>
<i>Total mass [kg]</i>	<i>1.91E+05</i>	<i>76.02</i>
<i>Ixx [kg·m<sup>2</sup>]</i>	<i>2.84E+06</i>	<i>6.11</i>
<i>Iyy [kg·m<sup>2</sup>]</i>	<i>2.86E+06</i>	<i>6.14</i>
<i>Izz [kg·m<sup>2</sup>]</i>	<i>2.75E+06</i>	<i>5.91</i>

Hydrodynamic coefficients of the structure have been performed in this thesis with a commercial code based on the linear potential flow theory [62]. The numerical wave interaction model of the submerged part has been built for the 1:13.6 scaled geometry, without the attached boat landing shown in Figure 26. The hydrodynamic coefficients of the submerged cylindrical section are shown in Figure 27 in 1:13.6 scale.

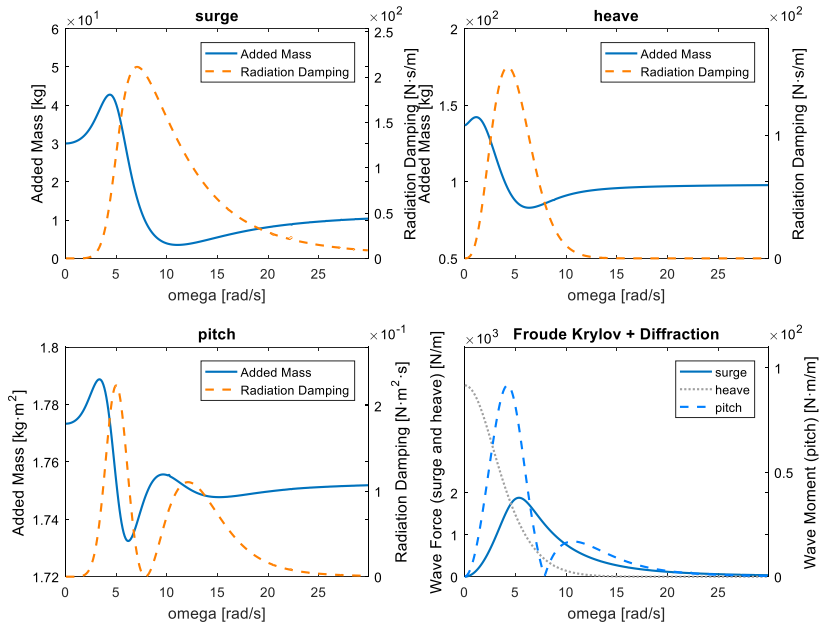


Figure 27 Hydrodynamic coefficients of the 1:13.6<sup>th</sup> scale floating buoy HarshLab 2.0 in surge, heave and pitch. Added mass and Radiation damping of surge (top-left), heave (top-right) and pitch (bottom-left). Froude-Krylov and diffraction forces in surge, heave and pitch (bottom-right)

Due to the axisymmetric geometry of the numerical model no heave-pitch interaction is obtained in the linear potential code coefficients. However, the attached structure for boat landing showed in Figure 26 introduces such coupling, that has been accounted for through the Morison equation.

The pitching moment has been measured in the forced oscillatory tests in heave. Three sets of forced tests, each of them with an amplitude and covering a relevant period range, have been utilized for that purpose. The measured moment has been fitted with the two factors of drag and inertia, as defined in 3.6.2.

$$M_{5fit} = f_{d-53} \cdot |\dot{\delta}_3| \cdot \dot{\delta}_3 + f_{m-53} \cdot \ddot{\delta}_3 \quad 3.6.2$$

$$M_{5bl} = -f_{d-53} \cdot |v_3 - \dot{\delta}_3| \cdot (v_3 - \dot{\delta}_3) + f_{m-53} \cdot (a_3 - \ddot{\delta}_3) \quad 3.6.3$$

$$F_{3bl} = -\frac{M_5}{x_{bl}} \quad 3.6.4$$

The resulting mean fitted factors of the set showed in Figure 28 have been  $f_{d-53}=15.25$  and  $f_{m-53} = 1.698$ .  $x_{bl}$  represents the horizontal distance from the center of gravity of the attached structure to the center of gravity of the whole structure, equal to 0.485m.

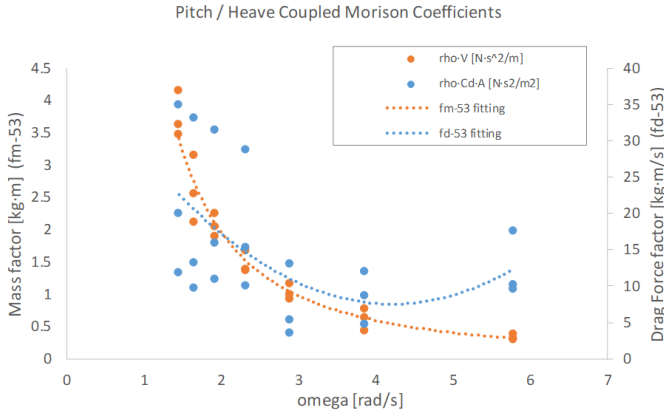


Figure 28 Heave-pitch cross coupling Morison coefficients

The overall influence of the attached boat landing structure in terms of drag, excitation and inertia effects have been included in the numerical *DynTD* model, in the force vector of the structure in equation 3.4.1. A Morison heave force and pitch moment, as defined by 3.6.4 and 3.6.3 respectively have been included. The viscous damping and hydrostatic stiffness introduced by the boat landing in each degree of freedom, have been assumed to be included in the decay test viscous force fitting and the additional stiffness pointed out in Table 12.

### 3.7 Chapter Summary

The four numerical tools developed along the work of this thesis have been introduced. Each of them represents a tool to assess floater body motions and mooring line tensions in a coupled model, based on different assumptions:

- Quasistatic Linearized Frequency Domain: It assumes the floating structure as a dynamic system and the mooring as a static one. The coupling consists in adding a horizontal stiffness in surge motion of the floater, solved in the *FD*. Based on the static properties of the mooring system and a maximum position of the structure, line tension and required length are computed.
- Quasistatic Non-Linear Time Domain: Floating structure is assumed as a dynamic system, coupled in all degrees of freedom with the catenary equations and solved in the time domain. Time series are postprocessed to assess line tension and required length.
- Dynamic Non-Linear Time Domain: Floating structure is considered as a dynamic system as well as the mooring system. It consists of a lumped mass and floating structure fully coupled model. Due to all non-linearities of the mooring system the coupled system is solved in the time domain. Time series are postprocessed to assess line tension and required length.
- Dynamic Linearized Frequency Domain: Floating structure is considered as a dynamic system as well as the mooring system. All non-linearities of the mooring system are linearized and the coupled model is solved in the frequency domain. Modal analysis of the coupled model is enabled. Line tensions are postprocessed based on the obtained *PSDs*.
- Two geometries are presented, along with their physical properties, that will be used as case studies to compare and validate the simulation tools developed in this PhD Thesis.

www.upv.es



Universidad  
del País Vasco

Euskal Herriko  
Unibertsitatea

## Chapter 4

# Comparison of Numerical Approaches in Extreme Conditions

### 4.1 Introduction

Extreme events have a significant relevance in the mooring system sizing and is one of the key aspects to consider from preliminary stages of design. In order to evaluate mooring motions and line tensions subject to extreme waves and currents, a comparison study has been carried out between the most widely used numerical methods currently in the offshore engineering sector, the *QSFD*, the *QSTD* and the *DynTD*. The tools used have been the *QSFD* and *QSTD* herein developed (see sections 3.2 and 3.3 respectively) and the commercial code Orcaflex [13] that uses the *DynTD* approach. During extreme events, mooring lines are subject to large loads and motions, mainly induced by the structure, which tend to be very influenced by non-linear effects. In principle, this fact makes the *QSFD* and *QSTD* not to be accurate enough to predict line tensions and mooring related cost. However, it is shown along this chapter that, after specific corrections, the *QSFD* method can be suitable for preliminary designs of the mooring system.

The present chapter aims at identifying the main sources of discrepancy among the three above-mentioned approaches for a set of realistic combinations of line mass and pretensions. A comparison based on numerical simulations is introduced to give an insight into the accuracy of the estimation of structure offset, maximum tension, total mooring mass and the required footprint, applied to the spar type floating *WEC* presented in 3.6.1. These parameters provide information to be



considered in a global perspective, together with other CAPEX items of the *WEC*, so that the design of the whole device can be kept optimised from early stages.

## 4.2 Numerical Model Settings

To design a mooring system for a *WEC*, extreme loads are to be accounted for with the device in the survival mode. There are multiple simulation combinations that may come up from considering real environments. However, in an early stage of design a case that initially produces large mooring line tensions can be selected in order to get estimations of both performance and cost indicators. The corresponding load case considered here assumes waves, wind and current are all aligned with one line of the mooring system, as indicated in Figure 29.

A single load case has been simulated with multiple combinations of lines' non-dimensional pretension and linear mass. The outcomes provide information about maximum offset and design line tension as well as the cost (mooring mass and required footprint).

### 4.2.1 Mooring Properties

The mooring system represented in the numerical model is a four-line catenary mooring system with the lines radially regularly distributed, as represented in Figure 29.

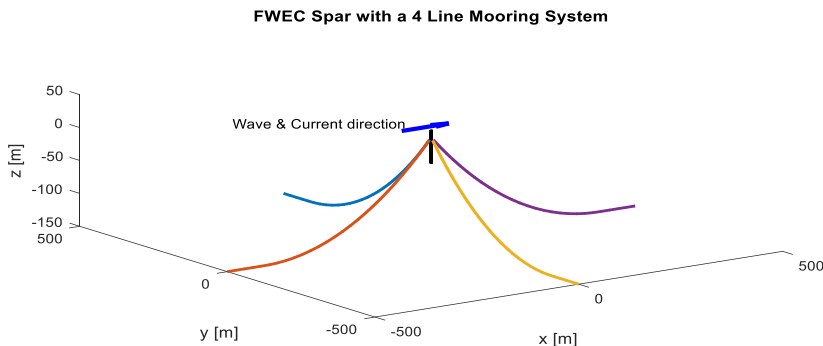


Figure 29 Four lines mooring system configuration modelled in 150m water depth

In order to assess the influence of non-linearities of the mooring system on structure motions and line tensions, a range of non-dimensional pretensions and linear mass has been defined as specified in Table 3, which results in 25 mooring models.

Table 3 Mooring properties selected to be combined for simulation cases

Mooring linear mass [kg/m]	Non-dimensional pretension	Length / Mass number
65	1,6	1
85	1,34	2
105	1,18	3
125	1,13	4
145	1,1	5

The vertical coordinate of the fairlead of mooring lines with respect to the seabed has been assumed to be 150m, assuming the fairleads at the center of gravity. Therefore, the resulting water depth is 181.97[m].

#### 4.2.2 Sensitivity Analysis of Simulation Settings

A sensitivity analysis was carried out with both *QSTD* and *DynTD* models in order to define the simulation settings. The *DynTD* model, made in Orcaflex [13] for the work developed within this chapter, in order to get a first estimation of the model comparisons, has been analysed with lines made up of 10 to 100 elements and the relative errors have been in all cases below 5%. The number of elements considered for the presented results have been 80 and a time step of 0.1s.

The *QSTD* model, made in the tool herein developed (see section 3.3), requires the catenary equations to be solved at each time step iteratively until an error bound is reached. This allowed error influences its results. In order to check the accuracy of the mooring force along the simulation, a sensitivity analysis has been carried out with the model presented in 3.3 to changes in the error bound allowed within the iterative loop.

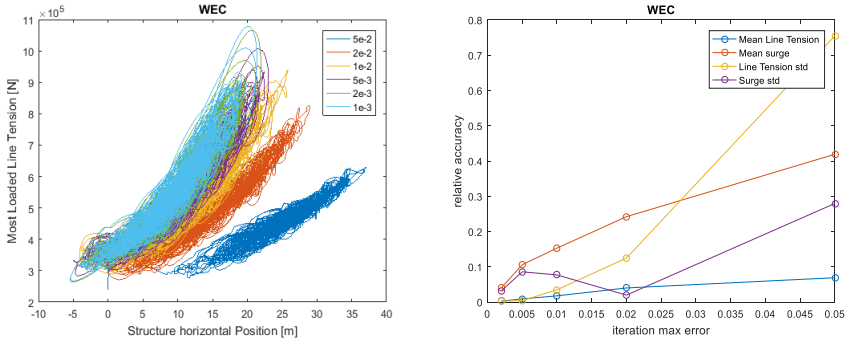


Figure 30 Sensitivity analysis of the  $QSTD$  iterative process. Surge of the structure and the corresponding mooring horizontal force (left) and relative errors of the standard deviation of both line tension and surge motion (right)

It is shown in Figure 30 that, with the  $QSTD$  model, both line tension and structure horizontal position relative errors are found below 5% for a maximum allowed error in the iterative process of catenary equations of 0.2%, assumed to be sufficiently accurate. This model has been proved to provide accurate results when using a time step of 0.1s with a Newmark-beta integration scheme, detailed in [49].

The reference case selected for numerical simulation corresponds with the recommended environmental conditions for permanent traditional offshore structures in [50], at the test site BiMEP, specified in Table 4.

Table 4 Environmental conditions for the reference simulation case

Parameter	Return Period [yrs]	Value
Significant Wave Height ( $H_s$ )	100	10 [m]
Peak Period ( $T_p$ )		18 [s]
Current Velocity ( $V_c$ )	50	1.3 [m/s]

The environmental data has been taken from [79], where an analysis of extreme climate conditions is presented for the site.

## 4.3 Results and Discussion

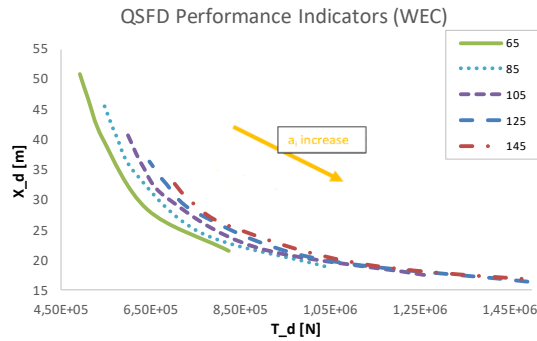
The *QSFD* model does not include any non-linear effect. Therefore, in order to assess the influence of non-linear effects of each approach, the *QSFD* results have been considered as a baseline whilst the results of both *QSTD* and *DynTD* approaches are compared with the baseline.

Consequently, the results are initially introduced for the *QSFD* approach, in terms of loads and motions as well as of the required line lengths and footprints. Results of the non-linear approaches are then compared with the *QSFD* baseline, drawing conclusions about the influence of the corresponding non-linear effects included in each model.

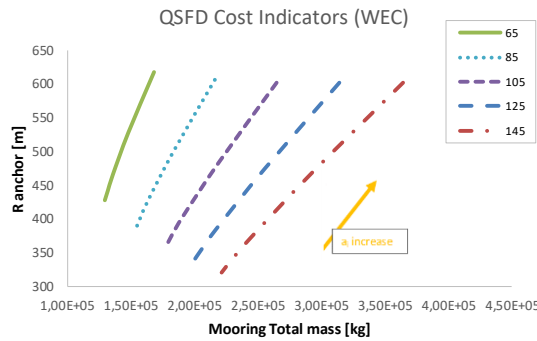
### 4.3.1 *Quasi-Static Frequency Domain Model Results*

This approach includes the horizontal stiffness added by the mooring system computed at the mean position to obtain the motion amplitudes, considering the mooring system coupled just with surge motion. It allows computing straightforward natural frequencies of the degrees of freedom of the structure in surge with the influence of the mooring system. Since the mooring settings are different among the model combinations arisen from Table 3, natural frequencies in surge have been observed to vary between 0.03[rad/s] and 0.07[rad/s]. Natural frequencies of the structure in heave and pitch without mooring system have been found to be 0.67[rad/s] and 0.38[rad/s] respectively.

Main performance indicators to be considered when designing a mooring system are the maximum line tension and the maximum structure horizontal offset. These parameters are relevant for the mooring system and umbilical cable structural integrity.



a)



b)

Figure 31 Baseline results of the *QSF* model. Performance indicators of line design tension and design offset a) and cost indicators of mooring total mass and anchor radius b). Yellow arrows indicate direction of lines pretension increase within each linear mass indicated in the legend.

Each line in Figure 31 represents a linear mass of the lines composing the mooring system, the variation of each performance and cost indicator along each linear mass is due to the variation in the non-dimensional pretension, increasing as indicated by the yellow arrow in Figure 31 within the values specified in Table 3. A non-dimensional pretension ( $a_i$ ) increase produces larger anchor radius ( $R_{\text{anchor}}$ ) and lower design offset ( $X_d$ ) in all cases.

A pretension increase influences the offset of the structure almost independently of the line mass, however, it also increases significantly

the design tension which may lead to unsafe designs as shown in Figure 31 a). The design offset of the structure is very sensitive to the linear mass at mid-low pretensions, however, with large pretensions, i.e.  $a_i > 1.2$ , the variation of the offset due to the linear mass (65[kg/m] – 145[kg/m]) becomes less significant.

Large pretensions imply in general larger footprints and total mooring mass, that are eventually translated into larger total costs of the mooring system. Similarly to what is observed for the offset, the anchor radius is very sensitive to the linear mass at mid-low pretensions, however with high pretensions the influence on the anchor radius is significantly lower, which is represented in Figure 31 (right).

It should be pointed out that these baseline results indicate a requirement in the mooring total mass of 5-15% the mass of the structure, as long as lines are completely made up of a section of one chain type.

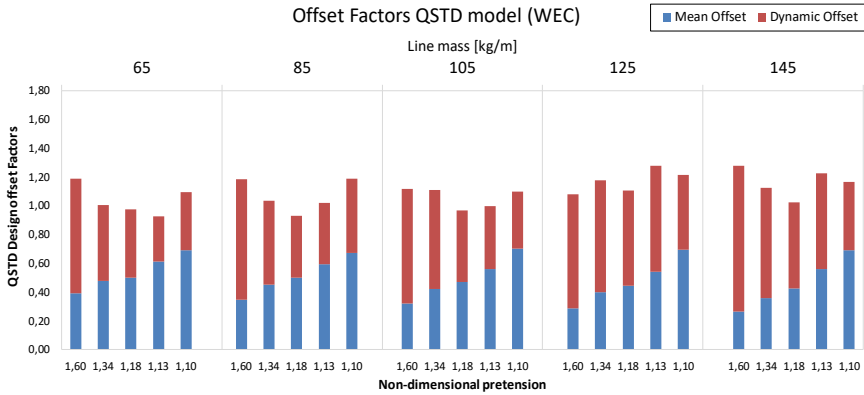
#### ***4.3.2 Performance Results of Non-Linear QSTD and DynTD Models***

To quantify the uncertainty of the *QSF*D baseline performance indicators, results of both time domain models are introduced as factors with respect to the indicators introduced in Figure 31. It enables quantifying the influence of non-linear effects such as the geometric stiffness or lines' drag and inertia as well as the influence of coupling all degrees of freedom with the mooring system.

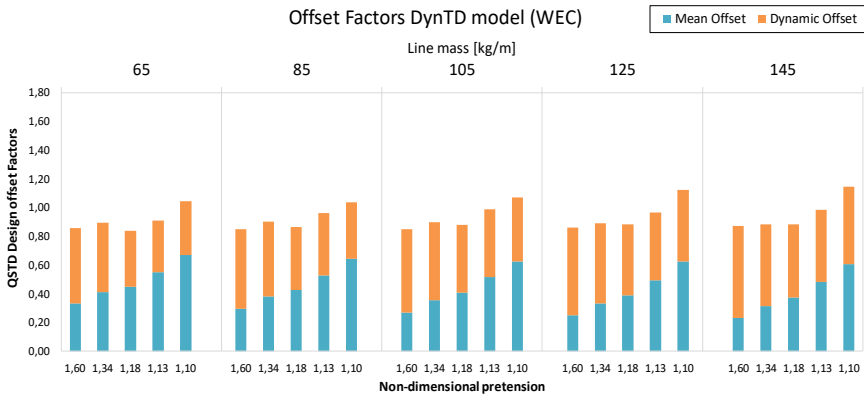
##### *4.3.2.1 Floater Motions*

The most significantly excited degrees of freedom in the introduced numerical models are surge, heave and pitch motions since all environmental forces have been aligned and propagated along the positive X axis. These directly influence line tensions and the structural integrity of the umbilical cable that any *WEC* must have installed in order to transport electrical energy. Surge motion of the structure (horizontal offset) is one of the most influencing parameters for the design of the umbilical cable, analyzed in detail in the following

paragraphs. The design offset has been computed with each approach following the same procedure as indicated for the corresponding line tensions through sections 3.2 to 3.4 and presented as factors with respect to the *QSFD* in Figure 32.



a)

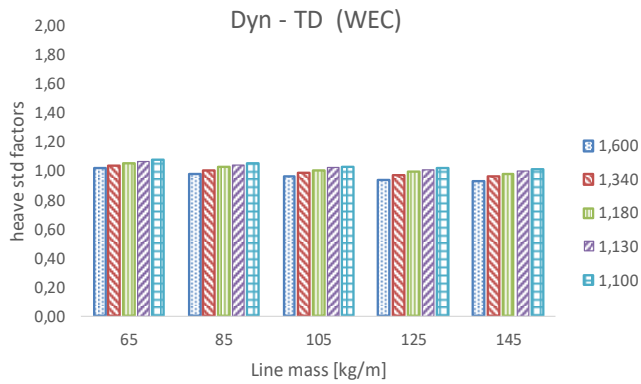


b)

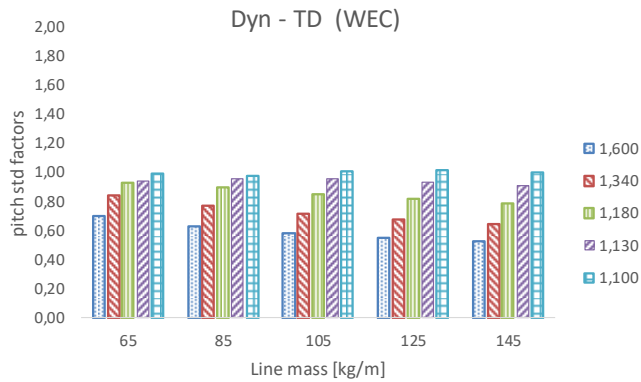
Figure 32 Surge factors with respect to *QSFD* model of the *QSTD* a) and *DynTD* b) approaches. Accumulated bars with the contribution of the mean and dynamic offsets

The *WEC* shows in Figure 32 a balanced influence between the mean and dynamic surge on the design offset factors. Mean offset contribution is significantly increased as the non-dimensional

pretension is decreased with slightly higher influence in the *QSTD* model. The total offset factor is dominated by structure dynamics with large non-dimensional pretensions and by the mean offset with low non-dimensional pretensions. It is to be noted that most mooring models show factors  $<1$  for the design offset with the *DynTD* model, whilst the *QSTD* model shows factors  $>1$ . It indicates, assuming that the most reliable model is the *DynTD* approach, that the *QSF* model is more conservative in the estimation of the design offsets of the structure rather than the *QSTD* for this kind of *WECs*.



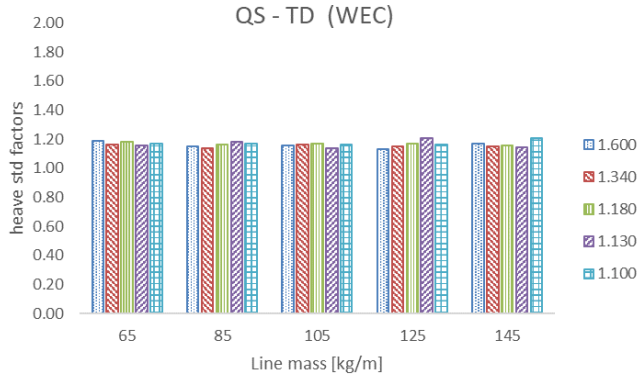
a)



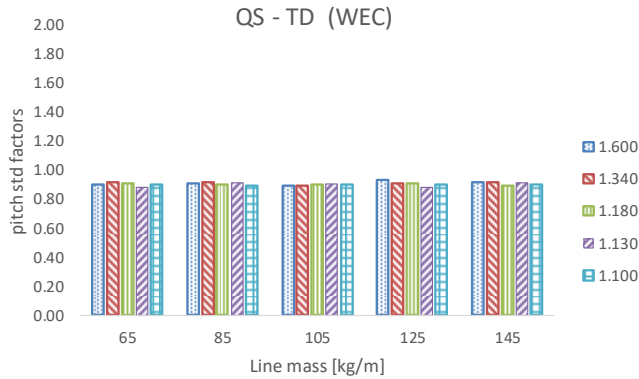
b)

Figure 33 Heave a) and pitch b) std factors of the *DynTD* models





a)



b)

Figure 34 Heave a) and pitch b) std factors of the *QSTD* models

Factors of the *QSTD* approach in terms of heave and pitch standard deviations are presented in Figure 34, showing almost constant values, 15% to 20% in heave and -10% in pitch. Nevertheless, the *DynTD* approach shows heave factors within the range of -8%, for high pretensions, to 8%, for low pretensions as shown in Figure 33 a). Pitch motion with *DynTD* approach also shows increasing factors with a decreasing pretension, as observed in Figure 33 b), though significantly more influenced by lines drag compared with heave.

The increase of the standard deviation factors with pretension increases can be explained looking at the *PSDs* of each degree of freedom, shown in Figure 35. Mooring systems with low non-dimensional pretension provide surge motions in good agreement in the natural frequency among all models as well as in amplitudes, as shown in the *PSDs* in Figure 35. However, mooring systems with large non-dimensional pretensions show damped surge *PSDs* at the natural frequency with the *DynTD* models, which can be observed in Figure 35 a).

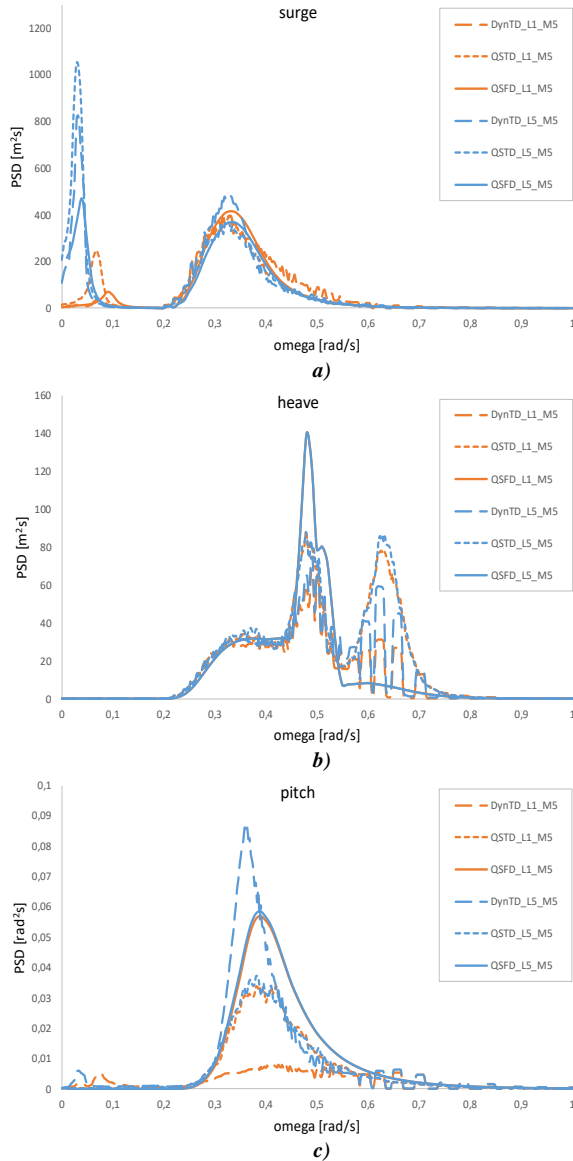


Figure 35 Power spectral densities in surge ( $WF$  magnified 20 times) (a), heave and pitch motions ( $WF$  reduced by a factor of 2) (b) and (c) comparing models' performance with the largest and lowest non-dimensional pretension.

Heave motion shows factors  $>1$  in all cases as the heaving natural frequency is overdamped with the linearized *QSFD* model, which corresponds with the second peak in Figure 35 b). Even though all time domain models show larger standard deviations in heave, *DynTD* models introduces a slightly higher damping in the heaving motion with respect to the *QSTD*. It results in an underestimation of the *QSFD* and overestimation of the *QSTD*.

Pitching motion standard deviation factors are due to the combination of two effects: on the one hand the *QSTD* models do not catch entirely the surge-pitch coupling introduced by the mooring system, and on the other hand large non-dimensional pretension models show damped pitch *PSDs* with the *DynTD* models in the wave frequency range. Additionally, the *QSFD* model shows slightly underdamped *PSDs* in the wave frequency range, with respect to the *TD* models, which results in the -10% above-mentioned factors of the *QSTD* models.

Therefore, mooring systems with large non-dimensional pretensions introduce significant damping in all degrees of freedom as observed with the *DynTD* approach. It reduces the response specially in the corresponding natural frequency, reducing its standard deviation. The fact that the *QSFD* approach overdamps motion responses due to the linearization, partially balances the viscous damping introduced by the mooring system showed with the *DynTD*. This mooring induced damping is not represented with the *QSTD*, what makes it to overestimate structure motions.

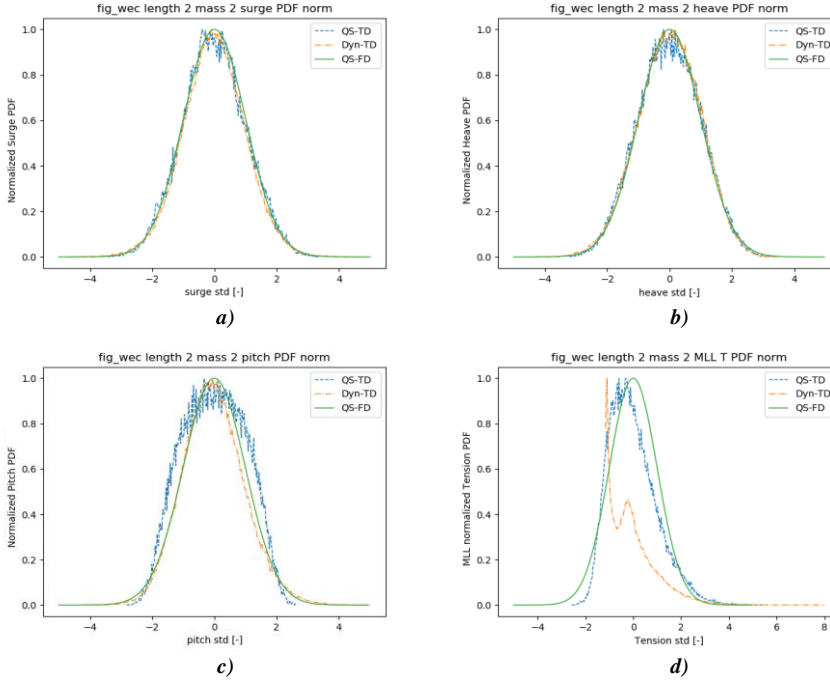


Figure 36 Normalized *PDFs* with the three models in surge a), heave b), pitch c) and the most loaded line tension d)

In Figure 36 and Table 5 normalized probability density functions (*PDF*) and their corresponding kurtosis (excess kurtosis with respect to the gaussian distribution) and skewness are introduced respectively for surge, heave, pitch and the most loaded line tension. The kurtosis indicates the sharpness of the distribution around the mean value, higher kurtosis indicates higher probability of producing extreme values. It is generally provided as the difference with respect to the kurtosis of the gaussian distribution, equal to 3, denoted as the excess kurtosis. The skewness indicates the asymmetry of the distribution about the mean value, gaussian distributions have zero skewness. Positive skewness indicates higher probability of producing extreme values. In Table 5 the corresponding values of the *QSFD* models have been omitted since it is a linear model and, therefore, they are Gaussian distributed with kurtosis equal to 3 and skewness equal to 0.

The *QSTD* approach shows negative excess kurtosis and skewness in all *DOFs*, with very homogeneous values among the mooring settings considered, whose average values are shown in Table 5. The most influenced degree of freedom with this approach is the pitch motion with a significantly low kurtosis while heave and surge provided slightly low kurtosis and skewness values. The most loaded line tension shows positive excess kurtosis as well as skewness, that differ clearly from the equivalent linear *PDF*, as represented in Figure 36. It is coherent with the catenary equations as it restricts floater motions through a non-linear increase of line tensions with the offset increase (commonly fitted with a 3<sup>rd</sup> order polynomial). Generally, these results mean that extreme motions are reduced, and extreme tension values are increased with respect to the linearized *QSFD*.

Table 5 Mean obtained kurtosis and skewness of the *WEC* motions and tension of the most loaded line with the non-linear *QSTD* approach

<i>WEC</i>	<i>SURGE</i>	<i>HEAVE</i>	<i>PITCH</i>	<i>MLL TENSION</i>
<i>KURTOSIS (QSTD)</i>	2,924	2,671	2,241	3,700
<i>SKEWNESS (QSTD)</i>	-0,188	-0,039	-0,050	0,665

Including lines' drag and inertia, in the *DynTD* approach, structure motions are modified as already pointed out in the *PSD* analysis. Heaving motions show also homogeneous excess kurtosis and skewness among the mooring models, with similar tendencies as those found with the *QSTD*, whose values are shown in Figure 37. Surge, pitch and most loaded line tensions show variable values depending mostly on the non-dimensional pretension. Surge motion shows higher positive kurtosis with higher pretensions and a kurtosis closer to 3 as the pretension is decreased. The skewness tends to negative values with lower pretensions and shows a tendency to the values represented with the *QSTD* approach. It indicates that the damping induced by the mooring system with high non-dimensional pretensions induces higher excess kurtosis and positive skewness while the negative skewness may be more attributed to the non-linear geometric stiffness. Although not as clear as in surge, pitch motions show the same apparent tendency to the values of the *QSTD* approach as lines pretension is lowered in

Figure 37 and same conclusions apply in terms of relations of physical effects with the non-linearity influence type. Most loaded line tensions show the opposite tendency, as lines pretension is lowered its kurtosis and skewness is further increased, producing even larger extreme line tensions compared with the *QSTD* approach. This is further analyzed in the following section, about line tensions.

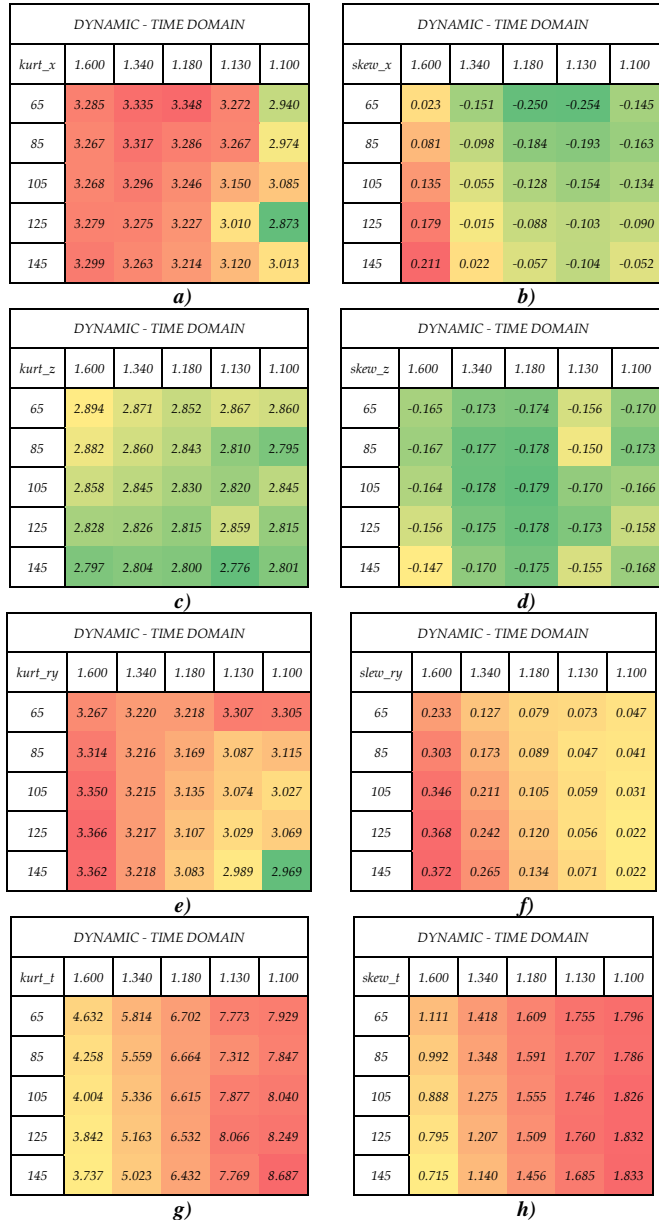


Figure 37 Kurtosis and skewness of surge motion (a)(b), heave motion (c)(d), pitch motion (e)(f) and most loaded line tension (g)(h) obtained with the *DynTD* approach



### 4.3.2.2 Predicted Line Tensions

The design line tension has been computed for all cases as defined through sections 3.2 to 3.4. The differences come from the non-linearities included in each model i.e. the non-linear geometric stiffness and line's drag and inertia forces.

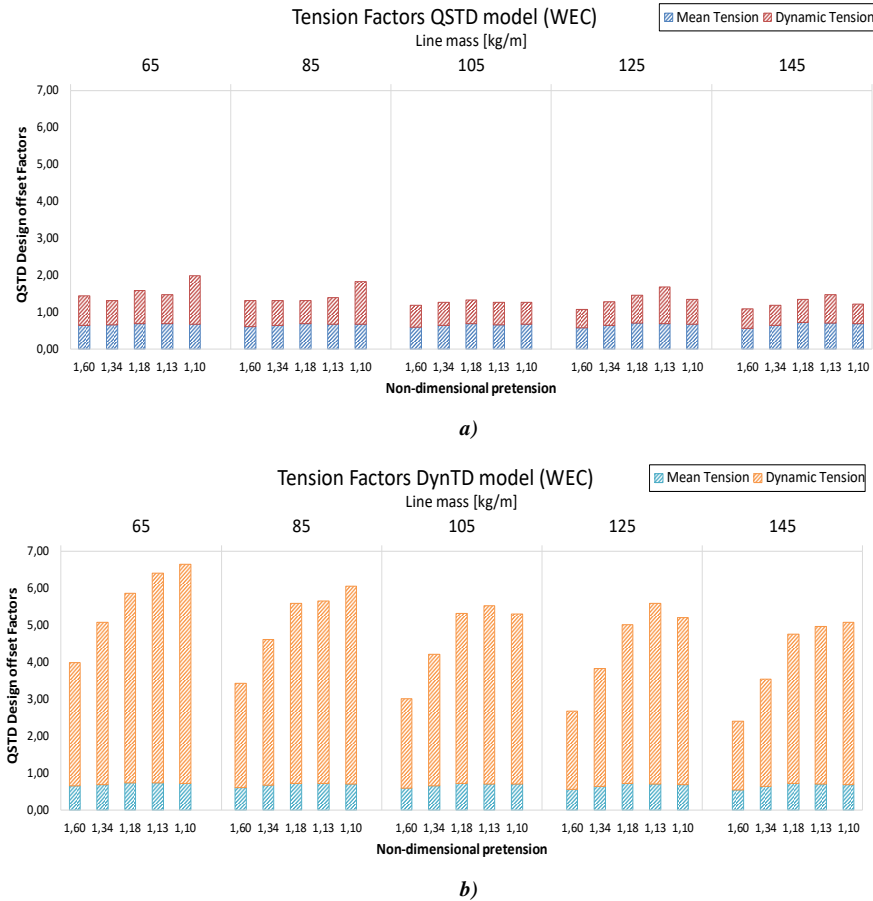


Figure 38 Most Loaded Line tension factors for the *WEC* with the *QSTD* a) and *DynTD* b) models

The mean line tension, computed with both approaches, shows contributions 55%-75% on the design line tension. It is not significantly sensitive to the mooring settings and the observed differences in the

design line tension are driven by line tensions induced by structure motions. The *QSTD* approach shows factors of 1,5 to 2 with a partially increasing tendency with decreasing pretensions in Figure 38 a). On the other hand, the *DynTD* approach shows increasing factors from 4 to 7 as the line pretension is decreased.

Line tension *PDFs* obtained with the *QSTD* approach show clear positive skewness and excess kurtosis in general, produced by the geometric stiffness, as showed in Table 5. In addition, its coupling with heave, shown in Figure 39, may induce slightly larger excess kurtosis of line tensions, as well as larger negative skewness in heave.

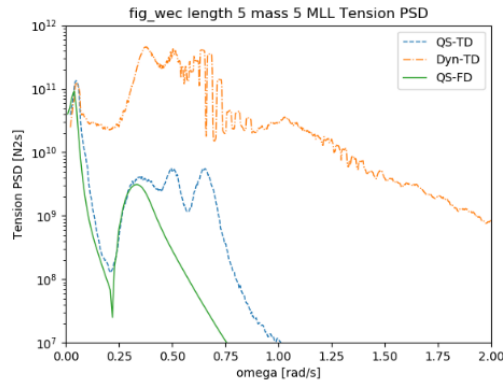


Figure 39 Most loaded line tension *PSDs* comparison with the approaches considered

Nevertheless, with the *DynTD* approach, in contrast to the tendency of structure motions to perform more linear motions with lower non-dimensional pretensions, line tensions show increasing excess kurtosis and skewness as the pretension is decreased, which can be observed in Figure 37.

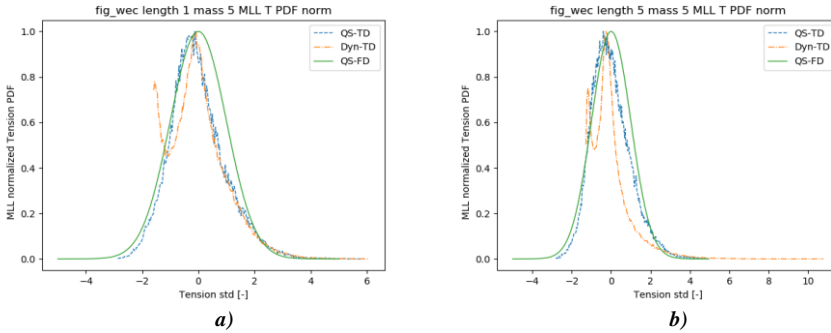


Figure 40 Normalized *PDFs* of the most loaded line with the three approaches. High pretension a) and low pretension b)

Analyzing further the most loaded line tensions with the *DynTD* approach, its *PDFs* show two local maxima in Figure 40. The maximum at higher tensions is due to surge dynamics which tends to perform more similarly to the *QSTD* model. However, the peak at lower tensions is due to slack lines during certain instants, which occurs due to the heaving of the buoy and to lines' inertia, also known as snap loads. This effect is clearly observed in Figure 41, where a clear correlation of slack line instants with negative heave velocity is observed and not showing a clear correspondence with surge dynamics.

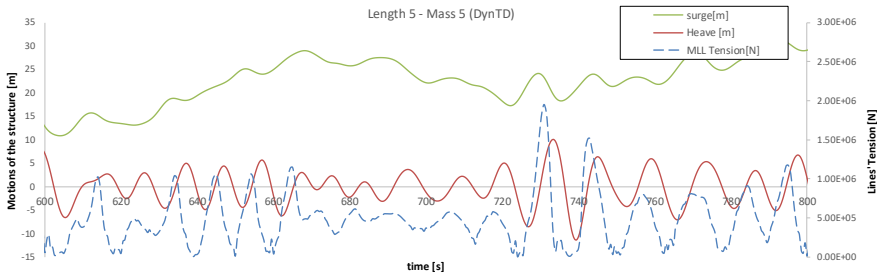
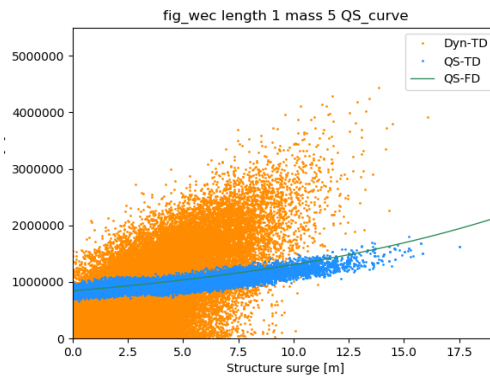


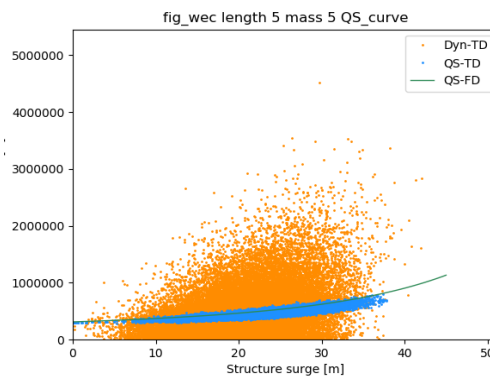
Figure 41 Time series portion of buoy heaving and the corresponding tension of the most loaded line

In Figure 42 the *QSTD* approach also shows a significant variability in line tension with respect to the quasistatic curve as a consequence of

the structure's heaving. However, the *DynTD* approach shows a very large line tension dispersion due to lines' drag and inertia. The latter produces the mentioned snap loads. These snap loads cannot be reproduced with neither the *QSFD* nor the *QSTD* approaches, leading to significantly underestimating lines tension with low pretensions. On the other hand, looking at the low frequency range in Figure 39 there is good agreement between the *QSTD* and *DynTD* as it appears to be decoupled from the heaving motion.



a)



b)

Figure 42 Line tension of *WEC* with large pretension a) and low pretension b) for three models. Green: *QSFD*, Blue: *QSTD* and Orange: *DynTD*.

Consequently, even though the estimation of lines' tension with the *QSTD* approach shows the influence of the heaving motion with respect to the *QSFD*, both of them differ significantly with respect to the *DynTD* with high pretensions mainly due to the lines induced damping and with low pretensions due to lines' inertia.

### ***4.3.3 Performance and Cost Comparison Results of Numerical Models***

The design spaces represented in Figure 31 are represented together with the corresponding results obtained with the *QSTD* and *DynTD* approaches in Figure 43. Both performance and cost indicators show same tendencies with the three approaches and what has been stated with the *QSFD* model still applies. Nevertheless, design line tensions resulting from the *DynTD* approach with respect to the other two approaches differ by factors of 2 to 7, as already showed in Figure 38, depending on lines' pretension. It is to be considered if any of the two introduced quasistatic approaches is to be used at preliminary design stages so that acceptable line strength is obtained.

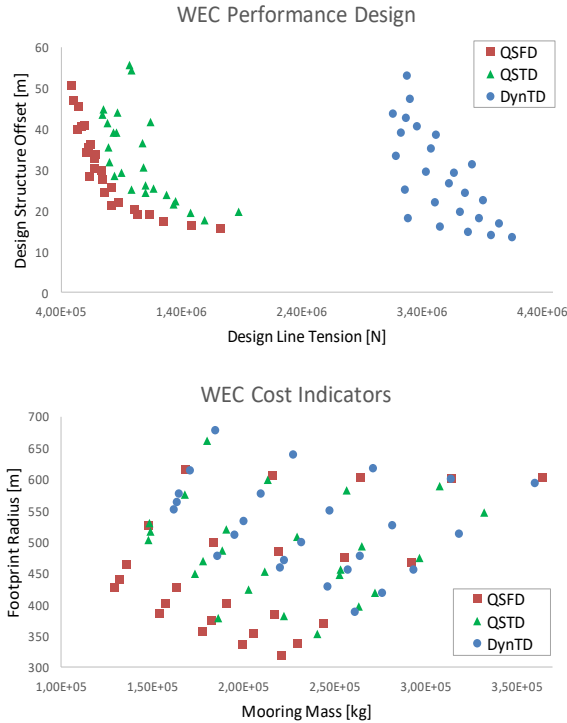


Figure 43 Design (top) and cost (bottom) spaces for the *WEC* structure with the *QSF* (red squares), *QST* (green triangles) and *DynTD* (blue circles) models

The mooring total mass and the footprint radius show increasing values as the complexity of the model increases. In addition, the large influence of lines’ drag and inertia observed in the design tension is not translated into a significant increase of the suspended line length and anchor radius. This enables the comparison of models in terms of mooring cost estimates.

The computational time required of both the *DynTD* (executed with the commercial code *Orcaflex* in this chapter, developed on Pascal [80]) and the *QST* models is close to real time with the settings specified in section 4.2.2, when ran in a common laptop equipped with an Intel i7 7<sup>th</sup> generation microprocessor. These approaches require 10 and 5 3-hour time domain simulations respectively. On the other hand, the *QSF* model runs require a few seconds to reproduce the response in *Comparison of Numerical Approaches in Extreme Conditions*

all frequencies, just due to the iterations required by the drag linearization. Nevertheless, it should be noted that the *QSTD* tool developed here has been coded on Matlab, which tends to be slower than C, FORTRAN or Pascal.

Therefore, the *QSTD* approach shows both total mooring mass and anchor radius closer to those of the *DynTD* rather than the *QSFD*, which would make it suitable for optimizations. However, it does not add significant accuracy improvement in terms of line tensions, and it requires a computational time of the same order of the *DynTD*. Consequently, it has not been considered suitable for preliminary optimizations.

Given the differences observed between the *QSFD* and the *DynTD* resulting from the linearization, and not considering the influence of heave in the *QSFD*, correction coefficients are proposed in Figure 44 in order to obtain more accurate cost estimates. Since lines' pretension have been observed to be more influencing on differences between models compared to lines' mass, the corrections proposed here are linear functions of lines' non-dimensional pretension.

In addition to the cost indicators, i.e. anchor radius and suspended line mass, designers must bear in mind that line tension factors are significant, as showed in Figure 44 c). It is notable with low pretensions and, in order to obtain acceptable line strengths, corrected line tension should be checked during any design optimization carried out with the *QSFD* approach.

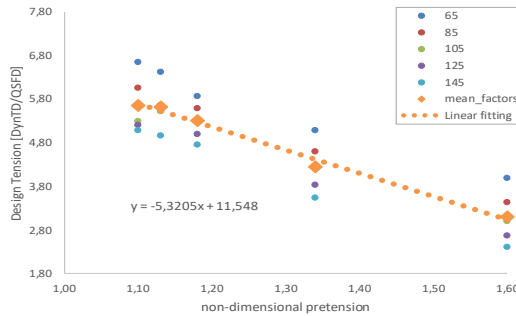
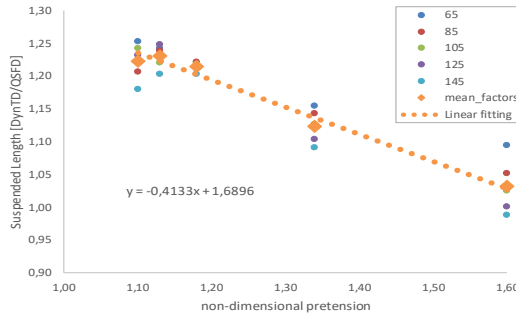
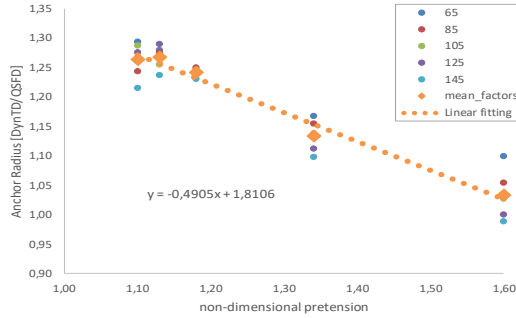


Figure 44 Correction factors between the *DynTD* and the *QSFD* models for five linear mass values (65, 85, 105, 125 and 145) and a linear fitting of the mean values for Anchor Radius (a), Suspended length (b) and Design Tension (c)



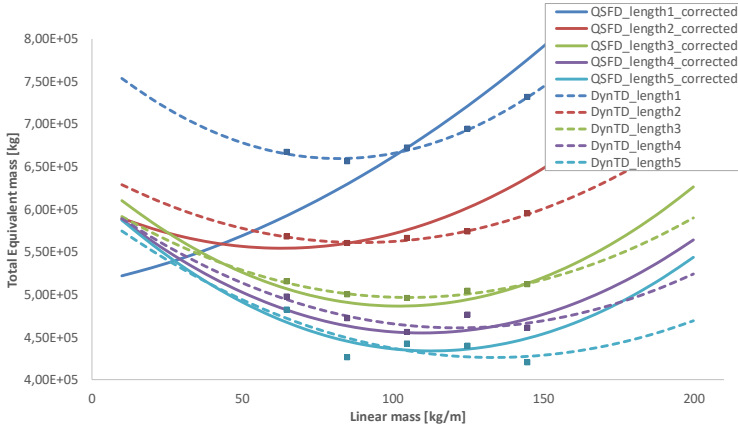


Figure 45 Cost optimization of the mooring system. Total cost is the sum of the lease area and the total mooring mass assuming a cost ratio of 3 [€/kg]/[€/m<sup>2</sup>]

When using these models for mooring design optimization, as described above, *QSF D* may be used provided it is corrected following coefficients proposed in Figure 44. In order to compare design optimization results of corrected *QSF D* and *DynTD* approaches Figure 45 is introduced. The mooring design optimization has been here considered as the sum of the required area [m<sup>2</sup>] and the total mooring mass, computed with the maximum suspended length resulting with each approach and applied to all lines of the mooring system. The cost has been provided in terms of the total equivalent required mass. The equivalent required mass is the summation of the mooring mass, assuming lines made up of a single chain type, and the equivalent mass of the footprint area given a cost ratio. Assuming a cost ratio of  $\frac{[\text{€/kg}]}{[\text{€/m}^2]} = \frac{3}{1}$ , total computed costs are represented in Figure 45 with both models. It results in increasing costs with increasing pretensions independently of the linear mass, and higher optimum linear mass with decreasing pretensions. It is derived from Figure 45 that the *QSF D* approach seems applicable for early stage optimizations with mid to low linear pretensions, i.e. <1.2. Obtained cost values differ by a 10% and it can acceptably be utilized only for preliminary design optimizations, setting tendencies of offset, footprint and total required mass, along with

design line tensions as long as corrections in Figure 44 are accounted for.

#### 4.4 Chapter Summary

The three state-of-the-art coupled approaches are compared in terms of structure motions, line tensions and required lines mass and footprint applied to a catenary moored floating *WEC*. The tools used have been the *QSFD* and *QSTD* herein developed and the commercial code Orcaflex that uses the *DynTD* approach. The following main conclusions have been obtained:

- *QSFD* approach shows increasing line tensions and required mass with no benefits in structure offset and footprint with moderate line pretensions ( $>1.2$ )
- Floater motions are overdamped with the *QSFD* which partially covers the mooring induced damping shown in the *DynTD*. It makes motion estimates of the *QSFD* closer to the *DynTD* than those of the *QSTD* approach
- Mooring induced damping is larger with larger pretensions which induces larger motion excess kurtosis and in general larger differences of the QS approaches with respect to the *DynTD*. On the other hand, non-linear geometric stiffness induces negative skewness of motions *PDFs*
- Line tensions with the *DynTD* approach show significant differences with respect to the QS approaches with large pretensions, mainly attributed to the mooring induced damping. These differences become larger for low pretensions as the *DynTD* model shows increasing snap load probability due to the heaving motions of the structure
- Mooring sensitivity analyses can be performed with the *QSFD* approach in early stages, provided representative correction factors are applied. It has been shown that the corrected results are representative as long as the lines non-dimensional pretension are low to intermediate ( $<1.2$ )

1959ko irailaren 25ean



Universidad  
del País Vasco

Euskal Herriko  
Unibertsitatea

## Chapter 6

# Numerical Verification of the Dynamic Linearized Frequency Domain Model

### 6.1 Introduction

Floating structures moored by means of catenary mooring systems tend to be designed with a very low horizontal stiffness, what makes them to be sensitive to the low frequency wave drift forces. Such low frequencies play a key role in lines tension spectra and, to reproduce them, significantly long simulations are needed. In addition to the simulation length, shorter elements in the lumped mass approach require shorter simulation time steps, resulting in time consuming simulations, especially when multiple combinations of parameters need to be analyzed in early design stages.

The lumped mass numerical model has been proved to be accurate for the computation of line tensions of catenary mooring systems in Chapter 5. It is especially appropriate for mooring line tension assessment under extreme conditions, given the non-linear behavior showed in Chapter 4. However, fatigue limit states or assessment of control strategies are carried out in the most occurrent sea states (with low to moderate energy), where the non-linear effects are of lower relevance and the number of load cases are increased.

Consequently, this section presents the verification of the linearized *DynFD* with the *DynTD* under operational conditions, both developed in this thesis. The *DynFD* is based on the method introduced by [22] and extended in section 3.5 with a linearized stiffness matrix to account for the geometric stiffness influence on both structure and lines, applied to the *WEC* introduced in section 3.6.1. The outcomes of the linearized

*DynFD* are presented and compared with its non-linear counterpart, *DynTD*, subject to the most occurrent sea states at BiMEP site [85]. The accuracy of the model is assessed, and a modal analysis of the coupled model is enabled, pointing out the most apparent limitations of this approach.

## 6.2 Numerical Model Settings

Both numerical tools used in this chapter, the *DynFD* and the *DynTD*, will be used to build the respective models based on a floater geometry, the selected mooring settings and the environmental conditions that the model will be subject to. The floater geometry is the spar *WEC* used in this thesis as a reference, described in section 3.6.1, in the power production mode. Its linear hydrodynamic coefficients have been obtained modelling two diffracting bodies in the commercial software [62]. One body with the geometry of the spar, represented in Figure 67 and defined in [16] as model *K*, and a massless surface to model the internal water surface level.

In order to model the internal water surface horizontal motions, in surge, sway and yaw, rigidly with the spar structure, three kinematic restrictions have been imposed to both bodies, following equation 3.4.5. Additionally, they have been left to move independently in heave, roll and pitch. The *PTO* has been assumed not to introduce any stiffness in the model and the optimal *PTO* damping to maximise the extracted energy has been computed with the frequency domain model accounting only for the body motions in heave, without the mooring system and with the linearized drag term. The obtained values are represented in Figure 25.

### 6.2.1 Mooring System

The mooring system for the model verification has been assumed to be made up of three catenary lines as described in Figure 67 and specified in Table 16. The corresponding lines are made of a single chain section with the properties specified in Table 17 and equivalent to the properties

considered in the previous chapter, in Table 7. The corresponding non-dimensional pretension of the lines, following equation 3.2.7, is 1.43.

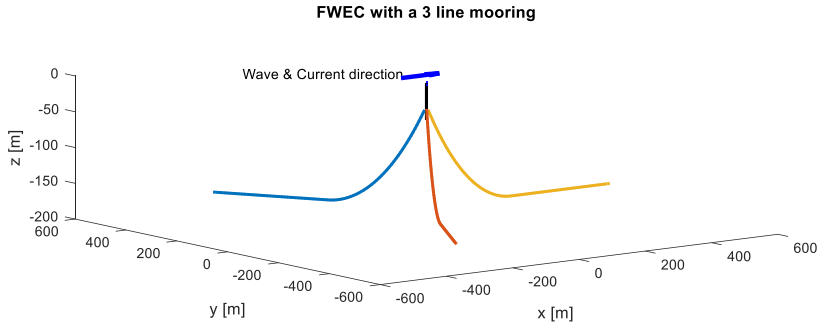


Figure 67 Floating WEC with the three-line mooring system

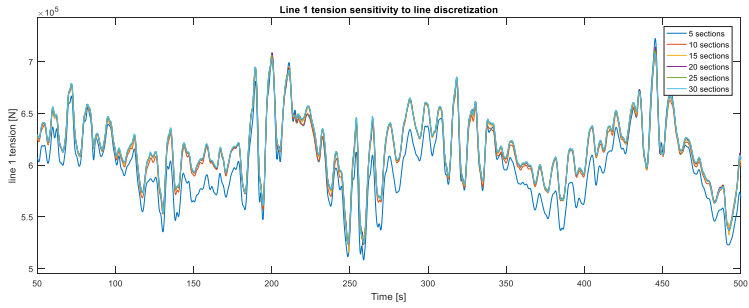
Table 16 Mooring line lengths, fairleads and anchor points

Property	Line 1	Line 2	Line 3
$x_{fairlead}$ [m]	-1.5	-1.5	2.9
$y_{fairlead}$ [m]	-2.6	2.6	0.0
$z_{fairlead}$ [m]	-32.0	-32.0	-32.0
$x_{anchor}$ [m]	-277.0	-277.0	554.0
$y_{anchor}$ [m]	-479.8	479.8	0.0
$z_{anchor}$ [m]	-172.0	-172.0	-172.0
Length [m]	590.0	590.0	590.0

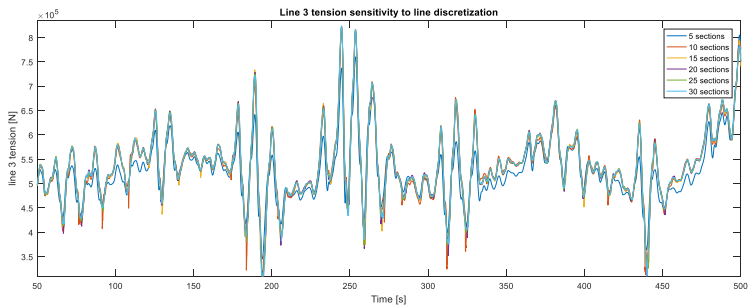
Table 17 Mooring line properties

<i>Mooring Lines Properties</i>	
<i>Property</i>	<i>Value</i>
<i>Equiv. Young Modulus [Pa]</i>	<i>3.35E+10</i>
<i>Equiv. A [m<sup>2</sup>]</i>	<i>1.78E-02</i>
<i>Linear mass [kg/m]</i>	<i>140</i>
<i>Rayleigh Damp Coeff</i>	<i>0.001</i>
<i>Seabed friction Coeff</i>	<i>0.5</i>
<i>Ca (axial)</i>	<i>0.5</i>
<i>Ca (radial)</i>	<i>1</i>
<i>Cd (axial)</i>	<i>0.6389</i>
<i>Cd (radial)</i>	<i>1.33</i>
<i>Hydrodynamic Diameter [m]</i>	<i>0.151</i>

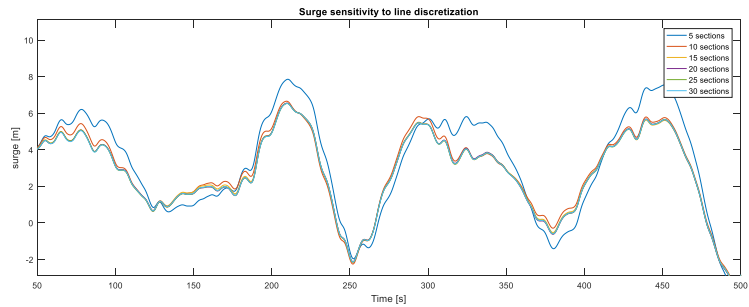
In order to select the appropriate number of line sections and the integration time step, a sensitivity study has been carried out. The resulting time series with increasing number of sections are showed in Figure 68 for fairlead tensions of lines 1 and 3 and surge. The relative error of the corresponding standard deviations with increasing number of line elements are plotted in Figure 69. Lines discretization with 15 elements show relative errors below 5% both in lines tension and in surge motion. Therefore, it was decided to consider mooring lines made up of 15 sections, as a trade-off between computational time and accuracy.



a)



b)



c)

Figure 68 Resulting time series of the sensitivity analysis to the number of sections used to discretize each mooring line. Time series of line 1 a), line 3 b) and surge c)



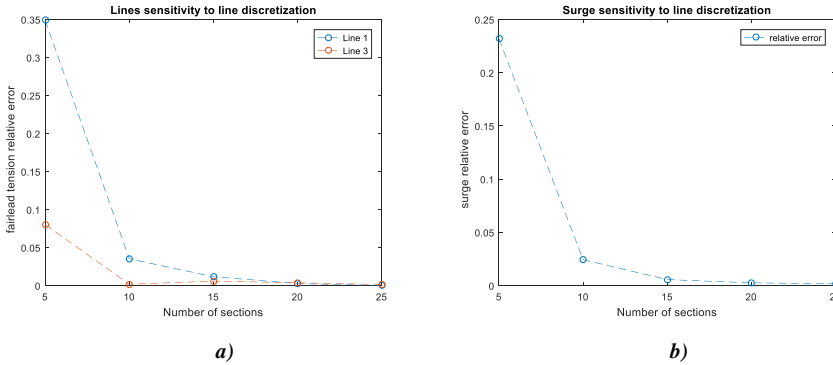


Figure 69 Relative errors found in standard deviations of the sensitivity analysis to the number of line sections. Relative errors of the standard deviations of lines 1 and 3 a) and surge b)

In addition, a simulation with 15 sections and half the time step, 0.01s, has been performed. The relative error of the standard deviation of the simulation with the original time step with respect to the simulation with a time step of 0.01s has been checked for the surge motion and tensions of lines 1 and 3. The error in surge was found to be of  $7.3 \cdot 10^{-3}\%$  while in line tensions of lines 1 and 3 were  $7.6 \cdot 10^{-2}\%$  and  $3.7 \cdot 10^{-2}\%$  respectively. Therefore, it has been decided to maintain the time step in 0.02s for all the verification cases.

### 6.2.2 Sea States for Dynamic Frequency Domain Verification

The WEC here analyzed has been subject to the most occurrent (>1% annual time) sea states at the BiMEP test site [50], pointed out Figure 70. It covers 63% of the annual time with a reduced number of simulation cases, 36 sea states, that also cover a wide range of  $H_s$  and  $T_p$  values, considered enough for verification in operational conditions. In the performed simulations the current and wave propagation directions have been assumed aligned with the global X axis, in the positive direction, as specified in Figure 69.

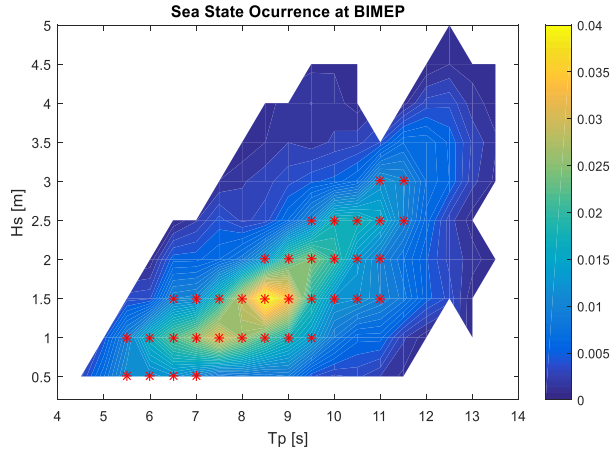


Figure 70 Sea State Occurrence probability at BiMEP sea test site [50] and the Sea States with more than 1% occurrence probability (red stars), selected for *TD* and *FD* simulation verification

The spectral shape considered has been a JONSWAP with a gamma factor equal to 3.3 in all sea states. The current force has been considered as a constant force induced by the mean current speed. A representative current speed in operational conditions of 0.5m/s has been assumed. The projected vertical surface of the submerged part of the *WEC* into the current direction is 290[m<sup>2</sup>] and a common drag coefficient of 0.65 has been assumed.

### 6.3 Results and Discussion

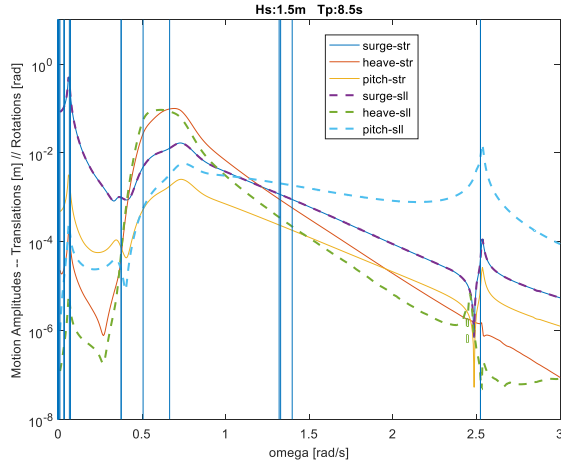
The results of simulations with the *DynFD* model, introduced in 3.5.9, have been compared with the corresponding simulation with the *DynTD* non-linear coupled model, described by equation 3.4.1. Results in terms of motion and line tension *PSDs* are compared and the differences have been quantified through the relative error of standard deviations of the *DynFD* model with respect to the non-linear *DynTD* model. *WEC* and mooring loads and motions have been obtained with 12 one-hour *TD* simulations, assumed to be large enough to represent some hundreds of *LF* cycles to provide good *PSDs*. An additional initialization period of 500s has been simulated that has been disregarded for the *PSD*

computations. The *PSDs* of the time series have been computed through the *pwelch* subroutine within the Matlab software [82]. Since the *FD* model has been linearized, an eigenvalue and eigenvector analysis has been carried out and is subsequently presented. It allows a deeper analysis and understanding of the extent of the applicability of the linearized model.

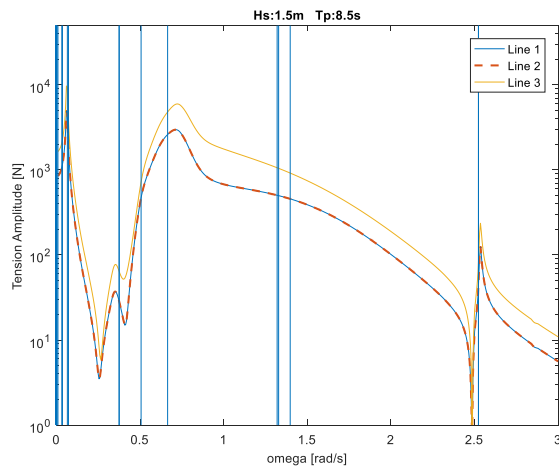
The required computational time of the *DynTD* model, as stated in Chapter 5 for a three line mooring system with lines made up of 15 line sections, is about 1.5 times real time for a model with 200 frequencies. It would require about 18 hours to run each 12-hour *TD* simulations introduced in this chapter. When running the equivalent case with the *DynFD* model in the same computer, it required about 80 seconds to obtain the linearized motion response, thus reducing in 1 to 2 orders of magnitude the computational cost. Nevertheless, in order to obtain smooth *PSDs* in the results introduced in this chapter, 600 frequencies have been used.

### 6.3.1 *Modal Analysis*

Even though the natural frequencies related with surge and sway change with the mean position of the structure, a relevant sea state has been selected to analyse the modes of motion of the coupled model,  $H_s=1.5\text{m}$  and  $T_p=8.5\text{s}$ , which corresponds with the most occurrent sea state at the selected site.



a)



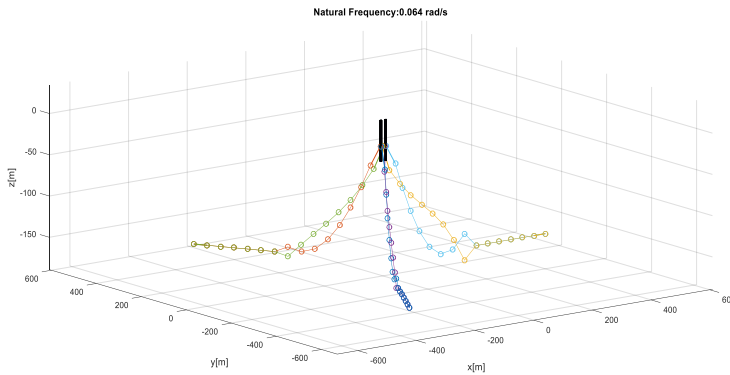
b)

Figure 71 Structure and internal surface water level motion a) and lines tension amplitudes at the fairleads b) and eigenvalues within the showed frequency range (vertical lines). Response amplitudes  $H_s=1.5\text{m}$  and  $T_p=8.5\text{s}$

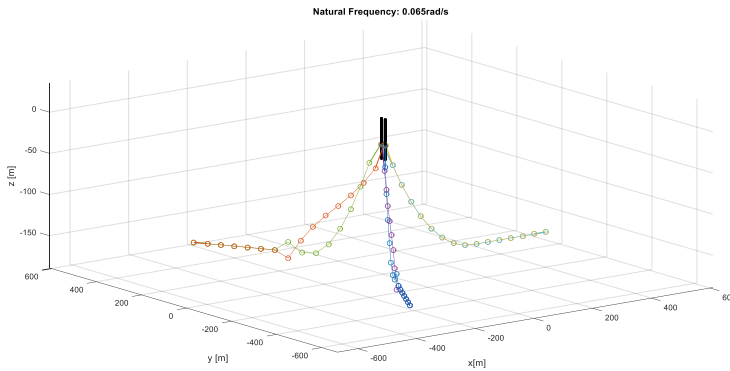
Figure 71 has been here introduced in order to visualize the relation between the *DOFs* of the *WEC* and the induced line tension amplitudes, subject to a representative sea state. Since the wave propagation direction does not excite sway, roll and yaw motions, these have been *Numerical Verification of the Dynamic Linearized Frequency Domain Model*

omitted in the figure. The most relevant eigenvalues have been considered to be those most influencing motions and tension amplitudes, all showed in Figure 71, with the vertical axis in logarithmic scale in order to visualize the correlation between motions, line tensions and eigenvalues.

It can be appreciated that the first peak in all motion and tension responses has two related eigenvalues. More precisely, the two modes of motion around this frequency, 0.065[rad/s] as represented in Figure 72.



a)

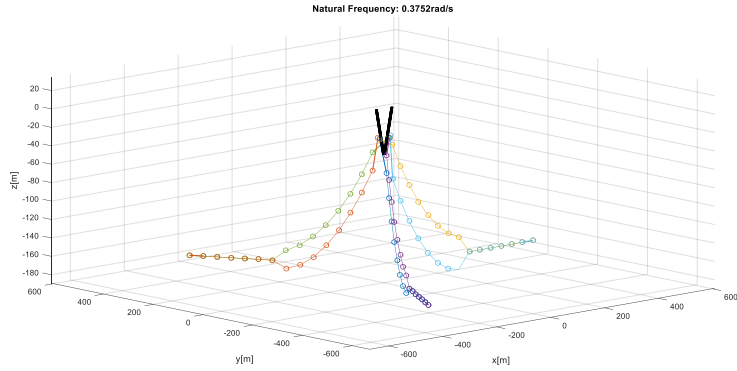


b)

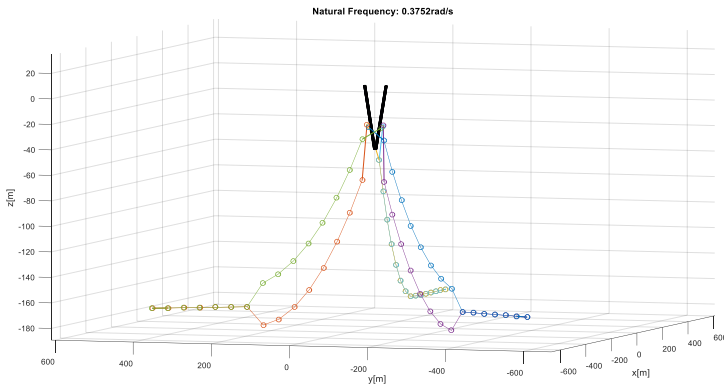
Figure 72 Modes of the coupled model mainly related with surge a) and sway b)

The modes represented in Figure 72 are mainly related with surge and sway motions of the *WEC*. The wave propagation direction aligned in the positive *X* axis mostly excites the mode related with the surge motion. Therefore, it produces the tension peak shown in Figure 71 in the corresponding frequency. Both surge and sway related natural frequencies have been found very close to each other, which indicates that the stiffness in surge is not very sensitive to the mean surge (equal to 0.8372m in the simulation shown in Figure 71) within the ranges of the introduced case study. Nevertheless, whilst the mode related with surge excites the three lines, the one related with sway excites only the two front lines. This statement should also be verified with small bending stiffness in the mooring lines. These modes of motion induce significant motions of lines' nodes which may produce significant viscous drag damping in surge in the linearized *FD* model.

A group of other 4 frequencies are found around 0.5[rad/s] in Figure 71, related with pitch and roll motions of the structure as well as heave of the structure and heave of the internal *SWL*, as represented in Figure 73 and Figure 74 respectively. It should be noted that the heave of the internal *SWL* corresponds with the piston mode in absolute coordinates, and the power is generated from the relative heave motion between the structure and the internal *SWL*.



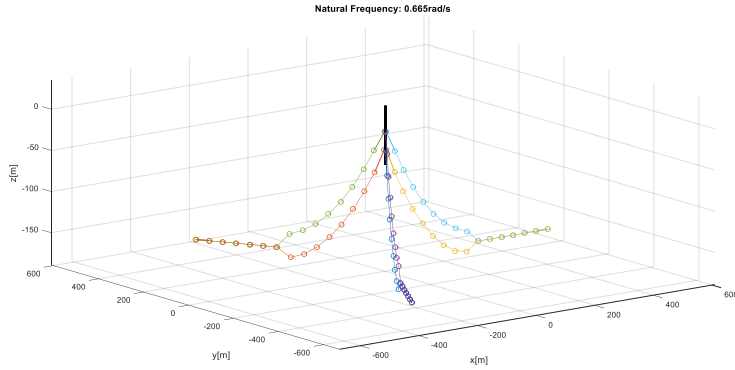
a)



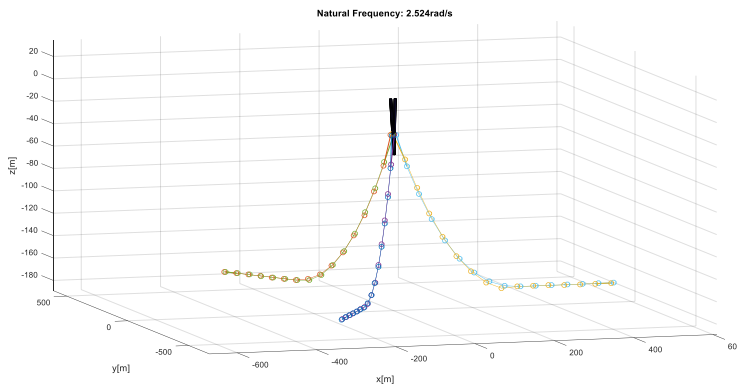
b)

Figure 73 Modes of the coupled model mainly associated with pitch a) and roll b)

Modes related with pitch and roll motions, as stated for surge and sway, induce significant line motions. In fact, these modes have been found significantly overdamped in the *FD* computed motion responses, shown in Figure 71, due to the linearization of drag forces both on the structure and on lines.



**a)**



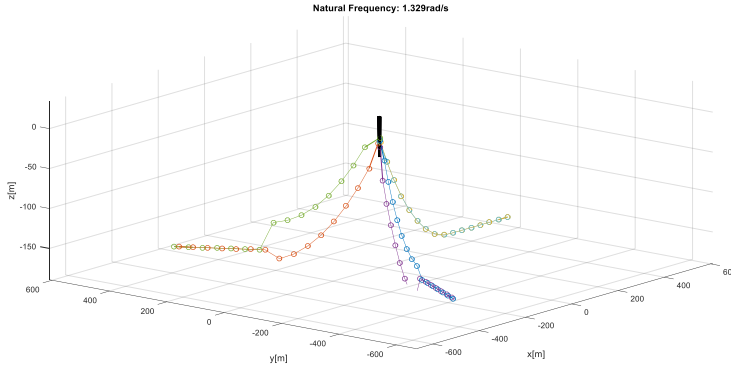
**b)**

Figure 74 Modes of the coupled model mainly associated with heave of the structure a) and pitch of the surface water level b)

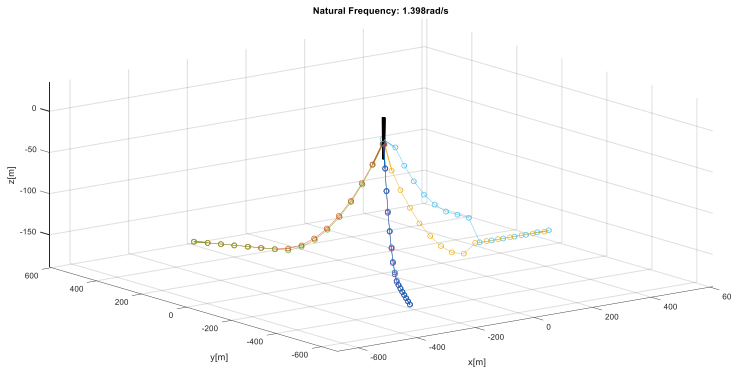
The modes related with structure and *SWL* heaving motions are represented in Figure 74 a) which, unlike surge and sway, do not excite significantly lines motions. On the other hand, the structure is significantly excited by waves and, consequently, large tension amplitudes can be observed in line tensions in Figure 71 b). The modes related with the internal *SWL* pitching, influence line tensions as they are coupled with the structure pitch and surge. It is clearly shown in Figure 71 that all modes experience a small excitation at the natural frequency in pitch of the internal *SWL*. However, this frequency should



be related with the corresponding sloshing mode in a more realistic numerical model. It has been found at a relatively large frequency and its influence on line tensions can be assumed not to be relevant.



a)



b)

Figure 75 Modes of the coupled model associated with line motions in the plane of the catenary of the windward lines a) and the leeward line b)

The modes represented in Figure 75 are related with in-plane lines motions with no significant motion of the structure. Both modes have been found to be in similar frequencies as the mean position of the structure has been relatively small, of 0.8372m, and the shape of the three lines is similar at that position. A third mode has been found at

1.32[rad/s], whose geometry has been omitted here, which shows a combination of both modes showed in Figure 75, but in opposing phase. These three modes are related with some differences between *DynFD* and *DynTD* models here compared, as explained in subsection 6.3.3. The modes of motion showed in Figure 75 stretch axially the three mooring lines. These modes, even though are well caught and provide invaluable information to the mooring designer, are a source of some disagreements between the *DynTD* and the *DynFD* approaches, as introduced in subsection 6.3.3.

### 6.3.2 Floater Motions

Surge, heave and pitch motions of both the floater and the internal *SWL* have been compared between both models in terms of their *PSDs* and the percentage difference of their standard deviations.

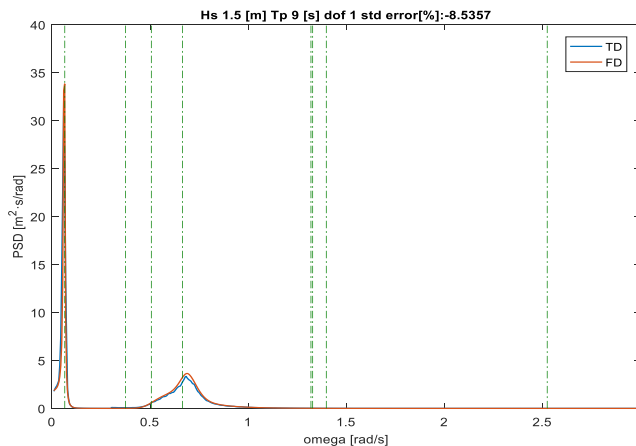


Figure 76 Surge motion *PSDs* of the floater. Wave frequency magnified with a factor of 100 to enable plotting the whole *PSD* in a single figure. Dash-dotted vertical lines indicate the relevant modes identified in section 6.3.1

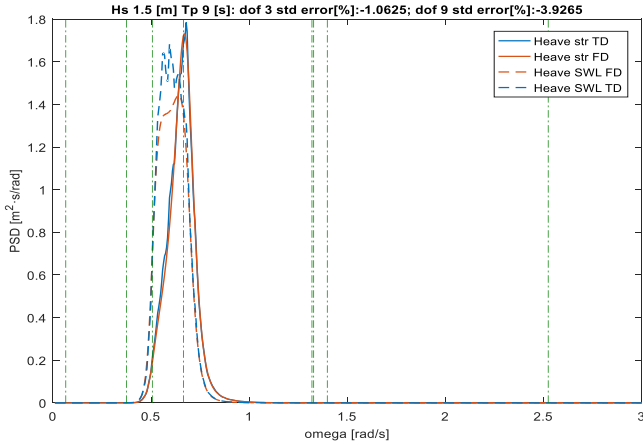


Figure 77 Heave motion *PSDs* of the floater (solid lines) and the internal *SWL* (dashed lines). Dash-dotted vertical lines indicate the relevant modes identified in section 6.3.1

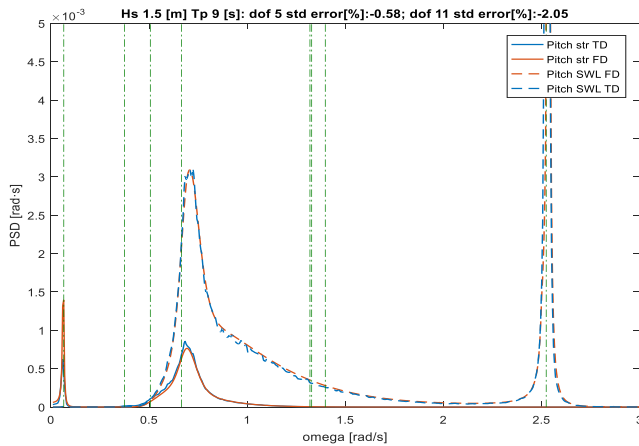


Figure 78 Pitch motion *PSDs* of the floater (solid lines) and the internal *SWL* (dashed lines). Dash-dotted vertical lines indicate the relevant modes identified in section 6.3.1

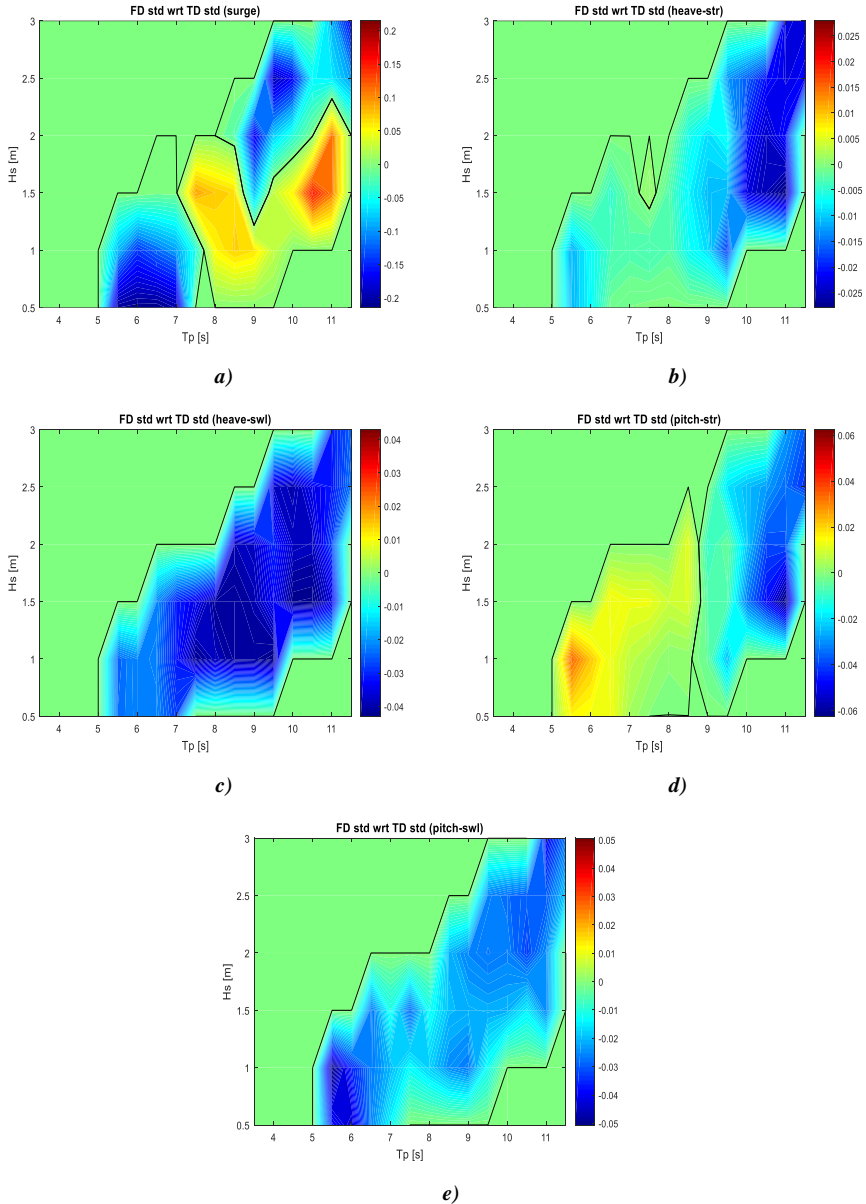
Looking at the natural frequencies related with each degree of freedom of the structure and the internal *SWL* in Table 1, motion response

amplitudes in Figure 76 to Figure 78 can be related to each natural frequency. The peaks of the response in surge and pitch at frequencies of  $0.065[\text{rad/s}]$  correspond with the natural frequency in surge, which indicates that both modes are coupled. As the peak period of the sea state showed in Figure 76 to Figure 78 is 9 seconds both heaving natural frequencies are significantly excited. This is shown in Figure 77 as the internal *SWL* is most amplified in frequencies close to  $0.5[\text{rad/s}]$  and the structure heaving at frequencies close to  $0.66[\text{rad/s}]$ . The pitching motion of the structure is not clearly shown in Figure 78 as there is no significant excitation around this frequency. In contrast, the pitching motion of the internal *SWL*, which corresponds to a sloshing mode, is clearly shown around its natural frequency of  $2.524[\text{rad/s}]$ , mostly due to not having introduced any viscous force in it.

The natural frequency in surge show good agreement between both models in Figure 76. It indicates that the linearized stiffness matrix introduced by the analytic mooring system represents well the mooring influence on the floating structure. The kinematic relations are well fulfilled as both models show negligible differences in surge, what can be observed in Figure 71, and consequently the surge of the water column has been omitted in Figure 76. However, the uncertainties in surge can be mostly attributed to the magnitude of motion in its natural frequency, consequence of differences on the mooring induced damping.

It is shown in Figure 78 that the pitching of the floater in the linearized model is overestimated in the *LF* range, balanced by the underestimation in the *WF* range. While the former is due to overestimates in surge, the latter can be attributed to the linearization of the viscous force term, that tends to overdamp the response. In addition, it is shown in Figure 79 that the pitch motion of the floater is underestimated when subject to more energetic sea states, amplifying the differences in pitch within the *WF* range.

Pitch of the internal *SWL* shows very good agreement as it is not directly influenced by the most relevant non-linearities, however, it corresponds with a sloshing mode of the surface and it may be largely influenced by the air chamber pressure, which has not been considered here.



e)

Figure 79 Percentage differences of the standard deviation of motions obtained with the *DynFD* with respect to the *DynTD*. Contour lines represent zero levels. a) Surge; b) Heave of the structure; c) Heave of the internal SWL; d) Pitch of the structure; e) Pitch of the internal SWL

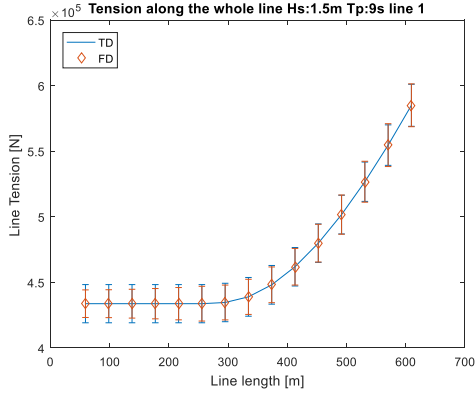
All degrees of freedom show in Figure 79 differences lower than 6% in standard deviation with respect to the non-linear *TD* model except surge. Surge, unlike other degrees of freedom, is very influenced by non-linear effects such as slowly varying wave drift forces and the geometric stiffness, what explains its larger differences. Additionally, the modes of motion related to surge and sway imply significant lines motions, as showed through modal analysis in Figure 72, and the inherent error made in the linearization of viscous forces on lines may vary the induced damping on structure motions. Mentioned effects make surge to be overestimated in most sea states, as a consequence of overestimations in the *LF* range and its high relevance on the standard deviation with respect to *WF* motions.

Heave motions although slightly underestimated in intermediate wave heights are in general in very good agreement, both of the structure and the *SWL*. Observed differences can be mostly attributed to being overdamped by the linearized viscous drag.

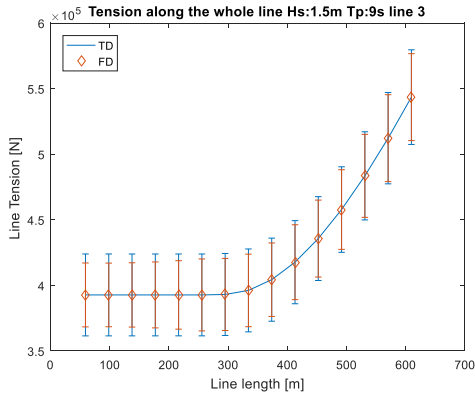
### 6.3.3 Line Tension

Line tension *PSDs* can be derived from nodes' motions both in the *LF* and in the *WF* range. The geometric stiffness linearization allows catching the induced line tensions in the *LF* range. As stated for pitch motions, line tensions are overestimated by the *FD* models in sea states with lower energy content. Similarly, the deviations in the *WF* range drives the total standard deviation percentage difference as the incoming wave energy increases, as represented in Figure 81 and Figure 82.

Heaving motions are significantly excited, and a non-linear behaviour of lines can be expected. Line tension amplitudes obtained in frequencies (0.5-0.7[rad/s]) corresponding to heave natural frequencies are acceptably well represented by the linearized model in Figure 82, specially for the windward lines, while the leeward *line 3* shows larger differences, more influenced by *WF* motions.



a)

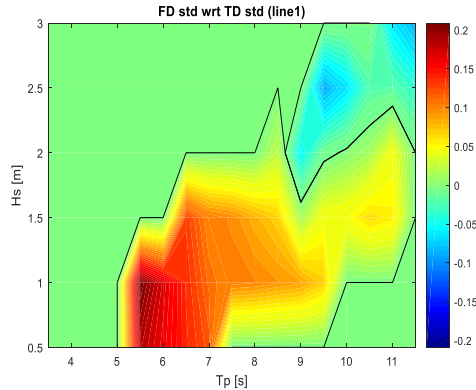


b)

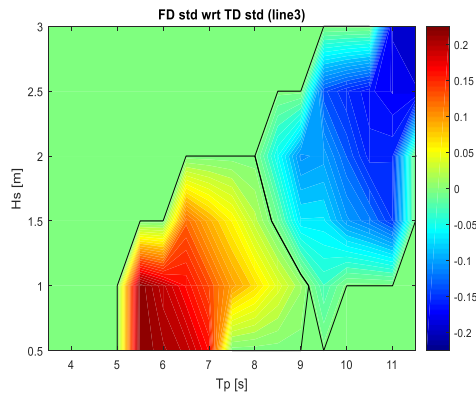
Figure 80 Line tension standard deviation (vertical lines at each node) with both models with respect to the mean line tension along the whole line 1 a) and line 3 b)

An estimation of line tensions *PSD* along the whole line is also provided by the *FD* model. Figure 80 shows the standard deviation (vertical lines) with respect to the mean tension computed with the analytic catenary equations, along the line. The mean tension difference between both models has been observed to be lower than 1%. In Figure 80 standard deviation differences have been found to be of 1.9% in the fairlead increased up to 27% in the anchor for lines 1 and 2 and of 8% in the fairlead up to 22% in the anchor for the line 3. The *FD* solution

tends to improve line tension estimates as the analysed section is closer to the fairlead, with the selected sea state.



a)



b)

Figure 81 Difference percentage of the linearized frequency domain model with respect to the non-linear time domain model in terms of line tensions standard deviation at the fairlead. Contour lines represent zero levels, showing both limits of the selected simulation sea states and limits between under and overestimations of the *DynFD* model.

There is however a remarkable difference between lines tensions obtained with both models in frequencies within 1.3-1.7[rad/s], mostly notable in low Hs. The frequency range is coincident with the modes described in Figure 75, as introduced in section 6.3.1 through modal



analysis. When the device is subject to low  $H_s$  sea states, line tension standard deviation values are overestimated with the *FD* model as shown in Figure 81, as a consequence of the *WF* range, observed in the *PSDs* in Figure 82 a). Although *PSDs* of lines' tension obtained with the *DynFD* model show a smooth decrease as the frequency is increased over these natural frequencies, the *DynTD* model show a steep decrease in the same range, especially in low energy sea states. This discrepancy can be attributed to non-linearities not appropriately caught in the linearized *FD* model, such as the interaction with the seabed or lifting line sections from the seabed. Moreover, it can cause overestimations in line tension standard deviation values of around 20% with low incoming energy, as shown in Figure 82. On the other hand, the explained discrepancy is balanced by the increasing line tension amplitudes induced by the heaving motions as the  $H_s$  is increased. Therefore, it is only relevant under low  $H_s$  sea states.



Good agreement has been obtained for all lines with the device subject to intermediate  $H_s$ , especially for the windward lines in the  $WF$  range, whilst slightly underestimated in  $LF$  for all lines, see Figure 82 c) and d). When analysed in moderate sea states, the windward lines results are improved with respect to lower  $H_s$  with some underestimation in the  $LF$  range. Nevertheless, Line 3, the leeward line, shows higher differences under moderate  $H_s$ , with lines tension standard deviation underestimated up to a 20%, due to the difference in the  $WF$  range, see Figure 82 f), which is mostly related with the heaving motion.

## 6.4 Chapter Summary

A verification work of the *DynFD* with the *DynTD* has been carried out considering a floating *WEC*, moored by means of a three catenary line mooring system. Differences in standard deviation of motions and line tensions at the fairleads have been shown and the strengths and weaknesses of the *DynFD* have been pointed out. The main findings can be summarized as:

- All maxima within the line tension *PSDs* are related with a mode of motion of the structure
- The mode of motion related with surge induces significant line motions. It produces a significant amount of viscous damping, identified as a source of uncertainty in surge motion estimates
- A group of three modes has been identified in frequencies over both heaving natural frequencies, that imply axially stretching of lines
- Most differences in surge motions are mainly related with the uncertainties introduced by the mooring induced damping
- Heave and pitch motions show in general good agreement, less influenced by the mooring linearization. The differences showed can be mostly attributed to the linearization of viscous forces on the floating structure
- Line tensions are very sensitive to the modes related with their axial stretching, especially with the system subject to mild sea states. As

the energy of the sea states is increased its influence is of relative importance compared with lines tension induced by the heave motions of the *WEC*

www.upv.es



Universidad  
del País Vasco

Euskal Herriko  
Unibertsitatea

## Chapter 7

# Conclusions

In this thesis a review of numerical modelling methods of catenary-moored floating structures has been carried out in Chapter 2, with an emphasis on *WEC* technologies, generally smaller and more dynamically excited than the traditional offshore structures. A comparative study about the most widely used numerical modelling approaches has been carried out in Chapter 4, under extreme environmental conditions. After showcasing that, in addition to the non-linear geometric stiffness, drag and inertia effects are of utmost importance, the corresponding lumped mass non-linear code has been developed, and the *DynTD* model has been introduced in Chapter 3. This model has been validated with tank test results of a *CALM* buoy subject to operational sea states in Chapter 5. Finally, since the mentioned *DynTD* model resolves the mooring system and floater motions numerical models in a fully coupled single mechanical system, it has been linearized, proposing the *DynFD* approach, also introduced in Chapter 3. Such a model has been developed in the frequency domain, coupling structure and line motions and accounting for lines drag and inertia as well as the linearized geometric stiffness on catenary mooring lines. The proposed *DynFD* developed model has been verified against the *DynTD* results in Chapter 6, using a floating *WEC* moored by means of three catenary mooring lines and obtaining good agreement in operational sea states.

The initial study, introduced in Chapter 4, considers the floating *WEC* introduced in section 3.6.1, subject to extreme waves and current. A set of 25 linear masses and lines pretension combinations has been considered and both structure motions and lines performance have been

analyzed, along with the corresponding cost of materials and the required footprint. It has been concluded that:

- The simplest approach, the *QSFD* introduced in section 3.2, provides acceptable results for the motions of the structure when moored with lines with mid to low pretensions
- High line pretensions show a significant amount of damping in structure's motions with the *DynTD* approach that cannot be caught with any other approach
- Line tensions obtained with the *QSFD* and *QSTD* approaches are far from the ones obtained with the *DynTD*, introduced in section 3.4, and have been considered not appropriate for detailed line tension estimates
- The *QSTD* approach, introduced in section 3.3, shows clearly the influence of all degrees of freedom, heaving included, on lines tension. However, the lack of lines inertia makes it to underestimate significantly lines tensions in the wave frequency range, performing well only in the low frequency range. This might be acceptable for structures other than floating *WECs*, that are primarily excited in the wave frequency range
- It has been observed that the difference between the *QSFD* and the *DynTD*, is mainly dependent on the pretension. Correction factors have been proposed for lines' length and tension. Acceptable cost estimates can be obtained using those factors with the *QSFD* approach, again for mid to low lines pretension and preliminary designs. This method is very simple to implement and fast enough to perform large amounts of simulations in a few hours

The main body of numerical modelling of this thesis has been focused in developing a simulation tool to solve a lumped mass model of the mooring system fully coupled with the floater dynamics, introduced in Chapter 3. The herein developed numerical models are based on the lumped mass concept, the *Cummins equation* in six degrees of freedom for each diffracting body and *Lagrange* multipliers approach for coupling the lumped mass model and all degrees of freedom described through the *Cummins equation*. In addition, as *WECs* are generally

composed of several rigid bodies, the kinematic relations have also been used to set restrictions between rigid diffracting bodies to compose floating *WECs*. This model has been validated with tank test results, as introduced in Chapter 5, using the results of the tank testing campaign of the *CALM* buoy described in section 3.6.2. It has been concluded that:

- Line tension estimates with transverse motions show lower accuracy, probably due to the seabed friction model
- Simulations in irregular waves with imposed motions have shown very good agreement. However, it has been observed that line tension estimates with numerical model is less sensitive to transverse motions compared with the physical tests
- Simulations in irregular waves with the *DynTD* coupled model show larger differences, mostly due to non-linearities in pitch that have not been modelled

One of the most significant contributions in this thesis is the *DynFD* model, introduced in section 3.5. It consists in linearizing all non-linear terms of the *DynTD* model. This enables the model to be solved in the frequency domain, resulting in an approach 1 to 2 orders of magnitude faster with respect to the non-linear time domain lumped mass. It has been verified with the corresponding *DynTD* simulations of the floating *WEC* moored with a catenary mooring with a high pretension and subject to operational sea states (up to  $H_s=3\text{m}$ ). The results of the verification have shown:

- Very good agreement in all degrees of freedom of the floater and lines' tension of the fairleads in most sea states has been obtained. The most notable disagreement has been found in mild and moderate  $H_s$  sea states in surge and lines' tension, of up to 20% in standard deviation. Mostly attributed to uncertainty in the mooring induced damping
- Modal analysis has shown that in mild  $H_s$  sea states some uncertainty is introduced by a mode stretching the whole lines, whose tension is slightly overestimated by the *DynFD* model



- In moderate  $H_s$  sea states some differences have been found in the leeward line in the wave frequency range, mostly related with heaving motions
- This verification has proven that lines' tensions can be obtained with a quick frequency domain model with good accuracy. The main drawback of this approach is that it may be complex to implement.

To sum up, preliminary cost estimates, based on extreme environmental conditions, can be obtained with the *QSFD* approach for mid to low pretensions, provided total suspended lines length and lines tension are corrected with correction factors varying with the lines' pretension. The non-linear lumped mass modelling approach provides itself very good results when the motion of the fairlead is within the plane of the catenary, and a further study should be performed to demonstrate that improved seabed models increase the accuracy of tension estimates. Larger uncertainties are introduced in floater body motions that are translated into line tension uncertainties. The herein proposed frequency domain approach (*DynFD*) of the fully coupled lumped mass and floater motion models has demonstrated good accuracy in operational conditions, it can efficiently be used to assess fatigue damage and control strategies accounting for the mooring influence.

## Recommendations for Future Work

Future research lines can be aligned with two main objectives, further verification and validation of the *DynFD* approach as well as its applicability to engineering practices.

An extended verification of the *DynFD* approach can be carried out, that may provide its applicability ranges in terms of environmental conditions, types of floating structure or mooring settings, i.e. line pretension and linear mass. This will increase the feasibility of the introduced approach within its applicable ranges.

Initial conditions of the *DynTD* and the mean position for the linearized *DynFD* are based on analytic catenary mooring systems. Extending the tools to find the corresponding positions for complex configurations of mooring systems would provide it with a large variety of potential applications within the sector.

Its applicability to fatigue life estimates can be very beneficial in terms of computational time. It implies assuming specific load cycle amplitude probability density functions built up from the obtained line tension spectral densities. A large body of research has been carried out by different authors to estimate probability density functions for non-gaussian loads, that can be used in combination with the results obtained with the *DynFD* model. Its applicability to fatigue damage estimates might, not only enable accounting for the fatigue damage earlier in the design process, but also to be integrated within different kinds of digital twins of floating platforms and its mooring systems.

Complex control algorithms of floating renewable energy structures can also be implemented with the additional purpose of minimizing loads on mooring lines. Such control subroutines may require linear systems of the floating structure and mooring lines to be solved systematically. This can be enabled with the herein proposed *DynFD* approach, that can be integrated in these control subroutines, as it provides structure motions and line tension power spectral densities in some tens of seconds.

www.upv.es



Universidad  
del País Vasco

Euskal Herriko  
Unibertsitatea

## References

- [1] H.J.J. Van den Boom, “Dynamic Behaviour of Mooring Lines,” *Behav. Offshore Struct. Elsevier Sci. Publ. B V*, pp. 359–368, 1985.
- [2] J. Azcona, X. Munduate, L. González, and T. A. Nygaard, “Experimental validation of a dynamic mooring lines code with tension and motion measurements of a submerged chain,” *Ocean Eng.*, vol. 129, pp. 415–427, Jan. 2017, doi: 10.1016/j.oceaneng.2016.10.051.
- [3] J. Azcona, D. Palacio, X. Munduate, L. González, and T. A. Nygaard, “Impact of mooring lines dynamics on the fatigue and ultimate loads of three offshore floating wind turbines computed with IEC 61400-3 guideline: Impact of mooring lines dynamics on the fatigue and ultimate loads of three offshore floating wind turbines computed with IEC 61400-3 guideline,” *Wind Energy*, vol. 20, no. 5, pp. 797–813, May 2017, doi: 10.1002/we.2064.
- [4] M. Hall and A. Goupee, “Validation of a lumped-mass mooring line model with DeepCwind semisubmersible model test data,” *Ocean Eng.*, vol. 104, pp. 590–603, Aug. 2015, doi: 10.1016/j.oceaneng.2015.05.035.
- [5] V. Harnois *et al.*, “Numerical model validation for mooring systems: Method and application for wave energy converters,” *Renew. Energy*, vol. 75, pp. 869–887, Mar. 2015, doi: 10.1016/j.renene.2014.10.063.
- [6] K. Xu, Z. Gao, and T. Moan, “Effect of hydrodynamic load modelling on the response of floating wind turbines and its mooring system in small water depths,” *J. Phys.*, p. 15.
- [7] T. H. J. Bunnik, G. de Boer, J. L. Cozijn, J. van der Cammen, E. van Haften, and E. ter Brake, “Coupled Mooring Analysis and Large Scale Model Tests on a Deepwater Calm Buoy in Mild Wave Conditions,” Feb. 2009, pp. 65–76, doi: 10.1115/OMAE2002-28056.

- [8] M. The Vu, H.-S. Choi, J. Kang, D.-H. Ji, and S.-K. Jeong, “A study on hovering motion of the underwater vehicle with umbilical cable,” *Ocean Eng.*, vol. 135, pp. 137–157, May 2017, doi: 10.1016/j.oceaneng.2017.02.035.
- [9] M. T. Vu *et al.*, “Study on Dynamic Behavior of Unmanned Surface Vehicle-Linked Unmanned Underwater Vehicle System for Underwater Exploration,” *Sensors*, vol. 20, no. 5, p. 1329, Feb. 2020, doi: 10.3390/s20051329.
- [10] C. V. Amaechi, F. Wang, X. Hou, and J. Ye, “Strength of submarine hoses in Chinese-lantern configuration from hydrodynamic loads on CALM buoy,” *Ocean Eng.*, vol. 171, pp. 429–442, Jan. 2019, doi: 10.1016/j.oceaneng.2018.11.010.
- [11] “Strength assessment of offshore structures - Sesam,” *DNV GL*. <https://www.dnvgl.com/services/strength-assessment-of-offshore-structures-sesam-software-1068> (accessed Dec. 15, 2019).
- [12] D. Gl, “SIMA Coupled Motion Analysis, Wind Turbines,” p. 26, 2018.
- [13] “OrcaFlex - dynamic analysis software for offshore marine systems,” *Orcina*. <https://www.orcina.com/orcaflex/> (accessed Dec. 15, 2019).
- [14] Z. Ran, M. H. Kim, and W. Zheng, “Coupled Dynamic Analysis of a Moored Spar in Random Waves and Currents (Time-Domain Versus Frequency-Domain Analysis),” *J. Offshore Mech. Arct. Eng.*, vol. 121, no. 3, pp. 194–200, Aug. 1999, doi: 10.1115/1.2829565.
- [15] A. F. de O. Falcão, “Wave energy utilization: A review of the technologies,” *Renew. Sustain. Energy Rev.*, vol. 14, no. 3, pp. 899–918, Apr. 2010, doi: 10.1016/j.rser.2009.11.003.
- [16] R. P. F. Gomes, J. C. C. Henriques, L. M. C. Gato, and A. F. O. Falcão, “Hydrodynamic optimization of an axisymmetric floating oscillating water column for wave energy conversion,” *Renew. Energy*, vol. 44, pp. 328–339, Aug. 2012, doi: 10.1016/j.renene.2012.01.105.

- [17] F. X. Correia da Fonseca, R. P. F. Gomes, J. C. C. Henriques, L. M. C. Gato, and A. F. O. Falcão, “Model testing of an oscillating water column spar-buoy wave energy converter isolated and in array: Motions and mooring forces,” *Energy*, vol. 112, pp. 1207–1218, Oct. 2016, doi: 10.1016/j.energy.2016.07.007.
- [18] “DNVGL-OS-E301.pdf.” Accessed: Oct. 26, 2019. [Online]. Available: <https://rules.dnvgl.com/docs/pdf/dnvgl/OS/2015-07/DNVGL-OS-E301.pdf>.
- [19] F. Cerveira, N. Fonseca, and R. Pascoal, “Mooring system influence on the efficiency of wave energy converters,” *Int. J. Mar. Energy*, vol. 3–4, pp. 65–81, Dec. 2013, doi: 10.1016/j.ijome.2013.11.006.
- [20] J. Fitzgerald and L. Bergdahl, “Including moorings in the assessment of a generic offshore wave energy converter: A frequency domain approach,” *Mar. Struct.*, vol. 21, no. 1, pp. 23–46, Jan. 2008, doi: 10.1016/j.marstruc.2007.09.004.
- [21] K. Larsen and P. C. Sandvik, “Efficient Methods For The Calculation Of Dynamic Mooring Line Tension,” presented at the The First ISOPE European Offshore Mechanics Symposium, Aug. 1990.
- [22] Y. M. Low and R. S. Langley, “Time and frequency domain coupled analysis of deepwater floating production systems,” *Appl. Ocean Res.*, vol. 28, no. 6, pp. 371–385, Dec. 2006, doi: 10.1016/j.apor.2007.05.002.
- [23] Y. M. Low and R. S. Langley, “A hybrid time/frequency domain approach for efficient coupled analysis of vessel/mooring/riser dynamics,” *Ocean Eng.*, vol. 35, no. 5–6, pp. 433–446, Apr. 2008, doi: 10.1016/j.oceaneng.2008.01.001.
- [24] J. Cruz, Ed., *Ocean wave energy: current status and future prepectives [i.e. perspectives]*. Berlin: Springer, 2008.
- [25] “Aquaret website. Technology types and description.” [http://www.aquaret.com/indexea3d.html?option=com\\_content&view=article&id=203&Itemid=344&lang=en#Animations](http://www.aquaret.com/indexea3d.html?option=com_content&view=article&id=203&Itemid=344&lang=en#Animations) (accessed Jun. 06, 2020).

- [26] “Pelamis Wave Power : EMEC: European Marine Energy Centre.” <http://www.emec.org.uk/about-us/wave-clients/pelamis-wave-power/> (accessed Jun. 06, 2020).
- [27] “Aquamarine Power : EMEC: European Marine Energy Centre.” <http://www.emec.org.uk/about-us/wave-clients/aquamarine-power/> (accessed Jun. 06, 2020).
- [28] “Fugro Installs Three Foundations for Oyster Wave Energy Device (UK),” *Offshore Wind*, Dec. 01, 2011. <https://www.offshorewind.biz/2011/12/01/fugro-installs-three-foundations-for-oyster-wave-energy-device-uk/> (accessed Jun. 06, 2020).
- [29] “MARMOK-A-5 Wave Energy Converter | Tethys.” <https://tethys.pnnl.gov/project-sites/marmok-5-wave-energy-converter> (accessed Apr. 06, 2020).
- [30] “IDOM - Grupo Internacional,” *IDOM*. <https://www.idom.com/es/> (accessed Apr. 06, 2020).
- [31] “Ireland leads the way in ocean energy as SEAI funded wave energy device arrives in Hawaii for testing,” *Sustainable Energy Authority Of Ireland*. <https://www.seai.ie/news-and-media/ocean-energy-test-device/> (accessed Jun. 06, 2020).
- [32] “<http://www.corpowerocean.com/technology/>.” <http://www.corpowerocean.com/technology/> (accessed Apr. 09, 2020).
- [33] “Oceantec | Marine energy.” <http://www.oceantecenergy.com/> (accessed Apr. 09, 2020).
- [34] “Components for Ocean Renewable Energy Systems | CORES Project | FP7 | CORDIS | European Commission.” <https://cordis.europa.eu/project/id/213633> (accessed Jun. 06, 2020).
- [35] “Ocean Energy Buoy Ribbon Cutting Ceremony,” *Energy.gov*. <https://www.energy.gov/eere/water/articles/ocean-energy-buoy-ribbon-cutting-ceremony> (accessed Dec. 05, 2020).

- [36] “Marine Energies - EVE.”  
<https://eve.eus/Actuaciones/Marina?lang=en-gb> (accessed Jun. 06, 2020).
- [37] “OES | News | International LCOE for Ocean Energy Technology.”  
<https://www.ocean-energy-systems.org/news/international-lcoe-for-ocean-energy-technology/> (accessed Mar. 16, 2020).
- [38] “Annual final price - Reference Retailers | OMIE.”  
<https://www.omie.es/en/market-results/annual/average-final-prices/reference-retailers?scope=annual&year=2019> (accessed Apr. 05, 2020).
- [39] B. de Miguel, P. Ricci, I. Touzón, and M. Ojanguren, “New perspectives on the long term feasibility of wave energy conversion: a techno-economical approach,” p. 7.
- [40] J. Weber, “WEC Technology Readiness and Performance Matrix – finding the best research technology development trajectory,” p. 10.
- [41] “DTCOceanPlus - Design tools for ocean energy systems,”  
*DTCOceanPlus - Design tools for ocean energy systems.*  
<https://www.dtoceanplus.eu/> (accessed Jun. 06, 2020).
- [42] I. E. A. Ocean Energy Systems, “International Levelised Cost of Energy for Ocean Energy Technologies,” May 2015.
- [43] “Moorings and Foundations Catalogue Deliverable 5.1,” Dec. 2016.
- [44] “Mooring systems - Bluewater.”  
<https://www.bluewater.com/products-technology/mooring-systems/> (accessed Nov. 10, 2020).
- [45] American Petroleum Institute (API), “API Recommended Practice 2SK - Design and Analysis of Stationkeeping Systems for Floating Structures.” Oct. 2005.
- [46] Ø. A. A. HARALD E. KROGSTAD, “Linear Wave Theory.”  
[http://folk.ntnu.no/oivarn/hercules\\_ntnu/LWTcourse/](http://folk.ntnu.no/oivarn/hercules_ntnu/LWTcourse/) (accessed Apr. 12, 2020).



- [47] J. Falnes, *Ocean waves and oscillating systems: Linear interactions including wave-energy extraction*. Cambridge University press, 2004.
- [48] J. M. J. W.W. Massie, *OffshoreHydromechanics.pdf*, First Edition. Delft: Delft University of Technology, 2001.
- [49] A. Naess and T. Moan, *Stochastic Dynamics of Marine Structures*. Cambridge: Cambridge University Press, 2012.
- [50] “BiMEP.” <https://bimep.com/pages/info> (accessed Dec. 19, 2019).
- [51] “DNV-RP-C205: Environmental Conditions and Environmental Loads,” p. 124, 2010.
- [52] “IEC TS 62600-100:2012 | IEC Webstore | electricity, water management, smart city, rural electrification, marine power.” <https://webstore.iec.ch/publication/7241> (accessed Sep. 27, 2020).
- [53] “IEC TS 62600-10:2015 | IEC Webstore | electricity, water management, smart city, rural electrification, marine power.” <https://webstore.iec.ch/publication/22012> (accessed Sep. 27, 2020).
- [54] “API.” <https://www.api.org:443/> (accessed Sep. 27, 2020).
- [55] “Rules & Guidelines,” *Marine & Offshore*. <https://marine-offshore.bureauveritas.com/rules-guidelines> (accessed Sep. 27, 2020).
- [56] O.M. Faltinsen, *Sea loads on ships and offshore structures*. Cambridge University press, 1990.
- [57] J N Newman, *Marine Hydrodynamics*. U.S.A.: The MIT Press, 2017.
- [58] W. E. Cummins, “The Impulse Response Function and Ship Motions,” presented at the Symposium on Ship Theory, Institut für Schiffbau der Universität Hamburg, Jan. 1962, Accessed: Jan. 02, 2020. [Online]. Available: <http://dome.mit.edu/handle/1721.3/49049>.

- [59] T. Francis Ogilvie, “Recent Progress Toward the Understanding and Prediction of Ship Motions,” Bergen, Norway, Sep. 1964, pp. 3–80.
- [60] S. Jamet, “NEMOH-Presentation,” *LHEEA*. <https://lhea.ec-nantes.fr/logiciels-et-brevets/nemoh-presentation-192863.kjsp?RH=1489593406974> (accessed Oct. 27, 2019).
- [61] “Wamit, Inc. - The State of the Art in Wave Interaction Analysis.” <https://www.wamit.com/> (accessed Dec. 19, 2019).
- [62] “ANSYS Aqwa | Hydrodynamics Simulation & Diffraction Analysis.” <https://www.ansys.com/products/structures/ansys-aqwa> (accessed Oct. 27, 2019).
- [63] G. Duclos, A. H. Clement, and G. Chatry, “Absorption of Outgoing Waves in a Numerical Wave Tank Using a Self-Adaptive Boundary Condition,” *Int. J. OFFSHORE POLAR Eng.*, vol. 11, pp. 168–175, 2001.
- [64] T. Perez and T. I. Fossen, “Time-domain vs. Frequency-domain Identification of Parametric Radiation Force Models for Marine Structures at Zero Speed,” *Identification Control*, p. 19.
- [65] “DNVGL-OS-E301: Position mooring,” Jul. 2018. Accessed: Mar. 16, 2020. [Online]. Available: <http://rules.dnvgl.com/docs/pdf/dnvgl/os/2018-07/dnvgl-os-e301.pdf>.
- [66] “NI 461 DTO R00 E - Quasi-Dynamic Analysis of Mooring Systems using Ariane Software,” Bureau Veritas, Oct. 1997.
- [67] Y. Yang, J. Chen, and S. Huang, “Mooring line damping due to low-frequency superimposed with wave-frequency random line top end motion,” *Ocean Eng.*, vol. 112, pp. 243–252, Jan. 2016, doi: 10.1016/j.oceaneng.2015.12.026.
- [68] International Ship & Offshore Structures Congress, M. L. Kaminski, P. Rigo, and IOS Press, Eds., *Proceedings of the 20th International Ship and Offshore Structures Congress (ISSC 2018)*. 2018.

- [69] J. Palm, C. Eskilsson, G. M. Paredes, and L. Bergdahl, “Coupled mooring analysis for floating wave energy converters using CFD: Formulation and validation,” *Int. J. Mar. Energy*, vol. 16, pp. 83–99, Dec. 2016, doi: 10.1016/j.ijome.2016.05.003.
- [70] O. A. Maestre, A. H. Frías, E. A. S. Martín, and V. P. Arcocha, “Parámetros redundantes para Rotación y Traslación en Cinemática,” p. 8.
- [71] “Sea loads ships and offshore structures | Engineering design, kinematics, and robotics | Cambridge University Press.” <https://www.cambridge.org/es/academic/subjects/engineering/engineering-design-kinematics-and-robotics/sea-loads-ships-and-offshore-structures?format=PB&isbn=9780521458702> (accessed Dec. 19, 2019).
- [72] J. Garcia De Jalon, *Kinematic and dynamic simulation of multibody systems: the realtime challenge*. U.S.A.: Springer, 1994.
- [73] “Tecnalia, Offshore renewable energy.” <https://www.tecnalia.com/en/energy-and-environment/offer-to-companies/offshore-renewable-energy/offshore-renewable-energy.htm> (accessed Jun. 14, 2020).
- [74] J. A. Pinkster and N. S. M. Basin, “Low Frequency Second Order Wave Exciting Forces on Floating Structures,” p. 220.
- [75] L. Bergdahl, J. Palm, C. Eskilsson, and J. Lindahl, “Dynamically Scaled Model Experiment of a Mooring Cable,” *J. Mar. Sci. Eng.*, vol. 4, no. 1, p. 5, Jan. 2016, doi: 10.3390/jmse4010005.
- [76] A. F. O. Falcão and L. M. C. Gato, “Air Turbines,” in *Comprehensive Renewable Energy*, Elsevier, 2012, pp. 111–149.
- [77] A. F. O. Falcão, L. M. C. Gato, and E. P. A. S. Nunes, “A novel radial self-rectifying air turbine for use in wave energy converters,” *Renew. Energy*, vol. 50, pp. 289–298, Feb. 2013, doi: 10.1016/j.renene.2012.06.050.
- [78] A. F. O. Falcão and J. C. C. Henriques, “The Spring-Like Air Compressibility Effect in OWC Wave Energy Converters: Hydro-

- , Thermo- and Aerodynamic Analyses,” presented at the ASME 2018 37th International Conference on Ocean, Offshore and Arctic Engineering, Sep. 2018, doi: 10.1115/OMAE2018-77096.
- [79] “Metocean Analysis of BiMEP for Offshore Design TRlplus,” IH-Cantabria, bimep, Mar. 2017. Accessed: Mar. 19, 2020. [Online]. Available: [https://trlplus.com/wp-content/uploads/2017/03/Metocean\\_Analysis\\_of\\_BiMEP\\_for\\_Offshore\\_Design\\_TRlplus\\_March\\_2017.pdf](https://trlplus.com/wp-content/uploads/2017/03/Metocean_Analysis_of_BiMEP_for_Offshore_Design_TRlplus_March_2017.pdf).
- [80] “The history of Orcina - find out about our journey and where it all began!,” *Orcina*. <https://www.orcina.com/about/history/> (accessed Nov. 14, 2020).
- [81] “HarshLab website,” *HarshLab*. <https://harshlab.eu/> (accessed Dec. 19, 2019).
- [82] “MATLAB - El lenguaje del cálculo técnico - MATLAB & Simulink.” <https://es.mathworks.com/products/matlab.html> (accessed Jul. 05, 2020).
- [83] F. Wendt *et al.*, “Ocean Energy Systems Wave Energy Modelling Task: Modelling, Verification and Validation of Wave Energy Converters,” *J. Mar. Sci. Eng.*, vol. 7, no. 11, p. 379, Nov. 2019, doi: 10.3390/jmse7110379.
- [84] M. Penalba, A. Mérigaud, J.-C. Gilloteaux, and J. V. Ringwood, “Influence of nonlinear Froude–Krylov forces on the performance of two wave energy points absorbers,” *J. Ocean Eng. Mar. Energy*, vol. 3, no. 3, pp. 209–220, Aug. 2017, doi: 10.1007/s40722-017-0082-x.
- [85] “BiMEP.” <https://bimep.com/> (accessed Oct. 26, 2019).

www.ehu.es



Universidad  
del País Vasco

Euskal Herriko  
Unibertsitatea

# Main Outcomes of this Thesis

## Articles Indexed in Journal Citation Reports

*I. Touzon, V. Nava, B. de Miguel, and V. Petuya, “A Comparison of Numerical Approaches for the Design of Mooring Systems for Wave Energy Converters,” JMSE, vol. 8, no. 7, p. 523, Jul. 2020, <https://doi:10.3390/jmse8070523> . Impact Factor (2019):2.033. Q2: 31/66 Oceanography*

*I. Touzon, V. Nava, Z. Gao, I. Mendikoa, and V. Petuya, “Small scale experimental validation of a numerical model of the HarshLab2.0 floating platform coupled with a non-linear lumped mass catenary mooring system,” Ocean Engineering, vol. 200, p. 107036, Mar. 2020, doi: [10.1016/j.oceaneng.2020.107036](https://doi.org/10.1016/j.oceaneng.2020.107036). Impact Factor (2019):3.068. Q1: 1/14 Engineering, Marine*

*I. Touzon, V. Nava, Z. Gao, and V. Petuya, “Frequency domain modelling of a coupled system of floating structure and mooring Lines: An application to a wave energy converter,” Ocean Engineering, vol. 220, p. 108498, Jan. 2021, doi: [10.1016/j.oceaneng.2020.108498](https://doi.org/10.1016/j.oceaneng.2020.108498). Impact Factor (2019):3.068. Q1: 1/14 Engineering, Marine*

In addition to the mentioned publications, during the development of this PhD there have also been other publications related with the work here presented, that resulted from collaborations with other research centers, especially with Tecnalia Research & Innovation, Offshore Renewable Energy Area:

*Wendt et al., “Ocean Energy Systems Wave Energy Modelling Task: Modelling, Verification and Validation of Wave Energy Converters,” JMSE, vol. 7, no. 11, p. 379, Oct. 2019, doi:[10.3390/jmse7110379](https://doi.org/10.3390/jmse7110379).*

## Conference Publications

*I. Touzon, B. de Miguel, V. Nava, V. Petuya, I. Mendikoa, and F. Boscolo, “Mooring System Design Approach: A Case Study for MARMOK-A Floating OWC Wave Energy Converter,” in Volume 10: Ocean Renewable Energy, Madrid, Spain, Jun. 2018, p. V010T09A025, doi:[10.1115/OMAE2018-77634](https://doi.org/10.1115/OMAE2018-77634)*

In addition to the mentioned conference publications, during the development of this PhD there have also been other conference publications related with the work here presented, that resulted from collaborations with other research centers, especially with Tecnalia Research & Innovation, Offshore Renewable Energy Area:

*F.-X. Faÿ et al., “Numerical Simulation of Control Strategies at Mutriku Wave Power Plant,” presented at the ASME 2018 37th International Conference on Ocean, Offshore and Arctic Engineering, Sep. 2018, doi: [10.1115/OMAE2018-78011](https://doi.org/10.1115/OMAE2018-78011).*

*F. Wendt et al., “International Energy Agency Ocean Energy Systems Task 10 Wave Energy Converter Modeling Verification and Validation,” in European Wave and Tidal Energy Conference, Cork, Ireland, Aug. 2017*

*K. Nielsen et al., “OES Task 10 WEC heaving sphere performance modelling verification,” presented at the 3rd International Conference on Renewable Energies Offshore (RENEW 2018), Lisbon, Portugal, Oct. 2018.*

*I. Touzon, A. Garcia-Corcuera, V. Nava, R. Rodriguez, and B. de Miguel, “Mooring system monitoring of offshore renewable energy floating platforms,” in 3rd International Conference on Renewable Energies Offshore (RENEW 2018), Lisbon, Portugal, Oct. 2018, p. 6.*

## Participation in Seminars

*Mooring Design and Analysis of Floating Offshore Renewable Energy (ORE) Devices. 2<sup>nd</sup> Marine Energy Conference. Euskampus Fundazioa. 2015*

*Quasistatic Design Approach of Mooring Systems for Floating Offshore Renewable Energy Devices. 3<sup>rd</sup> Marine Energy Conference. Euskampus Fundazioa. 2016*

*Frequency and Time Domain Models of Mooring Line Dynamics for Coupled Analysis of Renewable Energy Devices. 4<sup>th</sup> Marine Energy Conference. Euskampus Fundazioa. 2017*

*Fatigue Load Ranges of Mooring Lines of Floating Offshore Renewable Energy Platforms. 5<sup>th</sup> Marine Energy Conference. Euskampus Fundazioa. 2018*

*Fatigue Analysis of Mooring Lines in Time and Frequency Domains for Wave Energy Converters. 6<sup>th</sup> Marine Energy Conference. Euskampus Fundazioa. 2019*



